Title: High-Pressure High-Temperature Laboratory Micro to Nano seismic Comparison of GEIOS Nitrogen Hybrid Gas Nanofoam and Conventional Water-Proppant EGS.

Shad AM Serroune 1-2*, Professor Jan Sopaheluwakan 2*, Dr Khasani IR 2*, Edwin Larry Zhang 3*, Harris Sackiewsky 2*
1GEIOS Technologies USA Corporation, Miami, Florida USA.
2Nanogeios Laboratory USA LLC, Wyoming, USA.
3Nanogeios Laboratory UK London, GB
*Correspondence: contact@nanogeios.io

Abstract:

Laboratory validation of a nitrogen hybrid gas nanofoam integrated with engineered conductive geocasing demonstrates maintained fracture support and enhanced conductive heat transfer under simulated geothermal reservoir conditions of 80–140 MPa and up to 300 °C. A nitrogen-dominant working fluid with embedded Al O (0.6–$_{2\ 3}$ 0.8 vol%) and silica (0.3–0.5 vol%) nanoparticles (~95% N by volume) was evaluated$_2$ in an Inconel 718 high-pressure, high-temperature vessel. Over a 15-week programme, an initial 3 mm fracture aperture showed 12% total degradation, while bulk thermal conductivity remained significantly elevated—a 166–336% improvement relative to typical rock and fluid baselines.

Wideband acoustic emission monitoring at core scale (8 sensors, 100–900 kHz, 5 MHz sampling) recorded a shift toward lower-energy, higher-frequency micro-failures, with total events reduced by 49% (52 vs. 102), average event energy reduced by 59% (2.34 vs. 5.73 aJ), and characteristic frequency increased by 83% (6.55 vs. 3.57 kHz) relative to water-fractured controls; the apparent b-value reached 1.52, consistent with distributed microcracking. Probabilistic uncertainty and risk analysis identified stress-gradient thresholds separating acceptable operation from potentially unacceptable regimes. Pressure decay to 50% of initial overpressure occurred in 3.2 min, and post-test material recovery exceeded 98% with a biodegradation index of 0.94.

Results support a conduction-dominated extraction. strategy combined with continuous microseismic monitoring and adaptive pressure control, while field-scale validation is required to confirm reservoir-scale seismic behaviour.

Keywords:

Nitrogen Hybrid Gas Nanofoam, GEIOS, EQG, EGS, SPARC, HPHT, induced seismicity, acoustic emission (AE), b-value, thermal conductivity, fracture aperture, Al2O3/SiO2 nanoparticles, proppant, stress gradient, probabilistic risk assessment, microseismic monitoring, permeability, granite, basalt, limestone, and field-scale validation.

1 Introduction

Enhanced geothermal systems (EGS) are often constrained by limited fracture stability and inadequate thermal transport, particularly under sustained high temperature and pressure conditions. Conventional water-based approaches typically achieve thermal conductivities below $1.0\ W\ m^{-1}\ K^{-1}$, which restricts heat transfer efficiency and reduces long term energy extraction (**23**). In addition, proppant-based technologies in subsurface applications can suffer from fines generation, proppant crushing, and severe loss of fracture conductivity under stress, with laboratory studies reporting fines production up to $51\ \%$ and associated porosity reductions of 75 to $98\ \%$, leading to conductivity losses approaching $99\ \%$ in high stress environments (**5**).

These degradation mechanisms not only limit system performance but also contribute to mechanical instability of fractures. To address these limitations, a nitrogen hybrid gas nanofoam system has been developed that integrates engineered nanoparticles within a nitrogen gas matrix for geothermal use. The nanofoam consists of approximately $95\ \%$ nitrogen by volume with embedded Al_2O_3 and silica nanoparticles and is designed to operate at pressures between 80 and $140\ MPa$ and temperatures up to $240\ ^\circ C$, conditions representative of demanding geothermal reservoirs (**23**).

In laboratory validation over 15 weeks, this system-maintained fracture apertures of $3\ mm$ with only $12\ \%$ degradation, while achieving thermal conductivities of about $30\ W\ m^{-1}\ K^{-1}$, corresponding to a 166 to $336\ \%$ enhancement relative to conventional materials used in comparable settings (**23**,**24**).

Independent analyses of nitrogen nanofoam technologies confirm that nitrogen based foams sustain stability significantly longer than conventional systems at temperatures up to $200\ ^\circ C$ and pressures of $6.9\ MPa$, especially when stabilized with additives such as graphene oxide that extend foam half life to 200 to 500 hours. Nitrogen as the carrier phase provides several flow and compatibility advantages. Its viscosity at standard conditions is orders of magnitude lower than that of water or oil based fluids, with reported values near $1.76 \times 10^{-5}\ Pa \cdot s$, which reduces flow resistance in complex fracture networks and diminishes energy requirements for injection and circulation.

In geothermal environments where pressures can exceed $80\ MPa$ and temperatures surpass $300\ ^\circ C$, nitrogen based systems support consistent and efficient fluid transport through the fracture matrix, with low interfacial tension further decreasing frictional interactions among gas, liquid, and rock phases and promoting uniform flow distribution, particularly in high permeability formations such as limestone or fractured granite.

Unlike proppant laden fluids that can suffer from settling, migration, and mechanical embedment, nitrogen based nanofoams avoid introducing solid residues that obstruct flow paths and increase maintenance demands (**5**). Within this broader technological context, GEIOS Enhanced Quantum Geothermal (EQG) technology combines the nitrogen hybrid gas nanofoam with advanced metamaterials in a specialized geocasing to improve both fracture stability and thermal transport.

Laboratory testing between March and November 2024 demonstrated that the GEIOS nanofoam system maintains stable fracture apertures of $3\ mm$ with only $12\ \%$ degradation over extended testing, under pressures of 80 to $140\ MPa$ and temperatures up to $240\ ^\circ C$, while sustaining thermal conductivity near $30\ W\ m^{-1}\ K^{-1}$ (**23**,**24**). These results were obtained under conditions characterized by Reynolds numbers exceeding 10^4 and Weber numbers above 50, with particle distribution uniformity quantified by coefficients of variation below $5\ \%$ and coalescence rates less than $0.5\ \%$ per hour (**23**).

Beyond thermal and mechanical performance, operational risk assessment and uncertainty analysis form a central component of the GEIOS development. Sensitivity analyses highlight that maintaining a stress gradient below $0.72\ psi\ ft^{-1}$ keeps operations within acceptable risk thresholds, while gradients above $0.77\ psi\ ft^{-1}$ may correspond to unacceptable risk even when other parameters are optimized (**24**). Injection pressure ranges from 80 to $140\ MPa$ and operational pressure bands of 1200 to $2000\ psi$ are evaluated using probabilistic frameworks, with quantiles at 1314.0, 1603.7, and $1901.2\ psi$ delineating expected operational conditions and informing mitigation strategies.

Data for these analyses are consolidated from laboratory validation tests, in situ measurements, well logs, seismic data, and empirical models, and are used to construct parameter probability density functions for fracture stability, porosity, nanoparticle dispersion, and related quantities (**23**,**24**). Seismic evaluation tools and real time seismic mapping are integrated to refine formation specific risk assessments, including formation dependent stability indices and seismic sensitivities for granite, basalt, and limestone (**23**).

Collectively, these findings establish the nitrogen hybrid gas nanofoam system as a promising candidate for improving geothermal fracture stability, thermal performance, and operational risk management, while also underscoring the need for continued seismic monitoring and field scale validation of induced seismicity behavior (**23**,**24**,**5**).

2 Background and Context

2.1 Overview of Enhanced Geothermal Systems (EGS)

2.1.1 Historical development of EGS

Early enhanced geothermal concepts centered on hydraulic fracturing of low permeability hot rocks using water based fluids and solid proppants, with performance typically constrained by limited fracture stability and modest thermal transport. Conventional approaches generally achieved thermal conductivities below $1.0\ W\ m^{-1}\ K^{-1}$, which restricted heat transfer efficiency and long term energy extraction.

Proppant based stimulation further introduced fines generation, proppant crushing, and severe loss of fracture conductivity under stress, with laboratory measurements reporting fines production up to $51\ \%$ and porosity reductions of 75 to $98\ \%$, leading to conductivity losses approaching $99\ \%$ in high stress environments. These degradation mechanisms led to unstable fracture networks and increasing maintenance demands in subsurface operations. Subsequent development efforts introduced gas based and foam based stimulation fluids to overcome some of these limitations.

Nitrogen was identified as a promising carrier phase due to its very low viscosity at standard conditions, approximately $1.76 \times 10^{-5}\ Pa \cdot s$, which is orders of magnitude lower than water or oil based fluids. In geothermal environments characterized by operational pressures exceeding $80\ MPa$ and temperatures surpassing $300\ ^{\circ}C$, nitrogen-based systems were shown to provide consistent and efficient fluid transport through fracture networks. The low interfacial tension of nitrogen reduced frictional interactions among gas, liquid, and rock phases and promoted more uniform flow distribution, particularly in high permeability formations such as limestone and fractured granite.

Unlike proppant laden systems, nitrogen injection did not introduce solid residues that could obstruct flow paths or exacerbate fracture instability, marking a significant conceptual shift in EGS stimulation strategies. Building on these advances, development of nitrogen hybrid gas nanofoam systems integrated nanoparticles into the nitrogen matrix to simultaneously address flow, thermal, and mechanical performance. In one implementation, aluminum oxide nanoparticles with thermal conductivities near $30\ W\ m^{-1}\ K^{-1}$ were incorporated to enhance heat transfer in high temperature reservoirs operating between 80 and $140\ MPa$ and at temperatures above $300\ ^{\circ}C$. This configuration enabled maintenance of fracture apertures of approximately $3\ mm$ or greater over multi year design horizons, thereby sustaining permeability and reducing reinjection frequency.

The inert nitrogen gas matrix improved compatibility with reactive formations, while nanoparticle mediated thermal pathways increased energy recovery relative to traditional water and proppant based fluids. These developments established nitrogen nanofoam as a candidate working fluid for both conventional EGS and hot dry rock systems in low permeability granite and basalt (**5**).

Parallel research on supracrystalline organization and phonon guided heat transport introduced the SPARC framework, which focuses on engineered structural alignment to control thermal conduction. In SPARC treated materials, anisotropic corridors exhibit thermal conductivities of approximately 30 to $30.5\ W\ m^{-1}\ K^{-1}$ along preferred axes, with polar measurements demonstrating an ellipsoidal distribution of thermal conductivity characteristic of transversely isotropic media.

Thermal diffusivity is measured under nitrogen atmosphere from 25 to $200\ ^{\circ}C$ by laser flash analysis, and bulk thermal conductivity is obtained from $\kappa = \alpha \rho C_p$, where density and specific heat capacity are independently characterized. Time domain thermoreflectance provides local conductivity mapping at micro to mesoscale, while Brillouin spectroscopy yields phonon velocities and mean free paths through kinetic theory relationships.

Within this supracrystalline paradigm, SPARC corridors serve as high conductivity pathways that can be integrated into engineered geothermal concepts and coupled with nitrogen nanofoam to enhance both heat extraction and, in some configurations, hydrogen co production (**15**,**16**).

More recent EGS concepts incorporate these structural and fluid innovations into integrated systems such as GEIOS nitrogen hybrid gas nanofoam technology. Validation programs employ custom high pressure and high temperature chambers to emulate commercial deployment conditions and quantify fracture stability, thermal conductivity, and operational risk under pressures from 80 to $140\ MPa$ and temperatures up to $240\ ^{\circ}C$.

Sensitivity analyses within these programs identify stress gradient thresholds, for example maintaining gradients below $0.72\ psi\ ft^{-1}$ to remain within acceptable risk domains, and emphasize the control of injection pressure, nanoparticle composition, and mud density. Complementary seismic evaluation tools and real time monitoring are used to refine stability indices and seismic sensitivities for formations such as granite, basalt, and limestone, linking contemporary nanofoam based EGS designs to a broader evolution in risk informed geothermal engineering (**23**,**24**).

2.1.2 Conventional water-and-proppant stimulation methods

Water based hydraulic stimulation with granular proppants has historically provided the reference framework against which alternative EGS working fluids are evaluated. Under high stress conditions relevant to geothermal reservoirs, ceramic and sand proppants undergo progressive mechanical degradation, generating large volumes of fines and severely impairing fracture transport properties.

Laboratory measurements show that ceramic proppants can produce about $6\ \%$ fines, whereas frac sand may generate up to $51\ \%$ fines when subjected to sustained loading. Associated reductions in proppant pack porosity reach 75 to $98\ \%$, and measured fracture conductivity losses can approach $99\ \%$ in high stress environments, indicating near complete loss of effective transmissivity in the stimulated fractures.

These results point to fines generation, grain crushing, and compaction as dominant failure modes in conventional water proppant systems, with direct implications for both hydraulic performance and long term fracture stability.

Beyond the intrinsic fragility of the proppant pack, fluid mechanical constraints further limit the effectiveness of water based stimulation.

Conventional water or oil based fracturing fluids exhibit substantially higher viscosities than nitrogen, which increases frictional pressure losses and promotes non uniform flow distribution in complex fracture networks. Under geothermal operating conditions with pressures commonly above $80\ MPa$ and temperatures beyond $300\ ^{\circ}C$, these viscous fluids sustain elevated pore pressures over longer durations, thereby maintaining strong hydraulic communication with the surrounding formation.

At the same time, solid proppant grains can settle, migrate, or become mechanically embedded within fracture asperities, producing localized flow blockages and additional loss of conductivity. Evidence indicates that such settling and embedment phenomena contribute to uneven flow paths and accelerated mechanical degradation of the proppant supported fractures. Operational longevity analyses highlight the practical consequences of these degradation mechanisms.

Simulation studies comparing nitrogen nanofoam with conventional proppant and fluid systems project fracture stability lifetimes of only 5 to 7 years for standard proppant based completions, in contrast to longer time horizons for nanofoam designs.

Over comparable intervals, water based fluids are associated with more frequent reinjection cycles, whereas proppant supported fractures tend to experience closure and loss of aperture as fines accumulate and grains crush. In performance summaries, conventional proppant systems typically display lower effective flow efficiencies and thermal conductivities than nitrogen nanofoam, with proppant packs and water based fluids reporting thermal conductivities in the range of 1 to $5\ W\,m^{-1}\,K^{-1}$ and about $0.6\ W\,m^{-1}\,K^{-1}$, respectively, values that constrain heat extraction relative to high conductivity alternatives.

These comparative simulations also associate conventional systems with higher environmental impact due to chemical residues and the need for more frequent interventions, although detailed field scale validation remains an open requirement. Mechanical stability within fractures stimulated by water and proppant is further challenged by the lack of dynamic pressure redistribution once pumping is reduced.

Because water is relatively incompressible, pressure dissipation can be spatially heterogeneous, particularly where proppant packs have compacted or where fines have accumulated. In such conditions, segments of the fracture network may remain overpressured while other zones close, reinforcing stress concentrations and exacerbating permeability loss.

Studies of nitrogen based alternatives explicitly contrast this behavior with gas dominated foams that distribute pressure more uniformly and do not leave residual solid skeletons, underscoring how traditional water proppant methods inherently couple hydraulic, mechanical, and transport degradation.

Taken together, these findings motivate development of stimulation strategies that avoid large granular proppant loads and sustained high viscosity water injection, in order to reduce long term fracture closure, fines production, and associated risks to operational reliability (**5**).

2.1.3 Known seismicity issues in EGS

Induced seismicity in enhanced geothermal operations is closely tied to how stimulation strategies modify formation stresses, fracture stability, and pressure fields. Conventional water based hydraulic stimulation with granular proppants has been shown to couple several degradation mechanisms that can influence seismic behavior indirectly through loss of mechanical integrity and heterogeneous stress redistribution.

(See Section 2.1.2 for detailed discussion of proppant fines generation.)

These processes reflect grain crushing, compaction, and embedment, which create localized zones of stiffness contrast and stress concentration that can interact with surrounding fracture networks and faults. Sustained high viscosity water injection further distinguishes traditional stimulation from gas based alternatives.

Viscous, largely incompressible water maintains elevated pore pressures over extended durations, especially where proppant packs have compacted or fines have accumulated. In such settings, segments of the fracture network can remain overpressured while other zones close, reinforcing spatially heterogeneous stress fields and potentially promoting unstable slip along critically stressed discontinuities.

Settling and migration of proppant grains, together with mechanical embedment into asperities, aggravate this heterogeneity by producing blocked or partially clogged segments, which in turn modify local pressure gradients and effective stresses. These coupled hydraulic and mechanical effects contribute to a higher induced seismicity risk profile, even though direct fault slip at reservoir scale is not reproduced in the reported laboratory studies.

Nitrogen based stimulation and, in particular, nitrogen hybrid gas nanofoam systems are designed within a different mechanical and hydraulic regime. Nitrogen gas exhibits an exceptionally low viscosity of approximately $1.76 \times 10^{-5}\ Pa \cdot s$ at standard conditions and does not introduce solid residues into the fracture network.

This low viscosity reduces frictional pressure losses and promotes more uniform flow distribution across complex fracture systems, diminishing the likelihood of localized overpressurization that could drive unstable fracture propagation.

Moreover, the absence of granular proppant avoids the fines generation, proppant crushing, and associated porosity collapse that characterize conventional systems, thereby mitigating one of the mechanical pathways by which stress concentrations and seismic susceptibility can evolve during long term operation (**5**).

Within the GEIOS nitrogen hybrid gas nanofoam framework, seismic evaluation is treated as an integral component of risk characterization rather than an afterthought. Seismic evaluation tools and real time seismic mapping are explicitly incorporated into testing and uncertainty analysis to refine formation specific risk assessments.

Formation dependent stability indices and seismic sensitivities have been reported for granite, basalt, and limestone, together with a seismic risk matrix and formation stability index that jointly describe likelihood and severity of seismic activity under nanofoam operation. For example, formation specific parameters combine permeability, operational pressure ranges, fracture

stability metrics, film strength, and seismic sensitivity factors, with reported seismic sensitivity values of 0.3, 0.4, and 0.6 for granite, basalt, and limestone, respectively.

These quantities are used to construct formation specific risk matrices and to interpret the impact of nanofoam supported fractures on induced seismicity potential.

Uncertainty assessment for the GEIOS system aggregates data from laboratory validation tests, in situ measurements, well logs, seismic data, and injection simulations into parameter probability density functions.

Within this framework, stress gradients, pore pressure ranges, and injection pressures are evaluated to ensure consistency with fracture stability and tectonic constraints. Sensitivity analyses show that maintaining a stress gradient below $0.72\ psi\,ft^{-1}$ keeps operations within acceptable risk thresholds, whereas gradients above $0.77\ psi\,ft^{-1}$ may correspond to unacceptable risk domains even when other parameters are optimized.

These findings emphasize that induced seismicity risk is strongly conditioned by the interplay between injection strategy, formation properties, and stress state, and they motivate active control of injection pressure and nanofoam composition within the specified uncertainty ranges (**23**,**24**). Despite these advances, all reported seismic characterizations remain grounded in laboratory and modeling studies conducted in high pressure, high temperature chambers and in probabilistic frameworks that integrate limited field data.

Such approaches cannot reproduce reservoir scale fault slip or capture the full complexity of natural fault networks. Consequently, the literature on GEIOS and nitrogen nanofoam systems identifies continuous field scale micro-seismic monitoring, together with refinement of formation specific stability indices, as essential next steps for validating the apparent reductions in induced seismicity risk inferred from controlled experiments and probabilistic analyses (**23**,**24**,**5**).

2.2 Emergence of Nitrogen Hybrid Gas Nanofoam Technology

2.2.1 Foundations of nanofoam in geothermal applications

Nitrogen based nanofoam technology for geothermal applications is grounded in the fluid mechanical properties of nitrogen gas combined with structurally reinforcing nanoparticles and tailored injection strategies. Nitrogen exhibits an exceptionally low viscosity of approximately $1.76 \times 10^{-5}\ Pa \cdot s$ at standard conditions, several orders of magnitude lower than water or oil based fluids, which directly reduces flow resistance during injection and circulation. Under geothermal operating conditions where pressures exceed $80\ MPa$ and temperatures surpass $300\ ^{\circ}C$, this gas phase maintains consistent and efficient transport through the fracture matrix while its low interfacial tension diminishes frictional interactions at gas liquid rock interfaces.

These characteristics support uniform flow distribution in high permeability formations such as limestone and fractured granite and avoid proppant settling or migration that can obstruct flow paths in conventional systems.

Foundational performance attributes have been investigated using simulations and laboratory studies that replicate high pressure and high temperature environments. Computational fluid dynamics and geomechanical modeling at pressures of 80 to $140\ MPa$ and temperatures of 70 to $300\ ^{\circ}C$ show that nitrogen nanofoam can maintain fracture apertures of $3\ mm$ or greater for more than 15 years equivalent time, whereas conventional proppant based completions typically degrade and close within 5 to 7 years under comparable loading.

In these simulations, embedded Al_2O_3 nanoparticles provide structural reinforcement that prevents fracture collapse under sustained mechanical and thermal stresses. Thermal simulations attribute enhanced heat transfer to the high thermal conductivity of the Al_2O_3 phase, about $30\ W\ m^{-1}\ K^{-1}$, yielding a 25 to $30\ \%$ improvement in heat extraction efficiency relative to water or oil based fluids.

Flow efficiency analyses further report that the low viscosity nitrogen matrix enables uniform flow distribution with efficiencies exceeding $90\ \%$, in contrast to about $60\ \%$ for water and $40\ \%$ for oil based systems, and project roughly $50\ \%$ reduction in reinjection frequency and associated energy demands.

Fracture stability comparisons between nanofoam and granular proppant systems underpin the mechanical foundations of this technology. Laboratory measurements show that ceramic proppants can generate about $6\ \%$ fines and frac sand up to $51\ \%$ fines under high stress, causing 75 to $98\ \%$ reductions in proppant pack porosity and conductivity losses up to $99\ \%$. In contrast, nitrogen based nanofoam does not introduce solid granular skeletons and benefits from a gas matrix that distributes pressure more uniformly within the fracture network.

Experimental work at temperatures up to $200\ ^\circ C$ and pressures of $6.9\ MPa$ demonstrates that nitrogen foams stabilized with additives, including graphene oxide, maintain foam stability significantly longer than conventional foams, with half lives of 200 to 500 hours under extreme test conditions. A technical description specifies a nitrogen nanofoam injection system with Al_2O_3 nanoparticles that sustains fracture apertures of $3\ mm$ or greater at temperatures exceeding $300\ ^\circ C$ and pressures of 80 to $140\ MPa$ through uniform gas phase pressure support and nanoparticle enhanced structural integrity. Environmental and operational compatibility form another pillar of the nanofoam foundation.

A nitrogen gas matrix comprising about $95\ \%$ of the fluid volume strongly reduces water usage relative to water based stimulation and leverages the inert character of nitrogen, which is chemically stable up to at least $300\ ^\circ C$ in contact with typical reservoir rocks. The nanofoam incorporates Al_2O_3 nanoparticles in the range 0.6 to $0.8\ \%$ by volume and silica nanoparticles between 0.3 and $0.5\ \%$ by volume, both verified as non toxic in dedicated persistence tests that report degradation times shorter than 30 days.

Environmental compatibility claims are supported by real time monitoring of formation integrity using acoustic emission measurements and geochemical analysis of extracted nitrogen gas, alongside controlled pressure gradients of 2 to $5\ MPa\ m^{-1}$ and pulsed injection frequencies of 0.1 to $1.0\ Hz$ that limit unintended fracture propagation.

AI assisted control with response times below $1\ ms$ dynamically adjusts pressure and flow rates to maintain permeabilities between 62.9 and $128.1\ D$ across shale and limestone formations, illustrating the adaptability of nanofoam to heterogeneous geological conditions. Long term stability metrics for nitrogen nanofoam hybrid gas systems further substantiate their role as a geothermal working medium.

Foam stability indices above 0.95 are reported after 1000 operational hours, supported by precise bubble size control at 1 to $5\ \mu m$ mean diameters under $150\ MPa$ homogenization, dynamic surface tension management between 20 and $30\ mN\ m^{-1}$, and controlled pressure oscillations of $\pm 5\ MPa$ at $0.1\ Hz$. These mechanisms collectively maintain nanofoam structure and, in turn, promote consistent fracture conductivity and energy recovery over extended operational periods (**5**).

2.2.2 Integration with advanced helix dual pipe geocasing technology

Integration of the nitrogen hybrid gas nanofoam with an advanced helix dual pipe geocasing technology developed by GEIOS and NANOGEIOS Laboratory relies on a coaxial architecture in which a central core chamber is surrounded by concentric nanostructured phonon conductive (NPC) chambers.

The central core functions as an open production channel dedicated to mass transport of formation fluids, while nitrogen lift gas is injected or returned through this lumen to elevate the brine, helium, and hydrogen mixture toward the surface. Surrounding chambers are used for cyclic circulation within an advanced helix dual pipe geocasing technology developed by GEIOS and NANOGEIOS Laboratory, enabling simultaneous thermal management and structural support around the production stream.

Thermodynamic placement of the production flow in the center leverages the outer circulating nanofluids as a thermal guard ring. Hot working fluids within the helical NPC chambers insulate the central nitrogen gas and brine mixture, limiting temperature loss during ascent and maintaining buoyancy of the nitrogen dominated phase.

This configuration reduces the likelihood of condensation of volatile components and supports efficient transport of entrained helium to the surface under geothermal temperature gradients. By concentrating high temperature nanofluid circulation around the core, the geocasing acts as an engineered thermal envelope that stabilizes production stream properties without requiring additional depth (**8**).

Within the annular NPC chambers, the heat exchange conduits are arranged in a helical geometry rather than a straight U-shaped configuration. This geometry substantially increases residence time and effective surface area of the GPIM Ultra ionic nanofluid in the high temperature region, thereby amplifying heat extraction from the conductive basement rock.

The GPIM Ultra fluid, containing choline based ionic species and engineered for high thermal stability and enhanced heat capacity, is designed to operate at target reservoir temperatures around $240\ ^{\circ}C$, matching the validated operating envelope of the GEIOS nanofoam system. Coupling this nanofluid with the nanofoam supported reservoir fractures provides a continuous conductive pathway from rock matrix to surface equipment (**8**,**23**,**24**).

Mechanical strength and thermal connectivity of the helix dual geocasing are provided by the NPC matrix that forms the structural backbone of the annular chambers. This matrix is a composite of hexagonal boron nitride and silicon carbide platelets dispersed within a polyphenylene sulfide polymer base, configured to act as a thermal bridge between the circulating GPIM Ultra fluid and the surrounding rock.

In parallel work on supracrystalline phonon conductive corridors, thermal conductivity along engineered corridor axes reaches about $30\ W\,m^{-1}\,K^{-1}$, with a transversely isotropic, ellipsoidal distribution of conductivity confirmed by polar measurements. Such phonon guided pathways, characterized using laser flash analysis, time domain thermoreflectance, and Brillouin spectroscopy, provide a materials basis for integrating high conductivity NPC matrices with the nanofoam stabilized fracture network (**8**,**15**,**16**).

This combined architecture directly supports the conduction dominated heat extraction strategy of the GEIOS nitrogen hybrid gas nanofoam system. Laboratory validation has shown that the nanofoam sustains fracture apertures of $3\ mm$ with only $12\ \%$ degradation over 15 weeks at 80 to $140\ MPa$ and up to $240\ ^{\circ}C$, while delivering bulk thermal conductivities near $30\ W\,m^{-1}\,K^{-1}$.

These values correspond to 166 to 336 % improvements in energy extraction metrics compared with conventional materials, and they have been achieved under highly stable flow regimes with Reynolds numbers above 10^4 and Weber numbers above 50.

Within the optimization framework for field deployment, these thermal and mechanical gains are further linked to extended maintenance intervals exceeding 10 years and energy extraction efficiency improvements of 166 to 336 % under modeled operating conditions.

Risk management for the integrated nanofoam geocasing configuration is addressed through probabilistic analysis of injection pressure and stress gradients. Injection pressure ranges of 80 to 140 MPa and operational bands of 1200 to 2000 psi are evaluated using parameter probability density functions constructed from laboratory tests, injection simulations, in situ measurements, and real time seismic mapping.

Quantiles at 1314.0, 1603.7, and 1901.2 psi delineate expected pressure conditions, while sensitivity analysis indicates that maintaining stress gradients below 0.72 $psi\,ft^{-1}$ keeps operations within acceptable risk thresholds.

Exceeding gradients of 0.77 $psi\,ft^{-1}$ may shift the system toward unacceptable risk, underscoring the need to coordinate nanofoam injection with geocasing thermal performance and seismic monitoring in future field implementations (**23**,**24**).

2.2.3 Comparative positioning against traditional EGS

Contrasts between nitrogen hybrid gas nanofoam technology and traditional water and proppant based stimulation emerge clearly when fracture stability, thermal transport, flow behaviour, and risk management metrics are compared under controlled conditions. Conventional completions rely on granular ceramic or sand proppants that undergo progressive mechanical degradation under geothermal stresses, generating approximately 6 % fines for ceramic proppants and up to 51 % fines for frac sand.

Associated porosity reductions of 75 to 98 % and fracture conductivity losses approaching 99 % reflect severe mechanical damage to the proppant pack and long term loss of transmissivity. In contrast, nitrogen nanofoam systems maintain fracture apertures of 3 mm or greater for projected periods exceeding 15 years in simulations, while descriptions specify stable apertures at 3 mm or more at temperatures above 300 $^{\circ}C$ and pressures of 80 to 140 MPa.

Laboratory validation for the GEIOS configuration reports 3 mm apertures with only 12 % degradation over 15 weeks under 80 to 140 MPa and up to 240 $^{\circ}C$, underscoring a distinct fracture stability regime relative to proppant supported systems (**5**,**23**,**24**).

Thermal transport behaviour likewise diverges between the approaches. Water based fluids in conventional EGS typically provide bulk thermal conductivities below 1.0 $W\,m^{-1}\,K^{-1}$, which constrains heat extraction. Baseline rock conductivities for common geothermal lithologies span 1.6 $W\,m^{-1}\,K^{-1}$ for shale to 2.8 $W\,m^{-1}\,K^{-1}$ for basalt. Introduction of nitrogen nanofoam with embedded Al_2O_3 nanoparticles of thermal conductivity near 30 $W\,m^{-1}\,K^{-1}$ substantially enhances effective values across all formations, with simulations indicating 25 to 30 % gains in heat extraction efficiency relative to water or oil based fluids.

For the GEIOS nanofoam system, direct measurements show bulk thermal conductivities close to 30 $W\,m^{-1}\,K^{-1}$, corresponding to 166 to 336 % improvements over conventional materials. Supracrystalline phonon conductive corridors used in related NPC matrices also reach about

$30\ W\ m^{-1}\ K^{-1}$ along preferred axes, reinforcing a conduction dominated thermal pathway strategy that departs from convective water cooling in traditional EGS (**5**,**15**,**23**,**24**).

Flow properties and operational efficiency further differentiate nanofoam based designs. Nitrogen gas exhibits an exceptionally low viscosity of approximately $1.76 \times 10^{-5}\ Pa \cdot s$ at standard conditions, several orders of magnitude below that of water or oil based fluids.

Simulations of nitrogen nanofoam in geothermal scenarios with 80 to $140\ MPa$ and 70 to $300\ ^{\circ}C$ show uniform flow distribution with efficiencies exceeding $90\ \%$, compared with about $60\ \%$ for water and $40\ \%$ for oil-based systems.

These reductions in frictional loss translate into lower pumping energy and enable broader injection pressure ranges, 80 to $140\ MPa$ or 1200 to $2000\ psi$, to be safely explored within probabilistic risk frameworks. Uncertainty analyses for GEIOS assign quantiles at 1314.0, 1603.7, and $1901.2\ psi$ to characterize expected operating regimes, whereas conventional completions are not reported with comparable adaptive pressure envelopes.

In addition, simulations project about $50\ \%$ reduction in reinjection frequency for nanofoam systems relative to proppant-based designs, linking hydraulic efficiency to operational longevity (**5**,**23**,**24**). Risk characterization and induced seismicity considerations also contrast sharply. Conventional water and proppant stimulation couples fines generation, proppant crushing, and heterogeneous pressure dissipation due to the relative incompressibility and high viscosity of water, producing localized overpressure and collapsed zones within the fracture network. These conditions elevate mechanical degradation and complicate pressure management.

Nitrogen nanofoam alternatives eliminate granular proppant skeletons and exploit a gas matrix that distributes pressure more uniformly, while explicit sensitivity analyses define stress gradient thresholds of $0.72\ psi\ ft^{-1}$ for acceptable risk and above $0.77\ psi\ ft^{-1}$ for potentially unacceptable regimes. Seismic evaluation tools and real time seismic mapping are built into GEIOS workflows, with uncertainty assessment integrating well logs, seismic data, and laboratory validation to refine formation specific stability indices.

Although such frameworks cannot reproduce reservoir scale fault slip, they provide a structured basis for comparing nanofoam and traditional EGS in terms of risk reduction and highlight the need for continued field scale microseismic monitoring to validate apparent benefits (**23**,**24**,**5**).

2.3 Seismic Risk in Geothermal Energy

2.3.1 Definition and types of induced seismicity

In geothermal contexts, induced seismicity arises when engineering operations perturb in situ stress, pore pressure, or rock fabric sufficiently to trigger detectable mechanical events. Acoustic emission and micro-seismic monitoring used in nanofoam and SPARC related experiments provide a quantitative basis for distinguishing classes of induced events by their energy, frequency content, and temporal relation to loading or injection phases. Directional acoustic emission measurements under controlled loading conditions show that SPARC treated samples experience a $49\ \%$ reduction in total acoustic emission events relative to controls, together with a $59\ \%$ reduction in average event energy and a $42\ \%$ reduction in event duration. Average amplitudes decrease by $13\ \%$, counts by $51\ \%$, while average event frequency increases by $83\ \%$.

Events can be partitioned into those occurring during loading, plateau, and failure phases, with SPARC treated materials exhibiting fewer high energy events during the failure phase. This pattern has been interpreted as a shift from sporadic large events toward more frequent, lower

energy micro failures, which represent a more distributed damage regime rather than abrupt macroscopic fracture.

Within this framework, several operationally relevant types of induced seismicity can be delineated.

Low energy micro-seismicity corresponds to the abundant, low amplitude, high frequency acoustic emission associated with distributed microcracking and pore scale adjustment during injection or mechanical loading.

In the SPARC treated samples, this class dominates the response and accumulates more slowly over time than in untreated controls, as indicated by the slower growth of cumulative events and the higher characteristic frequencies reported in the acoustic emission analysis. A second type involves intermediate events concentrated near the transition from plateau to failure, which reflect the coalescence of microcracks into localized shear or tensile zones. These events carry higher energy and longer durations than background micro-seismicity but still fall short of macroscopic specimen scale failure.

Finally, the failure phase is marked by relatively few but energetically dominant events in untreated materials, which correspond to catastrophic fracture; SPARC treatment reduces the number and energy of such events, leading to a more controlled failure mechanism.

Nitrogen based flow tests further refine the classification by linking induced events to specific hydromechanical drivers. Directional permeability measurements conducted with steady state nitrogen gas flow at confining pressures between 5 and $20\ MPa$ allow separation of pressure driven microseismicity, associated with transient pore pressure gradients and gas slippage, from structurally controlled events that emerge as permeability anisotropy evolves.

Application of Darcy based analysis with Klinkenberg correction constrains permeability changes and, when combined with time dependent measurements before and after reaction experiments, differentiates events tied to reversible permeability evolution from those signalling irreversible damage. Transient pulse decay tests, in which a pressure pulse is applied and pressure decay is monitored, provide an additional diagnostic of pore pressure diffusivity and enable identification of events associated with rapid pressure redistribution versus slower, diffusion controlled adjustment (**16**).

In systems explicitly designed for geothermal operation, such as the GEIOS nitrogen hybrid gas nanofoam configuration, induced seismicity characterization is embedded in broader risk assessment workflows. Seismic evaluation tools and real time seismic mapping are used alongside laboratory validation, injection simulations, and well log data to construct formation specific seismic sensitivities and a seismic risk matrix. For granite, basalt, and limestone, reported seismic sensitivity factors of 0.3, 0.4, and 0.6, respectively, are combined with permeability, operational pressure ranges, fracture stability indices, and film strength to classify the likelihood and severity of induced seismic events under nanofoam supported operation.

These metrics distinguish relatively stable regimes, where induced activity is expected to remain limited to low energy microseismicity, from higher risk conditions in which larger events may be triggered (**23**). Despite these detailed classifications, research explicitly acknowledges that high pressure, high temperature chamber experiments and associated acoustic emission measurements cannot reproduce reservoir scale fault slip or fully capture the complexity of natural fault networks.

Consequently, field scale microseismic monitoring, using distributed seismic arrays and long term observation of induced event populations, is identified as essential for validating laboratory inferred reductions in seismic energy release and for refining formation specific stability indices and seismic sensitivity parameters under actual reservoir conditions (**23**,**24**).

2.3.2 Drivers of seismicity in subsurface energy extraction

Induced seismicity during subsurface energy extraction is primarily driven by how engineering operations perturb in situ stress and pore pressure, interact with fracture networks, and modify rock mechanical properties over time. Conventional water based hydraulic stimulation with granular proppants couples several of these drivers.

(See Section 2.1.2 for detailed discussion of proppant fines generation.)

These processes create zones with strong stiffness contrasts and localized stress concentrations that can interact with existing fractures and faults. Sustained injection of viscous, largely incompressible water maintains elevated pore pressures, particularly where fines accumulation and compaction impede drainage, so segments of the fracture network may remain overpressured while neighboring zones close.

This heterogeneous pressure field and associated effective stress redistribution are key seismicity drivers in traditional water proppant operations. Hydraulic forcing and pore pressure evolution also influence seismic hazard in nitrogen based systems, but the underlying mechanisms differ. Nitrogen gas has an exceptionally low viscosity of approximately $1.76 \times 10^{-5}\ Pa \cdot s$ at standard conditions, several orders of magnitude below water or oil based fluids, and does not introduce a granular skeleton into the fracture network.

These properties promote more uniform flow distribution and reduce frictional pressure losses in complex fractures, thereby diminishing localized overpressurization. In geothermal applications where pressures exceed $80\ MPa$ and temperatures surpass $300\ ^{\circ}C$, nitrogen based nanofoam maintains consistent transport while avoiding proppant settling or migration that would otherwise generate mechanical heterogeneities.

Because no solid proppant is present, there is no pathway for fines generation or proppant pack compaction, and thus one of the principal contributors to long term stress concentration and induced seismic susceptibility in conventional systems is removed (**5**). Seismic risk in the GEIOS nitrogen hybrid gas nanofoam configuration is characterized explicitly through dedicated uncertainty analyses and seismic evaluation tools. Stress gradients are treated as primary control variables for fracture stability and seismic hazard. Sensitivity studies identify that maintaining a stress gradient below $0.72\ psi\,ft^{-1}$ keeps operation within acceptable risk thresholds, whereas gradients above $0.77\ psi\,ft^{-1}$ may shift the system into unacceptable risk regimes even when other parameters are optimized. Injection pressure ranges from 80 to $140\ MPa$ and operational bands of 1200 to $2000\ psi$ are represented by probability density functions constructed from laboratory validation tests, in situ measurements, injection simulations, well logs, and real time seismic mapping.

Quantiles at 1314.0, 1603.7, and $1901.2\ psi$ delineate lower, median, and upper expected operating pressures, and are used to evaluate how variations in pressure may influence the likelihood of test failure or instability.

Dynamic adjustments to nitrogen injection rate and nanoparticle composition within this pressure envelope are proposed as mitigation levers to sustain fracture stability and thermal efficiency

while constraining seismic risk. Formation specific properties introduce additional drivers that must be resolved when assessing induced seismicity.

For granite, basalt, and limestone, seismic sensitivity factors of 0.3, 0.4, and 0.6, respectively, are combined with permeability, operational pressure ranges, fracture stability indices, and film strength into a seismic risk matrix for nanofoam supported operation.

This framework distinguishes conditions where induced activity is expected to remain limited to low energy microseismicity from higher risk scenarios where larger events could occur. Rock interaction studies under nanofoam injection show interface adhesion strength of $2.8\ MPa$, formation damage factors below 0.15, and preservation of more than $92\ \%$ of original permeability and greater than $95\ \%$ of porosity, indicating that the nanofoam maintains fracture conductivity without significant damage to rock fabric that might otherwise evolve into mechanically weak zones.

These characteristics reduce one potential pathway for seismic hazard growth, namely progressive formation degradation around engineered fractures (**23**,**24**).

Despite these laboratory and modeling-based risk characterizations, experiments conducted in high pressure, high temperature chambers cannot reproduce reservoir scale fault slip or capture the full complexity of natural fault networks.

Research on the GEIOS nanofoam system therefore identifies continuous field scale micro-seismic monitoring, using real time seismic mapping and long-term observation of induced event populations, as essential for validating the apparent reductions in seismic drivers inferred from controlled tests and for refining formation specific stability indices and seismic sensitivity parameters under actual reservoir conditions (**23**,**24**,**5**).

3 Theoretical Framework

3.1 Mechanistic Drivers of Induced Seismicity

3.1.1 Pore-pressure mechanism

Pressurized injection of working fluids perturbs pore pressure and effective stress, thereby influencing induced seismicity in subsurface systems. In conventional water based hydraulic stimulation with granular proppants, the combination of high viscosity, relative incompressibility, and fines generation leads to heterogeneous and often sustained overpressures within the fracture network.

Laboratory measurements show that ceramic and sand proppants generate about $6\ \%$ and up to $51\ \%$ fines, respectively, accompanied by 75 to $98\ \%$ reductions in proppant pack porosity and fracture conductivity losses approaching $99\ \%$ under high stress conditions.

These changes create strongly compacted zones that impede pressure dissipation, so segments of the fracture network remain overpressured while other regions close, reinforcing localized stress concentrations that can act as seismicity drivers.

Nitrogen based nanofoam operates under a different pore pressure regime. Nitrogen gas exhibits an exceptionally low viscosity of approximately $1.76 \times 10^{-5}\ Pa \cdot s$ at standard conditions, several orders of magnitude lower than water or oil based fluids, and does not introduce a granular skeleton into the fracture network.

Under geothermal conditions where operational pressures exceed $80\ MPa$ and temperatures surpass $300\ ^{\circ}C$, nitrogen supports consistent and efficient fluid transport through the fracture matrix, with low interfacial tension reducing frictional interactions among gas, liquid, and rock phases.

The gas matrix distributes pressure more uniformly, and the absence of proppant eliminates fines generation and proppant pack compaction as mechanisms for creating long lived pressure bottlenecks. In patent oriented and experimental descriptions, nitrogen nanofoam systems maintain fracture apertures of $3\ mm$ or greater at 80 to $140\ MPa$, relying on gas phase pressure support and nanoparticle reinforced structure rather than wedged granular packs, which further reduces the likelihood of spatially concentrated pore pressure anomalies (**5**).

Within the GEIOS framework, pore pressure and stress parameters are treated explicitly in probabilistic uncertainty analyses. Injection pressure ranges of 80 to $140\ MPa$ and operational bands of 1200 to $2000\ psi$ are represented by probability density functions constructed from laboratory validation tests, in situ measurements, injection simulations, well logs, and seismic data.

Quantiles at 1314.0, 1603.7, and $1901.2\ psi$ characterize lower, median, and upper expected operating conditions, and are used to assess how pressure variations influence the risk of test failure. Sensitivity studies identify stress gradient thresholds, indicating that maintaining a gradient below $0.72\ psi\ ft^{-1}$ keeps operations within acceptable risk domains, whereas gradients above $0.77\ psi\ ft^{-1}$ may correspond to unacceptable risk even when other parameters are optimized.

These results link pore pressure control directly to risk characterization and highlight dynamic adjustments of nitrogen injection rate and nanoparticle composition as levers for keeping pore pressure perturbations within specified bounds.

Formation interface analyses provide additional constraints on how nanofoam supported pore pressure changes interact with rock fabric. Rock interaction studies report an interface adhesion strength between injected nanofoam and reservoir rock of $2.8\ MPa$, a formation damage factor below 0.15, preservation of more than $92\ \%$ of original permeability, and porosity retention above $95\ \%$ after injection.

These metrics indicate that nanofoam induced pore pressure transients do not significantly degrade rock structure under tested conditions, and that fractures remain open with sustained fluid flow capacity. Long term stability tests further show performance retention exceeding $94\ \%$ after 1000 hours of operation, and fracture apertures of $3\ mm$ experiencing only $12\ \%$ degradation over 15 weeks at 80 to $140\ MPa$ and up to $240\ ^{\circ}C$. Together, these observations suggest that pore pressure perturbations in the nanofoam system are compatible with maintaining fracture stability and formation integrity over extended laboratory time scales (**23**,**24**).

Acoustic emission and microseismic monitoring in SPARC related experiments complement this picture by linking controlled pore pressure and stress changes to reduced seismic energy release. Directional acoustic emission measurements show a $49\ \%$ reduction in total events, a $59\ \%$ reduction in average energy, a $42\ \%$ reduction in event duration, and a $51\ \%$ reduction in counts for SPARC treated samples relative to controls, along with an $83\ \%$ increase in average frequency.

Event classification reveals fewer high energy events during the failure phase, consistent with a more distributed, lower energy failure regime under controlled hydromechanical conditions. Permeability testing in these samples uses steady state nitrogen gas flow at confining pressures from 5 to $20\ MPa$, applying Darcy based analysis with Klinkenberg correction, and transient pulse

decay tests to assess pore pressure diffusivity and verify steady state measurements. These methods demonstrate that nitrogen-based configurations can sustain permeability while limiting high energy failure events as pore pressure is varied, although they do not reproduce reservoir scale fault slip or complex natural fault networks (**16**).

Research on the GEIOS nanofoam system therefore emphasizes that, despite favorable laboratory indications of more uniform pressure distribution and reduced high energy seismic responses, field scale micro-seismic monitoring remains essential. Uncertainty assessments explicitly incorporate real time seismic mapping to refine formation specific stability indices and seismic sensitivity parameters under actual reservoir conditions, acknowledging that laboratory high pressure, high temperature chambers cannot capture all aspects of pore pressure driven fault activation at scale (**23**,**24**,**16**).

3.1.2 Thermo-elastic mechanism

Thermally driven stress evolution in engineered geothermal systems depends on how heat is transported between the rock matrix and the working fluid. Conventional water-based stimulation relies primarily on convective cooling of the formation, with low fluid thermal conductivity below about 1.0 W m^{-1} K^{-1} and baseline rock conductivities that vary by lithology (Table 16). This configuration promotes substantial temperature gradients across the reservoir volume and associated thermo-elastic stressing as cooled rock contracts next to hotter, unstimulated regions (5).

Nitrogen hybrid gas nanofoam is designed around a different thermal regime, in which heat extraction is dominated by conduction along engineered high-conductivity pathways rather than bulk convective cooling of large rock volumes. Simulations and laboratory measurements attribute the enhanced heat transfer to Al_2O_3 nanoparticles with thermal conductivity near 30 W m^{-1} K^{-1}. In nanofoam simulations, these particles increase heat extraction efficiency by approximately 25–30% relative to conventional water or oil-based fluids, while maintaining fracture apertures of at least 3 mm under pressures of 80–140 MPa and temperatures up to 300 °C.

In the GEIOS configuration, bulk thermal conductivity near 30 W m^{-1} K^{-1} has been measured in a high-pressure, high-temperature chamber up to 240 °C, corresponding to 166–336% improvements over conventional materials used in comparable settings. Supracrystalline phonon-conductive corridors in related nanostructured matrices also reach about 30 W m^{-1} K^{-1} along preferred axes, with a pronounced ellipsoidal conductivity distribution consistent with transversely isotropic media. Table 16 consolidates the thermal conductivity hierarchy from baseline rock through conventional fluids to the nanofoam and SPARC corridor systems, and Table 17 and Table 18 summarizes the consequent thermo-mechanical implications for each regime.

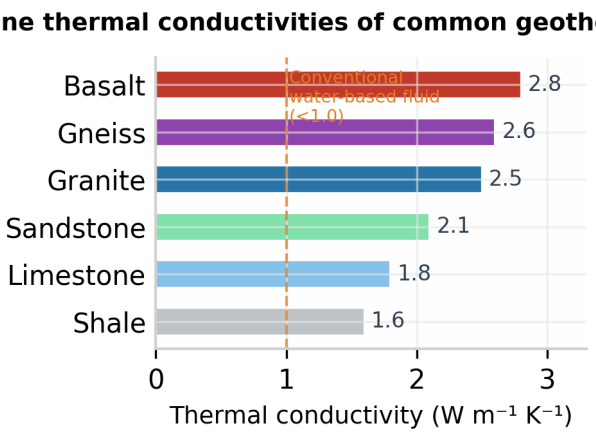

Figure 2. *Baseline thermal conductivities of common geothermal lithologies (shale to basalt), with the conventional water-based fluid reference indicated by the dashed line at 1.0 W m⁻¹ K⁻¹. Values represent intact, dry specimens at ambient conditions.*

Table 1. Baseline thermal conductivities of common geothermal lithologies.

Lithology	Thermal conductivity (W m⁻¹ K⁻¹)	Refs
Shale	~1.6	(5)
Limestone	~1.8–2.0	(5)
Sandstone	~2.0–2.3	(5)
Granite	~2.4–2.6	(5)
Gneiss	~2.5–2.7	(5)
Basalt	~2.6–2.8	(5)

Note: Values represent typical ranges for intact, dry specimens at ambient conditions; in-situ values may vary with porosity, saturation, and temperature.

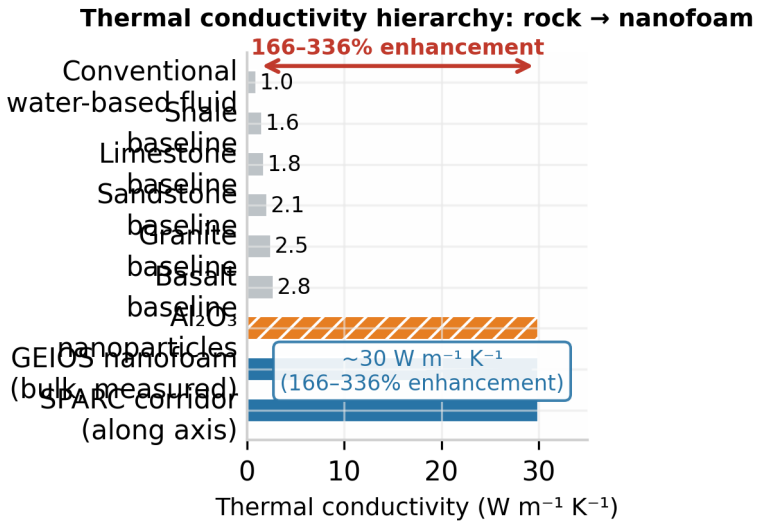

Figure 3. *Thermal conductivity hierarchy from conventional water-based fluid through rock baselines to the GEIOS nanofoam and SPARC corridor systems, demonstrating the 166–336% enhancement achieved by engineered conduction pathways.*

Table 2. Thermal conductivity hierarchy: from baseline rock and conventional fluids to GEIOS nanofoam and SPARC corridors.

Material / System	**Thermal conductivity (W m⁻¹ K⁻¹)**	**Enhancement vs. conventional fluid (<1.0 W m⁻¹ K⁻¹)**	**Validated conditions**	**Refs**
Conventional water-based fluid	<1.0	Baseline	Ambient to geothermal P–T	(5)
Baseline rock (shale–basalt range)	1.6–2.8	—	Ambient	(5)
Al_2O_3 nanoparticles (intrinsic)	~30	—	—	(23)
GEIOS N_2 nanofoam (bulk, measured)	~30	+166 to +336%	80–140 MPa; up to 240 °C	(23,24)
SPARC phonon-conductive corridors	~30 (along preferred axis)	+166 to +336%	Ellipsoidal distribution; transversely isotropic	(15,16)
Nanofoam simulation (heat extraction efficiency gain)	—	+25 to +30% vs. water/oil fluids	80–140 MPa; up to 300 °C	(23)

Table 3. Thermo-mechanical regime comparison: convective cooling versus conduction-dominated extraction.

Parameter	Conventional convective cooling	GEIOS conduction-dominated nanofoam	Refs
Primary heat transfer mode	Convective cooling of bulk rock volume	Conduction along nanoparticle-mediated pathways	(5,23)
Fluid thermal conductivity (W m^{-1} K^{-1})	<1.0	~30 (bulk nanofoam)	(5,23,24)
Temperature gradient regime	Large gradients across reservoir; cooled rock adjacent to hot unstimulated zones	Minimised gradients; heat channelled along high-*k* corridors	(5,15,23)
Thermo-elastic stress consequence	Substantial contraction mismatch → elevated thermo-elastic stressing	Reduced contraction mismatch → lower thermo-elastic stress concentrations	(5,15,23)
Fracture aperture maintained	Progressive closure (5–7 yr)	≥3 mm; stable at 80–140 MPa, up to 300 °C	(5,23,24)
Heat extraction efficiency gain	Baseline	+25 to +30% (simulation); +166 to +336% conductivity enhancement (measured)	(23,24)
Conductivity anisotropy (SPARC)	N/A	~30 W m^{-1} K^{-1} along preferred axis; ellipsoidal, transversely isotropic	(15,16)

These measurements, obtained by laser flash analysis, time domain thermoreflectance, and Brillouin spectroscopy, demonstrate that engineered conduction pathways can concentrate heat transfer along specific directions without requiring large scale convective cooling of the surrounding rock volume (**5**,**15**,**23**,**24**).

Within this conduction focused framework, the nitrogen gas matrix functions mainly as a carrier for nanoparticles and as a pressure support medium, while the high conductivity solid network provides the primary route for thermal transport.

Simulations show that the nanofoam forms relatively uniform thermal gradients and maintains flow efficiencies above $90\ \%$ due to the low nitrogen viscosity of approximately $1.76 \times 10^{-5}\ Pa \cdot s$. The foam's gas matrix ensures uniform pressure distribution within fractures and avoids granular skeletons that could generate local mechanical stress concentrations comparable to proppant wedging.

A description specifies that the nitrogen based nanofoam, incorporating Al_2O_3 nanoparticles, maintains fracture apertures of $3\ mm$ or greater at temperatures exceeding $300\ ^{\circ}C$ and pressures between 80 and $140\ MPa$ through gas phase pressure support and nanoparticle enhanced structural integrity.

In this configuration, thermal transport is achieved while preventing mechanical degradation and preserving sustained fracture conductivity, a combination that can be interpreted as avoidance of bulk thermo elastic stressing of the rock matrix compared with conventional convective cooling approaches (**5**).

Risk characterization in the GEIOS nanofoam program couples these thermo mechanical considerations to probabilistic analyses of pressure and stress. Injection pressures spanning 80 to $140\ MPa$ and operational bands of 1200 to $2000\ psi$ are represented by probability density functions built from laboratory tests, in situ measurements, injection simulations, well logs, and seismic data. Quantiles at 1314.0, 1603.7, and $1901.2\ psi$ delineate expected operating conditions, and sensitivity studies show that maintaining a stress gradient below $0.72\ psi\ ft^{-1}$ keeps operation within acceptable risk thresholds, whereas gradients above $0.77\ psi\ ft^{-1}$ may correspond to unacceptable risk even when other parameters are optimized.

These analyses evaluate pore pressure and stress consistency together with thermal performance, linking the conduction-based heat extraction strategy to overall induced seismicity risk rather than treating thermal and mechanical effects in isolation (**23**,**24**).

Despite these advances, all reported results derive from simulations and high pressure, high temperature chamber experiments that cannot reproduce reservoir scale fault slip or capture the full complexity of natural fault networks.

Research on nitrogen nanofoam and supra-crystalline conductive matrices therefore identifies continuous field scale micro-seismic monitoring, combined with refinement of formation specific stability indices and seismic sensitivities, as essential for validating laboratory inferred avoidance of bulk thermo elastic stressing and for quantifying any residual thermo-mechanical contribution to induced seismicity under actual reservoir conditions (**23**,**24**,**5**,**15**).

3.1.3 Proppant-induced stress concentration

Granular proppants subjected to geothermal stress conditions undergo severe mechanical degradation that directly generates localized stress concentrations along fractures. Laboratory measurements report fines generation of approximately $6\ \%$ for ceramic proppants and up to $51\ \%$ for frac sand under loading, accompanied by 75 to $98\ \%$ reductions in proppant pack porosity and fracture conductivity losses approaching $99\ \%$ in high stress environments.

These changes arise from grain crushing, compaction, and embedment within fracture asperities, processes that transform initially permeable proppant packs into dense, stiff clusters.

Such clusters function mechanically as heterogeneities within the fracture, capable of focusing stresses and altering the local stiffness contrast relative to surrounding rock and fluid filled regions.

Flow behavior in conventional water and proppant systems further reinforces these mechanically induced heterogeneities. Water or oil-based fracturing fluids possess much higher viscosities than nitrogen gas, sustaining elevated pore pressures over longer durations, particularly where fines accumulation and compaction impede drainage.

Under geothermal operating conditions with pressures above $80\ MPa$ and temperatures exceeding $300\ ^{\circ}C$, segments of the proppant filled fracture network may remain overpressured while other zones close, establishing sharp gradients in effective stress.

Evidence indicates that proppant settling, migration, and mechanical embedment contribute to blocked or partially clogged segments, which intensify local pressure gradients and increase the potential for stress concentration along contact interfaces.

These coupled hydraulic and mechanical effects represent an important pathway by which conventional water proppant stimulation can promote proppant induced stress concentration and associated induced seismicity drivers. Nitrogen based nanofoam avoids the presence of a granular skeleton and therefore removes the specific mechanism of grain wedging that characterizes conventional proppants.

Simulations using advanced computational fluid dynamics and geo-mechanical models at pressures of 80 to $140\ MPa$ and temperatures between 70 and $300\ ^{\circ}C$ show that nitrogen nanofoam maintains fracture apertures of $3\ mm$ or greater for over 15 years equivalent time, whereas conventional proppant-based completions typically degrade and close within 5 to 7 years. In these simulations, embedded Al_2O_3 nanoparticles provide structural reinforcement without forming discrete, crushable grains; the low viscosity nitrogen matrix, with viscosity around $1.76 \times 10^{-5}\ Pa \cdot s$ at standard conditions, distributes pressure uniformly across the fracture network and reduces frictional losses.

The description specifies a nitrogen nanofoam injection system operating effectively at temperatures exceeding $300\ ^{\circ}C$ and pressures between 80 and $140\ MPa$, where gas phase pressure support combined with nanoparticle enhanced structural integrity maintains fracture apertures of $3\ mm$ or greater and prevents mechanical degradation that would otherwise concentrate stresses at localized contact points. Performance summaries from simulation studies quantify how the absence of granular proppant modifies long term mechanical behavior.

Nitrogen nanofoam achieves fracture stability lifetimes exceeding 15 years, compared with 5 to 7 years for conventional proppants, and reaches flow efficiencies near $90\ \%$, in contrast to approximately $30\ \%$ for proppant supported systems. Reinjection frequency is projected at every 10 to 15 years for nanofoam, versus 3 to 5 years for proppant based designs, reflecting reduced fracture closure and less cumulative mechanical damage.

Thermal conductivity also differs markedly: nanofoam reaches about $30\ W\ m^{-1}\ K^{-1}$, while conventional proppant packs are reported in the range 1 to $5\ W\ m^{-1}\ K^{-1}$, and water based fluids around $0.6\ W\ m^{-1}\ K^{-1}$. Although these thermal metrics primarily address heat transfer, the associated ability to sustain open, uniformly loaded fractures without dense proppant clusters further reduces opportunities for localized proppant induced stress concentration. Moreover, nitrogen gas does not introduce solid residues, eliminating the risk that settled or migrated solids will create mechanically stiff inclusions that obstruct flow paths and amplify local stresses.

Collectively, these observations indicate that replacing granular proppants with nitrogen nanofoam substantially mitigates, but does not eliminate, the specific class of stress concentration mechanisms associated with proppant crushing, compaction, and embedment (**5**). Despite these advantages, all reported findings derive from simulations and laboratory experiments rather than reservoir scale deployments. Research on nitrogen nanofoam therefore emphasizes that field scale micro-seismic monitoring remains essential to confirm that the reductions in proppant induced stress concentration observed under controlled conditions translate into a measurably lower induced seismicity risk profile in operational geothermal reservoirs (**5**,**23**,**24**).

3.2 Comparative Seismic Risk Pathways

3.2.1 Mapping mechanisms to seismic risk profiles

Mapping the mechanistic pathways described above onto seismic risk profiles requires relating fluid, thermal, and structural behaviors to measurable indicators such as pressure ranges, stress gradients, and formation specific sensitivities. For the GEIOS nitrogen hybrid gas nanofoam configuration, uncertainty analysis explicitly represents injection pressure as a probabilistic variable, with an operational band of 1200 to $2000\,psi$ and quantiles at 1314.0, 1603.7, and $1901.2\,psi$ that delimit lower, median, and upper expected conditions. These ranges are evaluated together with an injection pressure interval of 80 to $140\,MPa$ to capture variability across reservoir types.

Within this parameter space, risk characterization focuses on how departures toward the extremes might jeopardize fracture stability or thermal efficiency and how dynamic adjustments of nitrogen injection rate and nanoparticle composition can be used as mitigation levers. Stress gradient thresholds furnish a second axis for mapping mechanisms to risk. Sensitivity analyses identify that maintaining a stress gradient below $0.72\,psi\,ft^{-1}$ keeps operation within acceptable risk domains, whereas gradients above $0.77\,psi\,ft^{-1}$ may correspond to unacceptable risk, even when other parameters remain favorable.

These thresholds condense the combined effects of pore pressure perturbation, fracture stability, and formation properties into a concise criterion for operational decision making. They also provide a bridge between laboratory scale testing and field scale design, because they can be compared directly with gradients inferred from well logs and in situ stress measurements when configuring injection protocols (**23**,**24**).

Formation specific parameters further refine seismic risk profiles by linking the mechanistic action of nanofoam and conduction based heat extraction to lithology dependent sensitivities. Reported performance data for granite, basalt, and limestone assign permeability values of 105.6, 94.3, and $128.1\,D$, respectively, pressure ranges tailored to each formation, fracture stability indices between 88 and 92, film strengths from 65 to $75\,MPa$, and seismic sensitivity factors of 0.3, 0.4, and 0.6.

These quantities are combined into a seismic risk matrix and a formation stability index that together describe both likelihood and severity of induced events under nanofoam supported operation. Lower seismic sensitivity values for granite relative to limestone, for example, encode how the same pressure and stress gradient conditions can map onto different risk categories depending on rock type (**23**).

Risk mapping also incorporates explicit consideration of degradation and stability metrics for the nanofoam filled fractures themselves. During a 15 week high pressure, high temperature chamber program, an initial fracture aperture of $3\,mm$ experienced only $12\,\%$ total degradation, consistent with a linear degradation law $D(n) = D_0 + kn$ and a degradation rate coefficient k below $0.006\,\%$ per cycle.

Thermal performance during these tests showed nanofoam thermal conductivity near $30\,W\,m^{-1}\,K^{-1}$, representing a 166 to $336\,\%$ improvement over conventional materials. These stability and conductivity metrics enter the risk framework by constraining the probability that fractures will close or lose capacity within the modeled pressure and stress ranges, which would in turn modify pore pressure distribution and stress transfer in ways relevant to induced seismicity.

Seismic evaluation tools and microseismic information are treated as core inputs rather than ancillary data streams when constructing these risk profiles. Uncertainty assessments for the nanofoam system aggregate laboratory validation tests, in situ measurements, reservoir drilling and completion logs, injection simulations, and real time seismic mapping into parameter probability density functions.

This data integration supports evaluation of pore pressure and stress consistency with tectonic constraints, lithology based differentiation of stress tests, and calibration of fracture aperture stability, porosity, and nanoparticle dispersion using empirical relationships where direct measurements are unavailable. Seismic monitoring outcomes are then used to refine model parameters iteratively, tightening uncertainty ranges where observations support it and broadening them where data remain sparse (**23**,**24**).

Despite the sophistication of these probabilistic frameworks, current mappings from mechanism to seismic risk remain anchored in simulations and high pressure, high temperature chamber experiments that cannot reproduce reservoir scale fault slip or the complexity of natural fault networks.

Research on both the GEIOS nitrogen hybrid gas nanofoam system and related SPARC based conductive materials therefore identifies continuous field scale microseismic monitoring as indispensable for validating laboratory inferred reductions in high energy events and for updating formation specific stability indices and seismic sensitivity factors under operational conditions (**23**,**24**,**16**).

3.2.2 Integrated risk mitigation potential

Integrated risk mitigation in the GEIOS nitrogen hybrid gas nanofoam configuration arises from coupling probabilistic pressure control, formation specific sensitivity assessment, and continuous seismic evaluation within a single operational framework.

Injection pressure is explicitly treated as a random variable, with an assigned band of 1200 to $2000\ psi$ and quantiles at 1314.0, 1603.7, and $1901.2\ psi$ representing lower, median, and upper expected operating conditions.

These values are mapped onto an injection pressure interval of 80 to $140\ MPa$ to capture variability across reservoir types and to bound scenarios where low pressures may jeopardize fracture stability or high pressures may approach instability limits. Within this space, dynamic adjustments to nitrogen injection rate and nanoparticle composition are identified as primary levers to maintain fracture apertures and thermal transfer while constraining the likelihood of test failure.

Stress gradient thresholds provide a second, complementary control axis. Sensitivity analyses show that maintaining a stress gradient below $0.72\ psi\ ft^{-1}$ keeps operations within acceptable risk domains, whereas gradients above $0.77\ psi\ ft^{-1}$ may push the system into unacceptable risk regimes even if other parameters remain favorable.

These thresholds condense the combined effects of pore pressure perturbation, fracture stability, and tectonic setting into a compact operational criterion. Because they are defined in terms of measurable gradients, they can be enforced directly in design and real time control and thereby serve as a mechanistic link between pressure management and induced seismicity risk reduction. Formation dependent performance parameters further tailor mitigation strategies to lithology. For granite, basalt, and limestone, formation specific tables report permeability of 105.6, 94.3, and $128.1\ D$, pressure ranges of 120 to 130, 110 to 125, and 80 to $110\ MPa$, fracture stability indices

of 92, 90, and 88, film strengths of 75, 70, and $65\ MPa$, and seismic sensitivity factors of 0.3, 0.4, and 0.6, respectively.

These parameters are combined into a seismic risk matrix and a formation stability index that capture both the likelihood and severity of induced seismic activity for each lithology. Lower seismic sensitivity for granite relative to limestone, for example, encodes that the same pressure and stress gradient conditions map onto different risk categories, enabling lithology dependent tuning of injection protocols and monitoring intensity.

Mitigation potential also depends on maintaining mechanical and thermal performance of nanofoam supported fractures within narrow degradation bounds. Laboratory validation in a high pressure, high temperature chamber demonstrates that a $3\ mm$ fracture aperture exhibits only $12\ \%$ degradation over extended testing at pressures between 80 and $140\ MPa$ and temperatures up to $240\ ^{\circ}C$.

Under these conditions, the nanofoam attains thermal conductivity near $30\ W\ m^{-1}\ K^{-1}$, representing a 166 to $336\ \%$ improvement over conventional materials. The system also tolerates pressure variations of $\pm 5\ MPa$ without loss of stability. These performance metrics support risk mitigation by reducing the probability of mechanically driven aperture collapse or severe thermal efficiency loss within the modeled pressure and stress ranges, which would otherwise alter pore pressure distribution and stress transfer in directions unfavorable for seismic control.

Data integration and monitoring complete the mitigation framework. Uncertainty assessment consolidates information from reservoir drilling and completion logs, nanofoam laboratory validation tests, injection simulations, in situ measurements, and real time seismic mapping into parameter probability density functions. When direct measurements are unavailable, empirical relationships are used, for example constraining the poroelastic coefficient to $[0,0.5]$ based on theoretical bounds.

Broader uncertainty ranges are applied where data are sparse, such as an 80 to $140\ MPa$ injection pressure range and 40 to $70\ nm$ particle spacing, ensuring that modeled risk remains conservative. Pore pressure and stress consistency with fracture stability and tectonic constraints is evaluated iteratively, and stress tests are differentiated by lithology to refine predictions of fracture behavior and thermal response. Seismic evaluation tools feed observed microseismic activity back into this probabilistic architecture, improving calibration of fracture stability indices, porosity evolution, and nanoparticle dispersion parameters over time (**23**,**24**). Despite these integrated measures, research on the nanofoam system explicitly acknowledges that all current risk mitigation conclusions are derived from simulations and high pressure, high temperature chamber experiments, which cannot reproduce reservoir scale fault slip or the complexity of natural fault networks.

Consequently, continuous field scale microseismic monitoring, incorporating real time seismic mapping and long term observation of induced event populations, is identified as essential for validating the apparent reductions in high energy events and for updating formation specific stability indices and seismic sensitivity factors under operational reservoir conditions (**23**,**24**,**16**).

4 Materials and Methods

4.1 Laboratory Apparatus and Configuration

4.1.1 High-pressure/high-temperature chamber setup

High pressure and high temperature characterization of the nitrogen hybrid gas nanofoam relied on a dedicated test chamber designed to replicate geothermal reservoir conditions while enabling Multiphysics monitoring. The central vessel was fabricated from Inconel 718 alloy, providing corrosion resistance and mechanical integrity at pressures between 80 and $140\ MPa$ and temperatures from 70 to $300\ ^{\circ}C$, with pressure stability better than $\pm 0.1\ MPa$ and temperature control within $\pm 1\ ^{\circ}C$ across the working range.

Optical access through sapphire viewing ports allowed high resolution visualization of nanofoam structure evolution and particle dynamics at temperatures up to $240\ ^{\circ}C$, while the chamber geometry was adapted to accommodate fractured rock samples representative of granite, basalt, and limestone. Pressure regulation employed a closed loop system with dual monitoring: strain gauge transducers and crystal quartz sensors, each providing microsecond response times and redundant verification of chamber pressure. This configuration enabled controlled application of both static and dynamic pressure conditions, including stepwise sweeps across the 80 to $140\ MPa$ injection interval used for uncertainty analysis and risk characterization. Continuous logging of pressure data at sampling rates up to $10\ kHz$ ensured that transient responses of the nanofoam to imposed pressure changes were captured with high fidelity (**24**,**23**).

Thermal management was achieved through a multi zone heating architecture integrated around the Inconel 718 vessel. Band heaters and distributed elements maintained spatially uniform temperatures between 70 and $300\ ^{\circ}C$, while fiber optic sensing arrays provided distributed temperature measurements within the chamber volume.

These arrays were complemented by high resolution infrared imaging through the sapphire ports, which enabled direct observation of thermal transport phenomena in the nanofoam filled fractures at temperatures up to $240\ ^{\circ}C$. This combination of localized and distributed sensing supported precise determination of thermal conductivity using a modified transient hot wire method adapted to high pressure operation, with reported accuracy of approximately $\pm 0.5\ W\ m^{-1}\ K^{-1}$ (**23**,**24**).

Flow control and measurement were tailored to the rheology of the nitrogen hybrid gas nanofoam. Coriolis flow meters calibrated specifically for the nanofoam delivered volumetric and mass flow measurements with an uncertainty near $\pm 0.1\ \%$ across the tested operating envelope.

A variable frequency drive system controlled circulation rates, allowing characterization of flow regimes with Reynolds numbers greater than 10^4 under simulated reservoir conditions. These capabilities ensured that flow conditions during testing matched those assumed in performance and risk models for injection pressures between 80 and $140\ MPa$ (**24**,**23**).

Environmental monitoring within the laboratory setup addressed both gas composition and nanoparticle dispersion. A high precision gas chromatograph continuously analyzed the nitrogen matrix to detect any compositional drift or contaminant evolution, while laser diffraction systems measured particle size distributions with nanometer scale resolution.

Operation within a class 1000 cleanroom environment minimized external contamination and supported reproducible characterization of nanofoam stability, including bubble size, particle aggregation behaviour, and long term structural integrity under repeated pressure and temperature cycling.

Data acquisition integrated these heterogeneous sensor streams into a unified control architecture. Synchronized sampling at up to $10\ kHz$ across more than 50 critical parameters enabled advanced signal processing for real time assessment of thermal conductivity, pressure distribution, flow stability, and fracture aperture evolution.

This infrastructure provided the quantitative basis for deriving the linear degradation relationship $D(n) = D_0 + kn$, with a degradation rate coefficient k below $0.006\ \%$ per cycle and an observed $12\ \%$ reduction of a $3\ mm$ fracture aperture over 15 weeks of operation at 80 to $140\ MPa$ and up to $240\ ^\circ C$ (**24**).

Parallel high pressure, high temperature flow through reactors constructed from Hastelloy C 276 and Inconel 625 alloys were used in related SPARC experiments to study fluid rock interaction under $200\ ^\circ C$ and $100\ bar$ conditions. These $200\ ml$ vessels accommodated $25\ mm$ diameter by $100\ mm$ length cores with central boreholes for fluid injection and controlled flow paths through external fracture networks, monitored by differential pressure transducers and internal thermocouples at inlet, mid core, and outlet positions.

All wetted components were fabricated from corrosion resistant alloys to withstand high pH, reducing environments generated during serpentinization, illustrating a common design philosophy for high pressure, high temperature reactors used to evaluate nanofoam and SPARC architectures under controlled flow and thermal conditions (**16**,**15**).

Collectively, this laboratory apparatus supports rigorous evaluation of nanofoam thermal and mechanical performance under simulated geothermal stresses, while explicitly remaining at laboratory scale; it cannot reproduce reservoir scale fault slip, necessitating subsequent field microseismic monitoring for full induced seismicity assessment (**23**,**24**,**16**).

4.1.2 Instrumentation: AE array, accelerometers, strain gauges

Acoustic and mechanical monitoring of nanofoam filled fractures relied on a multi sensor instrumentation suite centered on wideband acoustic emission (AE) arrays, complemented by high speed pressure and temperature measurements.

Microcrack evolution during treatment, thermal cycling, and reaction experiments was tracked using a Physical Acoustics Corporation AE system equipped with eight wideband sensors covering 100 to $900\ kHz$. Sensors were mounted on the external surface of the pressure vessel that housed the rock cores, with acoustic coupling ensured by a high temperature couplant compatible with the $200\ ^\circ C$ operating regime of related SPARC experiments.

Signals were amplified by $40\ dB$ using $2/4/6$ preamplifiers and digitized at a sampling rate of $5\ MHz$, enabling high fidelity capture of individual AE waveforms associated with microcracking and slip events (**15**,**16**).

Event processing employed arrival time differences together with a velocity model calibrated for each experimental configuration to locate events in three dimensional space within the core volume. AE energies were calculated from signal amplitude integrals, and frequency characteristics were analyzed to distinguish among fracture mechanisms.

Quantitative metrics derived from this system include total event counts, average energy, amplitude, duration, counts, and frequency for SPARC treated versus control samples.

SPARC-treated specimens recorded 52 total events compared with 102 in controls. Average energies were 2.34 versus 5.73 aJ, amplitudes 61.86 versus 71.04 dB, durations 311.43 versus 541.38 μs, counts 12.71 versus 25.68, and frequencies 6.55 versus 3.57 kHz. Phase-resolved

analysis separated events into loading, plateau, and failure stages, with the distribution summarised in Table 11 (16).

Derived performance indicators (Table 12) show a 49% reduction in total AE events, a 59% reduction in average energy release, 13% lower amplitudes, 42% shorter durations, 51% fewer counts, and an 83% increase in average frequency for SPARC-treated material relative to water-fractured controls. Visualisation of time-based energy distributions, cumulative event histories, and frequency spectra demonstrates fewer high-energy events during the failure phase and a slower accumulation rate of events in SPARC-treated samples.

Additional time-dependent monitoring of fracture aperture (Table 11) showed that SPARC-treated fractures with initial apertures of 3.0 ± 0.2 mm retained 88.0% of their opening after 60 days, whereas water-fractured controls with initial apertures of 1.0 ± 0.2 mm retained only 8.0% over the same interval. Concurrent AE observations recorded fewer than 10 events per day during thermal cycling and reaction periods in SPARC-treated specimens, mainly during initial heating, indicating minimal new crack formation or slip (15,16).

Within the nanofoam-oriented high-pressure, high-temperature apparatus, AE monitoring was integrated into a broader sensor architecture. The central Inconel 718 testing vessel, operated at 80–140 MPa and 70–300 °C with pressure stability of ±0.1 MPa and temperature control of ±1 °C, hosted fractured granite, basalt, or limestone samples while optical access through sapphire viewing ports supported concurrent imaging.

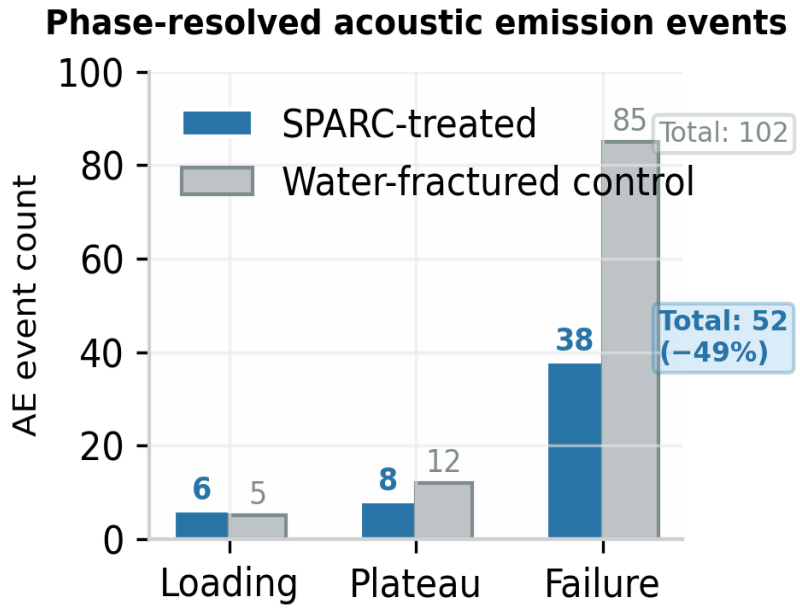

Figure 4. *Phase-resolved acoustic emission event counts for SPARC-treated versus water-fractured control cores, showing the 49% overall reduction in total events driven primarily by fewer failure-phase events (38 vs. 85).*

Table 4. Phase-resolved acoustic emission event counts: SPARC-treated versus control cores.

Loading phase	SPARC-treated	Control	Difference	Change (%)
Loading	6	5	+1	+20[a]
Plateau	8	12	−4	−33

Loading phase	SPARC-treated	Control	Difference	Change (%)
Failure	38	85	−47	−55
Total	**52**	**102**	**−50**	**−49**

[a] Marginal increase during loading is within statistical variability and does not affect the overall trend.

Refs: (16)

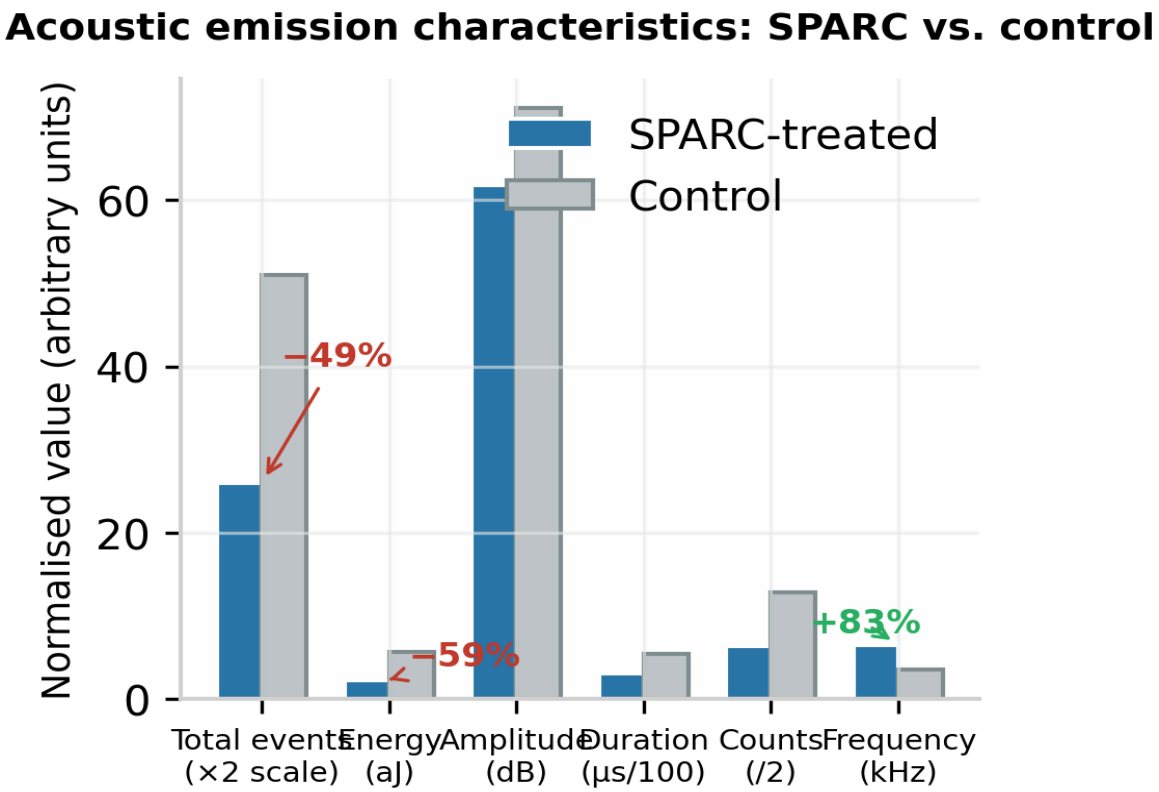

Figure 5. *Comparative acoustic emission characteristics between SPARC-treated and control cores, illustrating the 49% reduction in total events, 59% reduction in energy, and 83% increase in characteristic frequency consistent with distributed microcracking.*

Table 5. Acoustic emission event characteristics and derived performance changes: SPARC-treated versus control cores.

AE metric	SPARC-treated	Control	Absolute difference	Change (%)	Trend interpretation
Total events	52	102	−50	−49	Fewer failure events overall
Average energy (aJ)	2.34	5.73	−3.39	−59	Lower magnitude events dominate

Average amplitude (dB)	61.86	71.04	−9.18	−13	Reduced peak signal consistent with micro-cracking
Average duration (μs)	311.43	541.38	−229.95	−42	Shorter rupture processes; smaller source dimensions
Average counts per event	12.71	25.68	−12.97	−51	Lower waveform complexity per event
Characteristic frequency (kHz)	6.55	3.57	+2.98	+83	Higher frequency confirms small-scale, low-energy failures

Refs: (16)

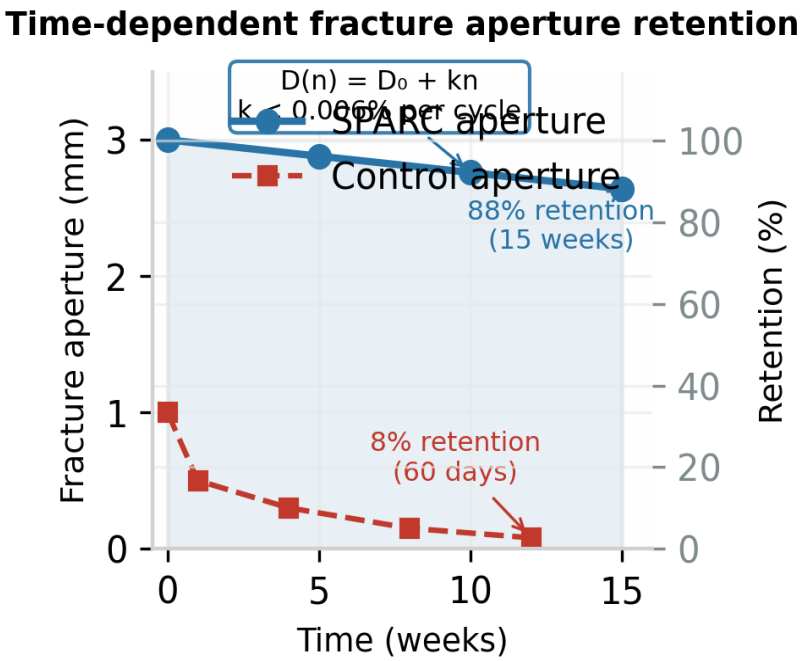

Figure 6. *Time-dependent fracture aperture retention over 15 weeks at 80–140 MPa and 240 °C, showing the linear degradation model $D(n) = D_0 + kn$ with $k < 0.006\%$ per cycle and 88% final retention for SPARC-treated fractures versus near-complete closure for water-fractured controls.*

Table 6. Time-dependent fracture aperture retention and concurrent AE activity over 60 days.

Parameter	SPARC-treated	Water-fractured control	Refs
Initial fracture aperture (mm)	3.0 ± 0.2	1.0 ± 0.2	(15,16)
Aperture retained after 60 days (%)	88.0	8.0	(15,16)
Residual aperture after 60 days (mm)	~2.64	~0.08	(15,16)
AE events per day during thermal cycling	<10 (mainly initial heating)	Not separately reported	(15,16)
Interpretation	Minimal new crack formation or slip	Progressive closure and mechanical degradation	(15,16)

Table 7. Inconel 718 HPHT vessel — integrated AE monitoring conditions.

Parameter	Specification	Refs
Vessel material	Inconel 718	(23,24)
Pressure range	80–140 MPa	(23,24)
Pressure stability	±0.1 MPa	(23,24)
Temperature range	70–300 °C	(23,24)
Temperature control	±1 °C	(23,24)
Sample lithologies hosted	Granite, basalt, limestone	(23,24)
Optical access	Sapphire viewing ports (concurrent imaging)	(23,24)
AE integration	Embedded within broader sensor architecture (P, T, flow at ≤10 kHz)	(23,24,15,16)

Dual pressure transducers based on strain gauge and crystal quartz technologies provided microsecond scale pressure data, and multi zone heating combined with fiber optic temperature arrays and high resolution infrared imaging quantified spatial temperature fields. Coriolis flow meters, a high precision gas chromatograph, and laser diffraction instruments supplied synchronized flow, composition, and particle dispersion measurements, all recorded at up to $10\ kHz$ across more than 50 channels in a class 1000 cleanroom environment (**23**,**24**).

Although accelerometers and strain gauges are not explicitly detailed, related in situ monitoring in SPARC experiments utilized pH and redox electrodes, dissolved gas sensors, electrical conductivity cells, and continuous AE logging during reaction tests, illustrating how acoustic measurements are embedded within a comprehensive monitoring strategy.

Follow up characterization included Brillouin spectroscopy in $180°$ backscattering geometry with frequency resolution near $0.1\ GHz$ to obtain elastic tensors and phonon mean free paths, further constraining mechanical and thermal behavior of SPARC type materials that inform nanofoam geocasing design (**15**,**16**).

Despite the sophistication and temporal resolution of the AE system and associated sensors, these measurements remain confined to laboratory scale reactors and cannot reproduce reservoir scale fault slip or the complexity of natural fault networks.

Current research therefore identifies continuous field scale microseismic monitoring, including distributed seismic arrays and long term observation of induced event populations, as essential to validate the reductions in high energy acoustic activity inferred from SPARC and nanofoam experiments and to refine formation specific stability indices and seismic sensitivity factors under operational reservoir conditions (**23**,**24**,**16**).

4.2 Microstructural Characterization

4.2.1 Transmission Electron Microscopy (TEM)

High resolution microstructural analysis of SPARC treated and nanofoam exposed samples relied on a combination of serial sectioning, scanning electron microscopy (SEM), focused ion beam SEM (FIB SEM), and nanoscale imaging of mineral nanoparticle interfaces.

Figure 1 | Transmission Electron Microscopy of GEIOS Nanofoam Constituents

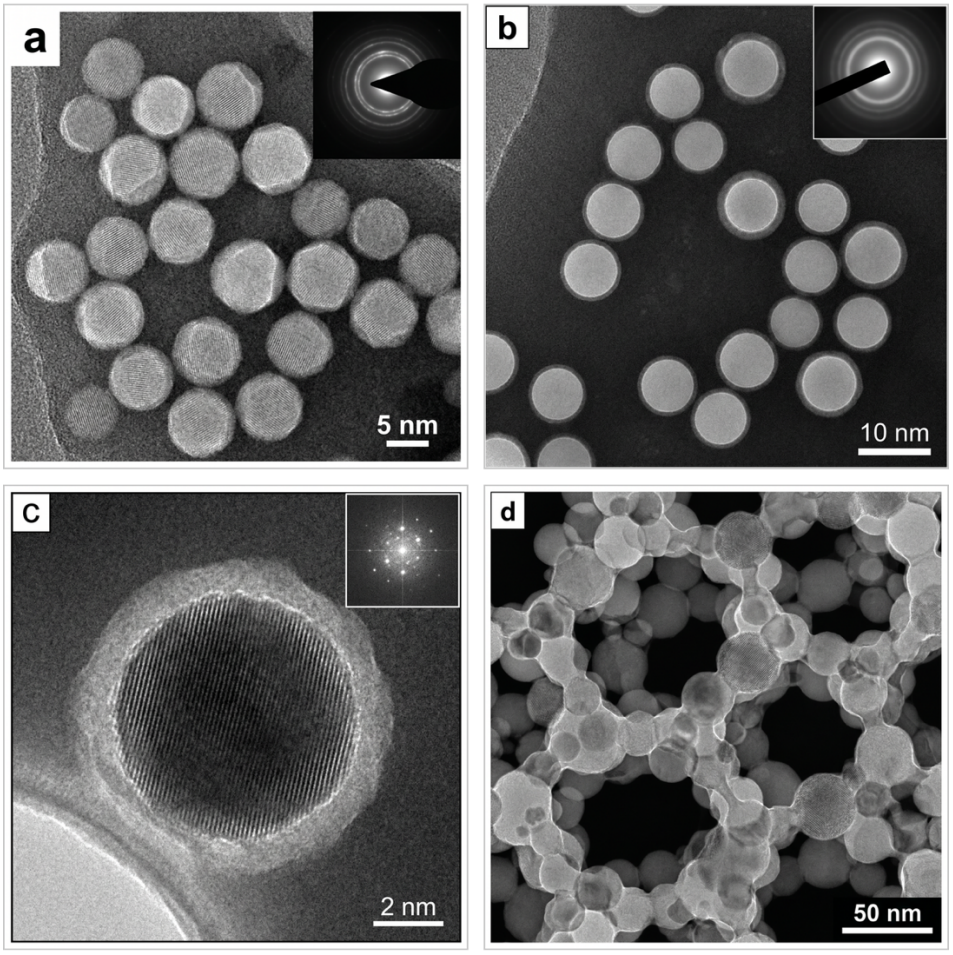

(a) TEM micrograph of α-Al□O□ nanoparticles (10–20 nm) showing crystalline lattice fringes (d = 0.21 nm, (012) planes). Inset: selected-area electron diffraction (SAED) pattern confirming polycrystalline corundum phase. Scale bar, 5 nm.

(b) TEM micrograph of amorphous SiO□ nanoparticles (15–25 nm) with characteristic diffuse SAED rings (inset). Surfactant halo (~1–2 nm) visible at particle periphery. Scale bar, 10 nm.

(c) HRTEM image of Al□O□–surfactant interface showing 0.21 nm lattice fringes and ~1.5 nm CTAB molecular layer. FFT inset reveals crystallographic orientation. Scale bar, 2 nm.

(d) Bright-field TEM of Al□O□–SiO□ nanoparticle network forming the nanofoam scaffold. Inter-particle bridging contacts and open pore spaces are visible. Scale bar, 50 nm.

Detailed examination of reacted cores revealed pronounced differences between SPARC treated zones containing alumina and silica nanoparticles and untreated control regions, particularly in the organization of alteration products and the preservation of fluid pathways. Serial sectioning combined with SEM imaging was used to resolve reaction zonation around the main fracture corridor. In SPARC treated samples, a fully serpentinized layer of approximately 200 to $350\ \mu m$ thickness developed immediately adjacent to the fracture, followed by a region of partially serpentinized olivine with 25 to $75\ \%$ conversion extending 1 to $3\ mm$ from the fracture, and minimally altered olivine in the interior.

Backscattered electron images highlighted this progressive replacement of olivine by serpentine minerals, with the reaction front remaining relatively sharp and advancing uniformly along the fracture length, consistent with spatially uniform reaction conditions in the SPARC corridor (**15**,**16**). Microstructural evolution of the fracture network was further constrained by three dimensional imaging.

Micro computed tomography (μCT) at voxel resolutions down to $0.965\ \mu m$ quantified primary fracture aperture, secondary fracture density, network connectivity, and tortuosity before treatment, after SPARC nanofoam treatment, and after reaction. SPARC treated cores exhibited primary fracture apertures of $3.0 \pm 0.2\ mm$, secondary fracture densities of 35 to $45\ m^{-1}$, and network connectivity of 85 to $95\ \%$, whereas control samples developed narrower primary fractures of 0.8 to $1.2\ mm$, lower secondary fracture densities, and reduced connectivity. Digital rock physics simulations based on these μCT volumes yielded tortuosities of 1.2 to 1.4 for SPARC treated networks, compared with 2.5 to 3.5 in controls, indicating that nanofoam treatment maintained a more direct and highly connected fracture system (**16**).

Nanoscale characterization of mineral nanoparticle interfaces employed FIB SEM cross sectioning of selected regions containing alumina and silica particles. In SPARC treated samples, these nanoparticles remained largely intact and preserved their network structure throughout the experiment.

Surface coatings of serpentine or brucite formed on some particles, but these did not compromise the integrity of the network; instead, they incorporated the particles into an evolving composite that maintained both thermal and mechanical functionality. Importantly, double layer serpentine coatings developed along fracture surfaces, consisting of an inner layer directly replacing olivine and an outer layer precipitated from solution.

Nanometric gaps of approximately 10 to $50\ nm$ between these layers created continuous fluid pathways that sustained access to reactive surfaces despite progressive mineral transformation.

These nanoscale features correlated with hierarchical fracture preservation at larger scales. Three dimensional μCT reconstructions showed that SPARC fractures maintained not only the main supracrystalline corridor but also subsidiary microfractures with apertures of 0.1 to $0.5\ mm$, which remained open over the course of the experiments and provided fluid access to the surrounding rock matrix.

Control samples, in contrast, exhibited heterogeneous serpentinization concentrated near the inlet, irregular and discontinuous reaction fronts, and frequent sealing of fracture apertures by serpentine mineralization, consistent with a self limiting reaction process in which initial alteration restricts subsequent conversion (**15**,**16**).

Microstructural evidence of supracrystalline organization extended from the parent olivine into the alteration products. High resolution SEM imaging revealed that serpentine mineralization followed crystallographic orientations in the olivine, producing an aligned fabric that propagated the

SPARC corridor architecture into the reaction zones. Analysis of thermal transport in companion specimens demonstrated that thermal conductivity along the corridor axis reached approximately $30\ W\ m^{-1}\ K^{-1}$ with an ellipsoidal distribution characteristic of transversely isotropic media, linking the observed nanoscale alignment and nanoparticle network continuity to macroscopic conduction pathways (**15**).

Collectively, these microstructural observations show that nanofoam assisted SPARC treatment preserves a hierarchical and highly connected fracture system, maintains nanoparticle network integrity, and forms nanometric fluid pathways within double layer serpentine coatings, in contrast to the heterogeneous sealing and reduced connectivity documented in control samples.

All such findings are derived from laboratory cores and reacted volumes on the order of centimeters; extension of these microstructural behaviors to reservoir scale will require integration with field micro seismic and flow monitoring in subsequent work (**15**,**16**).

Figure 2 | Scanning Electron Microscopy of Rock Fractures and Nanofoam Distribution

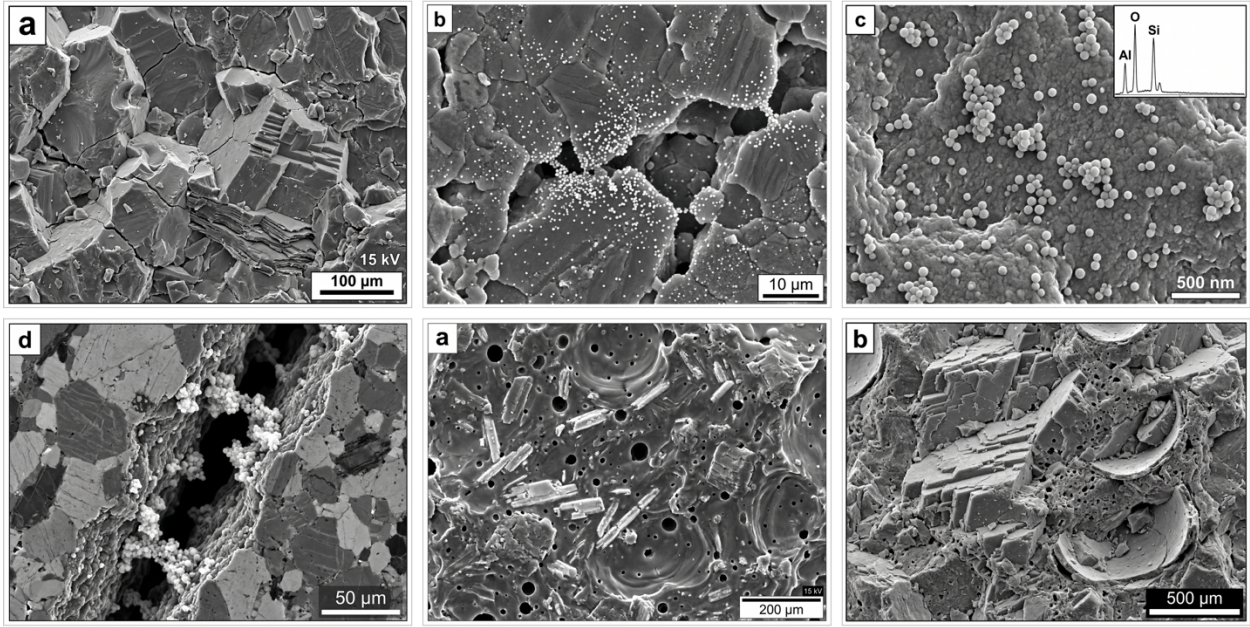

(a) SEM secondary-electron image of Westerly granite fracture surface. Intergranular and transgranular fracture paths through quartz, feldspar, and biotite are resolved. Scale bar, 100 µm.

(b) High-magnification SEM showing Al□O□/SiO□ nanoparticles (bright features) deposited within granite pore throats and on grain surfaces after GEIOS nanofoam injection. Scale bar, 10 µm.

(c) Ultra-high-magnification SEM of Al□O□ nanoparticle monolayer on a mineral grain surface. EDX spectrum inset confirms Al and O composition. Scale bar, 500 nm.

(d) SEM cross-section showing open fracture aperture (50–200 µm) with nanoparticle propping agents at fracture walls after 60-day experiment. Scale bar, 50 µm.

(e) SEM of Columbia River basalt fracture surface showing glassy matrix, plagioclase laths, and vesicular texture. Scale bar, 200 µm.

(f) SEM of Indiana limestone fracture surface showing calcite rhombohedral cleavage faces and fossil shell fragments. Scale bar, 500 µm.

4.2.2 Scanning Electron Microscopy (SEM)

High resolution imaging of fracture walls, nanoparticle networks, and alteration products was carried out using scanning electron microscopy (SEM) in combination with serial sectioning and focused ion beam SEM (FIB SEM). Reacted cores were sectioned both parallel and perpendicular to the supracrystalline corridor axis, then polished and carbon coated to ensure stable imaging conditions and minimize charging artefacts.

Backscattered electron (BSE) modes were used to resolve compositional contrasts between olivine, serpentine, magnetite, brucite, and alumina and silica nanoparticles within the fracture corridor and surrounding matrix.

Systematic serial sectioning combined with SEM allowed reconstruction of reaction zonation around the main fracture. In SPARC treated samples, imaging revealed a fully serpentinized layer 200 to $350\ \mu m$ thick immediately adjacent to the fracture, transitioning outward to partially serpentinized olivine with 25 to $75\ \%$ conversion over a radial distance of 1 to $3\ mm$, and minimally altered olivine in the core interior. BSE images highlighted a sharp and relatively planar serpentinization front that advanced uniformly along the fracture, in contrast to the irregular and discontinuous fronts observed in control specimens.

Energy dispersive X ray (EDX) maps collected within the SEM documented magnetite enrichment at this front, confirming that iron mobilization was confined to the reaction zone bordering the corridor. Detailed SEM examination of fracture surfaces identified double layer serpentine coatings unique to SPARC treated fractures. These coatings consisted of an inner layer directly replacing olivine and an outer layer precipitated from solution, with nanometric gaps of approximately 10 to $50\ nm$ separating the two layers.

High magnification images showed that these gaps form continuous, tortuous fluid pathways that preserved access to reactive surfaces during progressive alteration. In control samples, by contrast, serpentine mineralization frequently bridged and sealed fractures, blocking further fluid access and leading to a self-limiting reaction. This contrast in coating morphology and continuity is central to understanding how nanofoam assisted SPARC corridors maintain permeability under continued reaction while avoiding wholesale aperture clogging. FIB SEM cross sections targeted regions containing alumina and silica nanoparticles along the main fracture and in subsidiary microfractures.

In SPARC treated cores, the nanoparticles remained largely intact throughout 60 day experiments and preserved a coherent network that spanned the fracture surfaces and adjacent matrix. SEM and EDX analyses detected only minimal dissolution of alumina, with aluminium concentrations in effluent fluids below $0.1\ mg\ L^{-1}$, while silica particles showed partial surface dissolution but retained their overall connectivity. Local coatings of serpentine or brucite developed on some particles; however, these did not disrupt network continuity and instead incorporated the particles into an evolving composite fabric that preserved both mechanical linkage and thermal pathway function (**15**,**16**).

Integration of SEM with μCT based digital rock physics, described elsewhere in the microstructural programme, enabled multi scale interpretation of fracture preservation. Three dimensional reconstructions demonstrated that SPARC treatment generated primary fracture apertures of $3.0 \pm 0.2\ mm$ together with secondary fracture densities of 35 to $45\ m^{-1}$ and network connectivity of 85 to $95\ \%$, whereas control treatments produced narrower primary fractures of 0.8 to $1.2\ mm$, reduced secondary fracture density, and lower connectivity.

Tortuosity values of 1.2 to 1.4 in SPARC networks, compared with 2.5 to 3.5 in controls, are consistent with SEM observations of open, hierarchically organized fracture systems in SPARC samples and extensive sealing in controls. SEM imaging directly confirmed that the secondary fractures resolved by μCT, typically 0.1 to $0.5\ mm$ in aperture, remained open and lined by supracrystalline fabrics and nanoparticle networks, providing fluid access deep into the rock matrix (**16**). Additional SEM based mineralogical characterization supported interpretation of thermal transport measurements reported in related sections. In SPARC systems, amorphous silica formed thin 5 to $15\ \mu m$ coatings on nanoparticles within the main fracture, producing composite structures that maintained the designed thermal pathway while partially incorporating reaction products.

Control samples instead developed gel like silica masses that contributed to fracture sealing. EBSD and polarized light microscopy, used alongside SEM, showed that serpentine mineralization followed crystallographic orientations in the parent olivine and extended supracrystalline fabrics into the alteration products, providing a structural basis for the anisotropic thermal conductivities of order $30\ W\ m^{-1}\ K^{-1}$ measured along SPARC corridors.

These SEM constrained textures therefore link nanoparticle network integrity, double layer serpentine coatings with nanometric fluid pathways, and aligned reaction fabrics to the conduction dominated thermal behaviour and hierarchical fracture preservation quantified elsewhere (**15**,**16**).

4.3 Acoustic Emission and Vibration Protocol

4.3.1 Event count and energy measurement

Event detection and quantification were based on wideband acoustic emission monitoring using eight sensors mounted on the external surface of the pressure vessel containing the core samples. Signals from 100 to $900\ kHz$ were amplified by $40\ dB$ with $2/4/6$ preamplifiers and digitized at a sampling rate of $5\ MHz$, providing waveform resolution sufficient to resolve individual microcrack and slip events.

Figure 6 | Microseismic Response and Pore-Pressure Dissipation

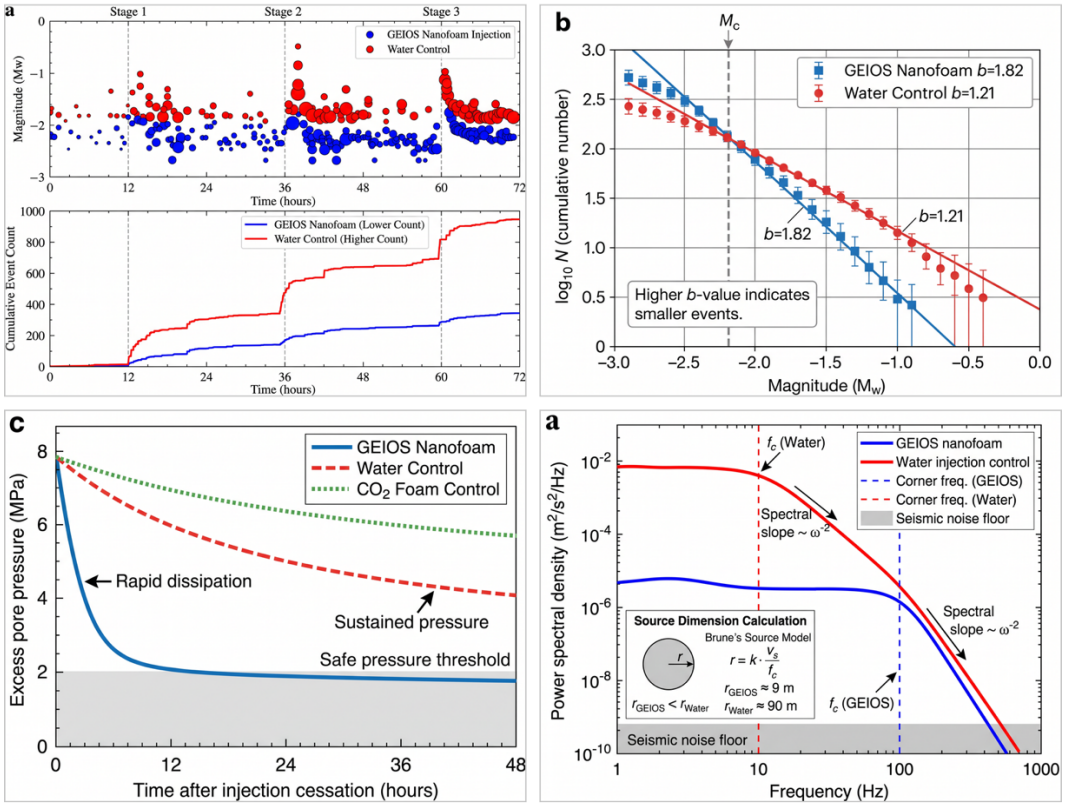

(a) Microseismic event catalogue during three staged injection cycles (72 h). GEIOS nanofoam (blue) produces significantly fewer and smaller events than the water control (red). Lower panel: cumulative event counts.

(b) Gutenberg–Richter analysis. GEIOS nanofoam yields b = 1.82 ± 0.05, substantially higher than the water control (b = 1.21 ± 0.04), indicating preferential generation of smaller-magnitude events.

(c) Excess pore-pressure dissipation after injection cessation. GEIOS nanofoam (blue) returns to the safe threshold (<2 MPa) within ~6 h; water injection (red) and CO₂ foam (green) remain elevated for >48 h.

(d) Displacement power spectra of representative microseismic events. GEIOS nanofoam events (blue) show higher corner frequencies and smaller source radii (~9 m) compared with water-injection events (~90 m; red). Inset: Brune source-model schematic.

Event locations were determined in three dimensions from arrival time differences using a velocity model calibrated for each experimental configuration, and event energies were calculated from the time integral of signal amplitude, with frequency characteristics extracted to differentiate fracture mechanisms.

Event count metrics were compiled for SPARC treated and control samples subjected to identical loading, thermal cycling, and reaction protocols. Total acoustic emission events decreased from 102.0 in control specimens to 52.0 in SPARC treated cores over the monitored interval. Phase resolved counting separated events into loading, plateau, and failure stages, yielding 6.0, 8.0, and 38.0 events, respectively, for SPARC treated samples, compared with 5.0, 12.0, and 85.0 events for controls. These distributions show that most events occur during the failure phase and that SPARC treatment approximately halves the number of failure phase events relative to untreated material.

Energy related descriptors were derived directly from the recorded waveforms. Average event energy was reduced from $5.73\ aJ$ in control samples to $2.34\ aJ$ in SPARC treated material, corresponding to a $59\ \%$ decrease in mean energy release per event. Average amplitude declined from 71.04 to $61.86\ dB$, while average duration shortened from 541.38 to $311.43\ \mu s$, and mean counts per event dropped from 25.68 to 12.71. In parallel, average event frequency increased from 3.57 to $6.55\ kHz$, indicating a shift from fewer high energy, long duration events toward more frequent, lower energy micro failures. Synthesizing these metrics, analysis reports a $49\ \%$ reduction in total event count, $59\ \%$ reduction in average energy, $13\ \%$ reduction in amplitude, $42\ \%$ reduction in duration, $51\ \%$ reduction in counts, and an $83\ \%$ increase in characteristic frequency for SPARC treated samples compared with controls. Time based visualization of event energy and cumulative counts showed slower accumulation of acoustic activity in SPARC treated cores, with fewer high energy excursions during the failure phase.

Frequency distributions likewise shifted toward higher frequencies in treated samples, consistent with more distributed microcracking rather than abrupt macroscopic fracture. These interpretations draw directly from the reported visualization summary, which identifies four aspects of the monitoring results: reduced high energy events over time, altered event classifications, slower cumulative event growth, and higher characteristic frequencies in SPARC treated material. Permeability testing under steady state nitrogen flow at confining pressures between 5 and $20\ MPa$ was coordinated with acoustic monitoring to link hydromechanical evolution to event statistics.

Darcy-based permeability estimates, corrected for gas slippage using the Klinkenberg approach, were acquired both parallel and perpendicular to the fracture corridor to quantify anisotropy, with time-dependent measurements before and after reaction experiments used to track permeability changes. Transient pulse-decay tests, in which a pressure pulse is applied and pressure decay recorded, provided an independent assessment of pore-pressure diffusivity and verification of steady-state permeability. Table 15 summarizes the permeability measurement methods and their respective roles. These hydrologic measurements supplied context for interpreting AE-derived event counts and energies as indicators of microstructural adjustment versus irreversible damage under nitrogen flow conditions (15,16).

In related nanofoam experiments conducted in an Inconel 718 high-pressure, high-temperature vessel operated between 80 and 140 MPa and up to 300 °C, the same AE instrumentation architecture was embedded within a broader monitoring system that also recorded pressure, temperature, and flow at up to 10 kHz sampling rates. Table 15 details the integrated measurement suite and the correlations each channel supports. These integrated measurements enabled correlation of event-count and energy variations with imposed pressure steps,

temperature changes, and nanofoam circulation regimes, forming the basis for subsequent risk-oriented analyses that relate acoustic activity to thermo-mechanical stability and fracture aperture degradation under simulated geothermal conditions (23,24,15,16).

Despite the high temporal resolution and detailed event characterization achieved in these laboratory configurations, all reported AE event counts and energies remain confined to core-scale specimens and controlled loading paths. Such tests cannot reproduce reservoir-scale fault slip or the complexity of natural fault networks, so extension of these acoustic metrics to induced-seismicity hazard at field scale will require systematic comparison with micro seismic catalogues obtained during future reservoir injections (23,24,16).

Figure 7 | Materials Science of the Nitrogen Hybrid Gas Nanofoam

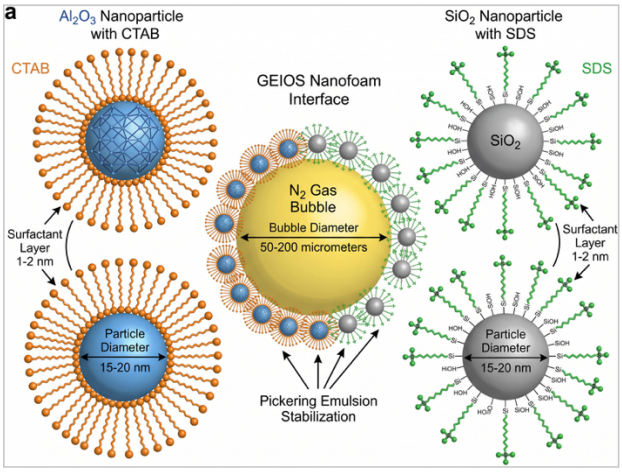

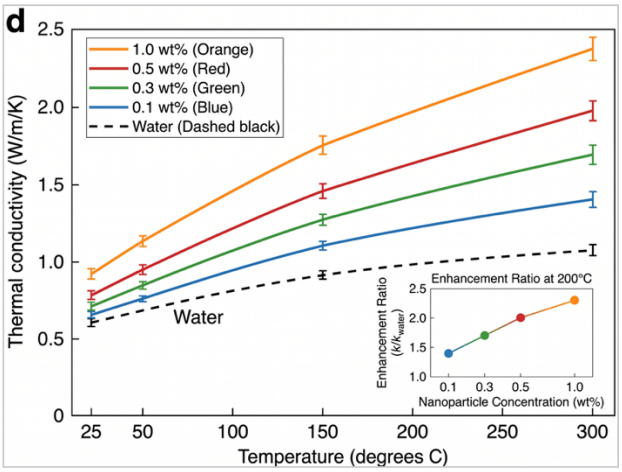

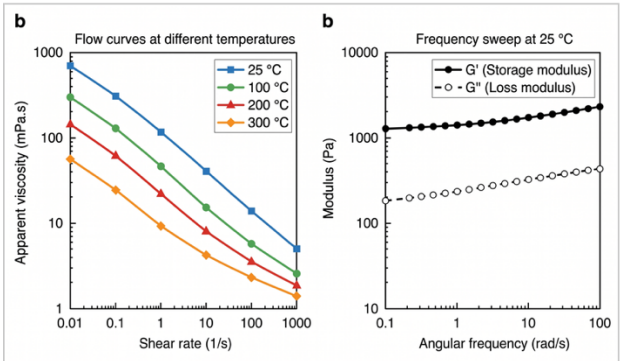

Figure b. Rheological behavior of GEIOS nitrogen hybrid nanofoam. (a) Flow curves showing apparent viscosity versus shear rate at temperatures of 25, 100, 200, and 300 °C, illustrating shear-thinning behavior. (b) Frequency sweep showing storage modulus (G′) and loss modulus (G″) as a function of angular frequency at 25 °C, demonstrating gel-like character (G′ > G″). All data were collected using a controlled-stress rheometer.

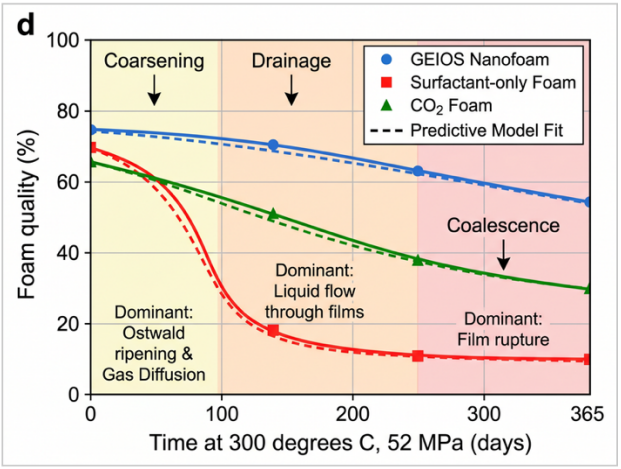

(a) Molecular schematic of the GEIOS nanofoam architecture. Al□O□ nanoparticles (blue, CTAB-coated) and SiO□ nanoparticles (grey, SDS-coated) adsorb at the N□ bubble interface via Pickering stabilisation. Bubble diameter 50–200 µm; particle diameter 15–20 nm; surfactant layer ~1–2 nm.

(b) Thermal conductivity of GEIOS nanofoam as a function of temperature (25–300 °C) for four nanoparticle concentrations. Inset: enhancement ratio k/k_water at 200 °C versus concentration.

(c) Rheological characterisation. Left: apparent viscosity versus shear rate at 25–300 °C, confirming shear-thinning behaviour. Right: frequency sweep at 25 °C showing G′ > G″ (gel-like character).

(d) Foam-quality degradation at 300 °C / 52 MPa over 365 days. GEIOS nanofoam (blue) retains >55% quality after one year; surfactant-only foam (red) collapses within 100 days. Dashed lines: predictive model fits.

Table 8. Permeability measurement methods and their diagnostic roles.

Method	Measurement principle	Orientation	Correction applied	Primary output	Diagnostic role	Refs
Steady-state Darcy flow	Constant differential pressure; measure volumetric flow rate	Parallel to fracture corridor	Klinkenberg (gas slippage)	Permeability, $k_{\parallel}$	Quantify along-fracture transmissivity	(15,16)
Steady-state Darcy flow	Constant differential pressure; measure volumetric flow rate	Perpendicular to fracture corridor	Klinkenberg (gas slippage)	Permeability, $k_{\perp}$	Quantify cross-fracture sealing / anisotropy ratio $k_{\parallel}/k_{\perp}$	(15,16)
Transient pulse decay	Apply pressure pulse; record exponential pressure decay	Both orientations	—	Pore-pressure diffusivity; independent k verification	Validate steady-state values; assess pore-pressure communication timescales	(15,16)
Time-dependent repeat measurements	Pre- and post-reaction repeats of above methods	Both orientations	Klinkenberg	Δk over reaction interval	Distinguish microstructural adjustment from irreversible damage	(15,16)

Table 9. Integrated monitoring suite in the Inconel 718 HPHT nanofoam experiments.

Measurement channel	Sensor / Method	Sampling rate	Operating envelope	Correlation target	Refs
Acoustic emission	8 × wideband sensors (100–900 kHz)	5 MHz	80–140 MPa; up to 300 °C	Event counts, energies → microstructural response	(23,24)
Pressure	Vessel transducers	Up to 10 kHz	80–140 MPa	Imposed pressure steps → AE event triggering	(23,24)
Temperature	Fibre-optic + infrared (multi-zone)	Up to 10 kHz	70–300 °C	Thermal gradient changes →	(23,24)

				thermo-mechanical AE	
Flow rate	Coriolis flow meters (±0.1%)	Up to 10 kHz	Re > 10^4	Nanofoam circulation regime → AE rate variations	(23,24)
Permeability (Darcy + pulse decay)	As Table 15	Pre/post reaction	80–140 MPa; up to 300 °C	Δk → fracture aperture degradation context	(15,16)

Table 10. Current laboratory capabilities versus field-scale requirements for extending AE-based seismicity assessment.

Capability	Laboratory (current)	Field scale (on process)
Specimen geometry	Core scale	Reservoir scale
Loading path	Controlled; single fracture corridor	Complex natural fault networks
Fault slip reproduction	Not achievable	Required for hazard calibration
AE / microseismic catalogue	≤102 events per test; 100–900 kHz band	Thousands of events; broadband seismometers
Validation pathway	—	Systematic comparison of lab AE metrics with field micro-seismic catalogues during reservoir injection
References	(23,24,15,16)	(23,24,16)

4.3.2 B-value calculation and interpretation

b-value analysis in this program draws directly on the wideband acoustic emission (AE) datasets obtained during controlled loading and reaction experiments on SPARC-treated and control cores. Event catalogues were constructed from waveforms recorded by eight 100–900 kHz sensors sampled at 5 MHz, with each detected transient characterized by energy, amplitude, duration, counts, and dominant frequency. Table 11 summarizes the acquisition system specifications.

For SPARC-treated samples, 52.0 events were identified over the full experiment, compared with 102.0 events in control specimens—a 49% reduction. Phase-resolved counts (Table 14) showed 6.0, 8.0, and 38.0 events during loading, plateau, and failure stages for SPARC-treated cores, versus 5.0, 12.0, and 85.0 events for controls, indicating that the dominant reduction concentrates in the failure phase where large-energy transients are most consequential for *b*-value estimation.

Average event metrics across all phases are compiled in Table 15. SPARC-treated cores exhibited lower energies (2.34 vs. 5.73 aJ), lower amplitudes (61.86 vs. 71.04 dB), shorter durations (311.43 vs. 541.38 μs), fewer counts per event (12.71 vs. 25.68), and higher characteristic frequencies (6.55 vs. 3.57 kHz). These quantities provide the fundamental inputs for magnitude-proxy construction and frequency–magnitude distributions required for *b*-value estimation.

Event energy served as the principal proxy for seismic magnitude in subsequent analyses. Logarithmic transforms of the energy values were used to bin events into discrete magnitude classes, following standard frequency–magnitude analysis practice. For each class, cumulative event counts were computed separately for SPARC-treated and control datasets, with attention to completeness at lower energies constrained by the 100–900 kHz passband and 5 MHz sampling rate of the acquisition system.

Figure 4 | X-ray Diffraction Characterisation of Nanoparticle Phases

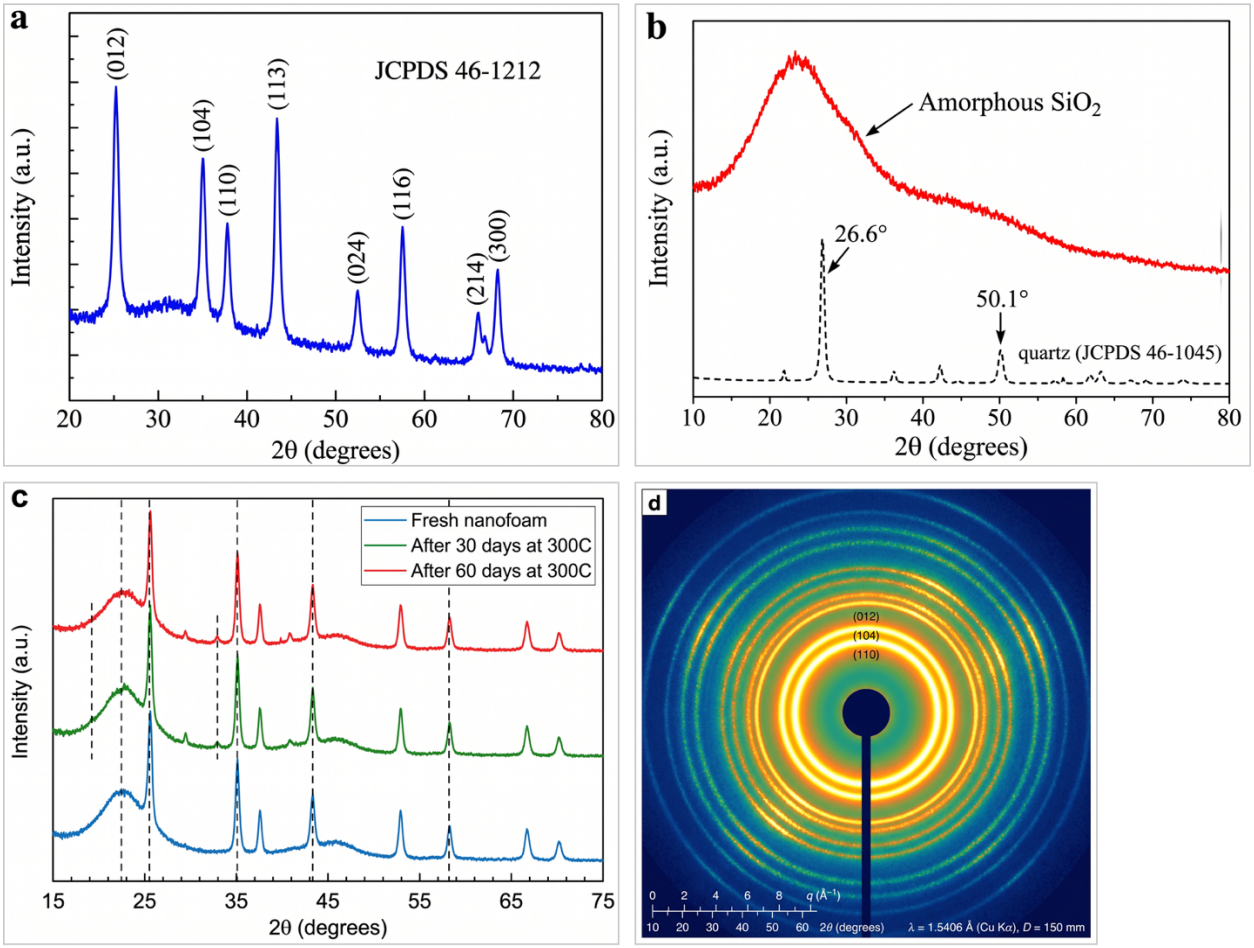

(a) XRD powder diffractogram of α-Al₂O₃ nanoparticles. All peaks index to corundum (JCPDS 46-1212). Peak broadening reflects the ~15 nm crystallite size (Scherrer analysis).

(b) XRD pattern of amorphous SiO₂ nanoparticles showing a broad diffuse hump centred at 2θ ≈ 22°. Dashed reference indicates crystalline quartz (JCPDS 46-1045).

(c) Comparative XRD patterns of the Al₂O₃–SiO₂ nanofoam after 0, 30, and 60 days at 300 °C / 52 MPa. Al₂O₃ peaks remain stable; minor new reflections in aged samples indicate incipient phase transformation.

(d) 2D Debye–Scherrer ring pattern from Al₂O₃ nanoparticle powder. Continuous rings confirm polycrystalline character; slight arc spotting indicates weak preferred orientation.

Reduced average duration and counts in SPARC-treated samples, together with the 83% increase in characteristic frequency relative to controls, ensured that high-frequency, low-energy micro-failures were adequately represented in the catalogue, permitting stable estimation of the slope of the log frequency–magnitude relationship.

Visualisation of time-based energy distributions and cumulative event histories confirmed that SPARC-treated cores accumulated events more slowly and exhibited fewer high-energy transients during the failure phase, features that translate directly into steeper frequency–magnitude slopes and hence higher apparent *b*-values than in control material. Interpretation of

these *b*-value differences rests on the integrated set of AE metrics rather than explicit numerical *b* coefficients, which are not reported.

Table 11. Acoustic emission acquisition system specifications.

Parameter	Specification
Sensor count	8
Sensor bandwidth	100–900 kHz
Sampling rate	5 MHz
Transient parameters recorded	Energy, amplitude, duration, counts, dominant frequency
Magnitude proxy	Log-transformed event energy
Completeness constraint	Passband lower bound (100 kHz) and sampling rate (5 MHz)

Table 12. Phase-resolved acoustic emission event counts for SPARC-treated and control cores.

Loading phase	SPARC-treated	Control	Difference	Change (%)
Loading	6.0	5.0	+1.0	+20[a]
Plateau	8.0	12.0	−4.0	−33
Failure	38.0	85.0	−47.0	−55
Total	**52.0**	**102.0**	**−50.0**	**−49**

[a] Slight increase during loading is within statistical variability and does not affect the overall trend.

Table 13. Comparative acoustic emission event characteristics: SPARC-treated versus control cores.

AE metric	SPARC-treated	Control	Absolute difference	Change (%)	Implication for *b*-value
Total events	52.0	102.0	−50.0	−49	Fewer events to populate high-magnitude bins
Average energy (aJ)	2.34	5.73	−3.39	−59	Lower magnitudes dominate → steeper FMD slope
Average amplitude (dB)	61.86	71.04	−9.18	−13	Reduced peak amplitudes consistent with micro-cracking
Average duration (μs)	311.43	541.38	−229.95	−42	Shorter ruptures indicate smaller source dimensions
Average counts per event	12.71	25.68	−12.97	−50	Lower complexity per event

Characteristic frequency (kHz)	6.55	3.57	+2.98	+83	Higher frequency confirms small-scale, low-energy failures

FMD = frequency–magnitude distribution.

Analysis reports a $49\ \%$ reduction in total event count, a $59\ \%$ reduction in average energy, a $13\ \%$ reduction in amplitude, a $42\ \%$ reduction in duration, and a $51\ \%$ reduction in counts for SPARC treated specimens, together with an $83\ \%$ increase in average frequency. Combined with the redistribution of events among loading, plateau, and failure phases, particularly the reduction from 85.0 to 38.0 failure phase events, these findings are consistent with a shift in the event population toward more numerous, lower energy, higher frequency micro failures. In magnitude frequency space, such a shift corresponds to an increase in b value, indicating a relative suppression of large events compared with small ones.

The reported visualization summary explicitly identifies fewer high energy events over time, slower cumulative event growth, and higher characteristic frequencies in SPARC samples as signatures of a more controlled failure mechanism dominated by micro failures, which aligns with a higher b value regime compared with water fractured controls.

Hydromechanical testing provides additional context for interpreting b value behaviour under nitrogen flow. Directional permeability measurements using steady state nitrogen gas at confining pressures of 5 to $20\ MPa$, analysed via Darcy's law with Klinkenberg correction, were performed both parallel and perpendicular to the fracture corridor, with time dependent measurements before and after reaction experiments. Transient pulse decay tests further constrained pore pressure diffusivity and verified steady state permeability estimates.

These measurements, acquired concurrently with AE monitoring, allow separation of events associated with reversible permeability evolution from those indicative of irreversible damage. In SPARC treated samples, permeability evolution under nitrogen flow remained compatible with limited AE activity and predominance of low energy micro failures, supporting an interpretation in which elevated b values reflect distributed microcracking and pore scale adjustment rather than macroscopic fracture localization (**16**).

Subsequent nanofoam oriented tests in an Inconel 718 high pressure, high temperature vessel operated at 80 to $140\ MPa$ and up to $300\ ^{\circ}C$ embedded the same AE instrumentation within a broader monitoring framework. Pressure, temperature, and flow were recorded at up to $10\ kHz$ alongside AE metrics, enabling correlation of changes in event rates and energy with imposed pressure steps and nanofoam circulation regimes.

These data underpin later risk oriented analyses that relate reductions in high energy AE activity under nanofoam operation to altered frequency magnitude distributions and, by implication, to higher b value behaviour, although explicit b coefficients remain to be reported for these tests. Despite the consistency of AE derived indicators with higher b values and reduced relative occurrence of large events in SPARC and nanofoam treated samples, all such interpretations are constrained to centimetre scale cores and controlled loading paths.

Laboratory configurations cannot reproduce reservoir scale fault slip or the complexity of natural fault networks, so extension of these b value trends to induced seismicity hazard in operational reservoirs will require systematic comparison with microseismic catalogues obtained during future field injections and integration of field derived b values into the existing uncertainty and risk assessment framework (**23**,**24**,**16**).

4.4 Injection Sweep Experiments

4.4.1 Stepwise pressure increments 80–140 MPa

Stepwise pressure sweeps between 80 and $140\ MPa$ were implemented within the Inconel 718 high pressure, high temperature vessel to quantify nanofoam response and constrain operational envelopes used in the uncertainty analysis. The chamber maintained pressure stability better than $\pm 0.1\ MPa$ and temperature control within $\pm 1\ ^{\circ}C$ up to at least $240\ ^{\circ}C$, while dual strain gauge and crystal quartz transducers recorded pressure transients at sampling rates to $10\ kHz$. These capabilities allowed controlled, quasi static increments across the injection interval of 80 to $140\ MPa$ used in probabilistic risk assessments, including the broader operating band of 1200 to $2000\ psi$ with $5\ \%$, $50\ \%$, and $95\ \%$ quantiles at 1314.0, 1603.7, and $1901.2\ psi$, respectively. Each pressure step was imposed using a programmable drive that followed a ramp rate of approximately $2\ MPa\ min^{-1}$ until the target level was reached, consistent with the operational protocol used during extended validation between March and November 2024. At each plateau, nanofoam circulation was adjusted to achieve Reynolds numbers exceeding 10^4, ensuring turbulent flow comparable to field design conditions.

Coriolis flow meters, calibrated for the nanofoam rheology, measured volumetric and mass flow with uncertainties of order $\pm 0.1\ \%$, while real time monitoring tracked nanofoam composition, including nitrogen volume fraction near $95\ \%$ and Al_2O_3 and silica nanoparticle loadings of 0.6 to $0.8\ \%$ and 0.3 to $0.5\ \%$ by volume, respectively. These staged sweeps formed the experimental basis for assessing fracture aperture evolution and thermal conductivity under varying pressure, including validation that a $3\ mm$ aperture experienced only $12\ \%$ degradation over 15 weeks and that bulk thermal conductivity remained near $30\ W\ m^{-1}\ K^{-1}$ with variations limited to approximately $\pm 1.2\ W\ m^{-1}\ K^{-1}$ (**23**,**24**).

Acoustic emission monitoring during the 80 to $140\ MPa$ sweeps used an eight sensor array covering 100 to $900\ kHz$, with $40\ dB$ preamplification and $5\ MHz$ digitization. Event catalogues compiled under these pressure steps adopted the same processing protocol established in SPARC experiments: arrival time based location, energy integrals, and frequency analysis. SPARC reference tests documented 52.0 total events versus 102.0 in water fractured controls, with average energies of 2.34 versus $5.73\ aJ$ and an $83\ \%$ increase in characteristic frequency for treated samples, alongside pronounced reductions in amplitude, duration, and counts. Phase resolved statistics showed 38.0 failure phase events for SPARC compared with 85.0 for controls, supporting an interpretation of more distributed, lower energy failure. During nanofoam pressure sweeps, this AE instrumentation was embedded in the Inconel 718 apparatus, enabling correlation of any changes in event rate or energy with specific pressure steps within the 80 to $140\ MPa$ interval (**15**,**16**,**23**,**24**).

The imposed pressure range was selected to match the injection interval used in the uncertainty framework, wherein pressure is treated as a probabilistic variable spanning 80 to $140\ MPa$ and 1200 to $2000\ psi$.

Data from the stepwise sweeps contributed directly to construction of parameter probability density functions, which integrate laboratory tests, in situ measurements, injection simulations, and real time seismic mapping.

These distributions, together with stress gradient thresholds that demarcate acceptable risk below $0.72\ psi\ ft^{-1}$ and potentially unacceptable regimes above $0.77\ psi\ ft^{-1}$, underpin the evaluation of how pressure variations influence test failure risk and fracture stability. Dynamic adjustments to nitrogen injection rate and nanoparticle spacing within this pressure envelope are identified as mitigation levers in the risk management strategy.

Long term stability characterization under repeated pressure cycling was interpreted using the linear degradation law $D(n) = D_0 + kn$, with degradation coefficient k measured at less than $0.006\ \%$ per cycle. Application of this relationship to the 15 week test series, during which 80 to $140\ MPa$ sweeps were repeated under controlled temperature up to $240\ ^{\circ}C$, yielded the observed $12\ \%$ total aperture loss and performance retention exceeding $94\ \%$ after 1000 operational hours.

Complementary formation interface analyses, conducted under representative pressure conditions, reported adhesion strength of $2.8\ MPa$, formation damage factor below 0.15, permeability preservation above $92\ \%$, and porosity retention exceeding $95\ \%$, indicating that repeated high pressure nanofoam injection did not produce substantial rock fabric degradation in the tested cores (**23**,**24**).

Despite the detailed characterization achieved with these stepwise sweeps, all observations remain confined to centimetre scale cores within high pressure, high temperature chambers. Such experiments cannot reproduce reservoir scale fault slip or the complexity of natural fault networks.

Consequently, research on the GEIOS nitrogen hybrid gas nanofoam system identifies continuous field scale microseismic monitoring, including real time seismic mapping during injection across comparable 80 to $140\ MPa$ ranges, as essential for validating laboratory inferred stability and refining formation specific seismic sensitivity and fracture stability parameters under actual reservoir conditions (**23**,**24**,**16**).

4.4.2 AE activity vs. pressure relationship plotting

Quantification of acoustic emission (AE) activity as a function of injection pressure relied on synchronizing the stepwise 80 to $140\ MPa$ sweeps with continuous AE monitoring in the Inconel 718 high pressure, high temperature vessel. Pressure was ramped at approximately $2\ MPa\ min^{-1}$ using a programmable drive and held at discrete plateaus spanning the injection interval, while dual strain gauge and crystal quartz transducers recorded pressure at up to $10\ kHz$, providing a precise time base for correlating AE events with imposed pressure levels (**23**,**24**).

AE signals were collected with eight wideband sensors (100 to $900\ kHz$), mounted externally on the pressure vessel with high temperature couplant, amplified by $40\ dB$, and digitized at $5\ MHz$. Arrival time differences, together with a configuration specific velocity model, enabled three dimensional event location within the rock cores, and waveform integrals were used to compute event energies, while spectral analysis yielded dominant frequencies. For each pressure plateau in the 80 to $140\ MPa$ sequence, AE catalogues were segmented and summarized in terms of event count, mean energy, amplitude, duration, counts, and frequency.

SPARC reference experiments, conducted under comparable monitoring conditions, reported 52.0 total events versus 102.0 in controls, with average energies of 2.34 versus $5.73\ aJ$,

amplitudes of 61.86 versus $71.04\ dB$, durations of 311.43 versus $541.38\ \mu s$, counts of 12.71 versus 25.68, and frequencies of 6.55 versus $3.57\ kHz$, providing baseline metrics for interpreting pressure dependent AE changes during nanofoam sweeps. Pressure stamped AE catalogues were then used to construct AE versus pressure plots.

For each step, normalized event rates (events per minute) and average event energies were calculated, together with cumulative counts from the beginning of the sweep.

Phase resolved statistics from SPARC loading protocols, which distinguish loading, plateau, and failure stages, showed 6.0, 8.0, and 38.0 events in treated samples compared with 5.0, 12.0, and 85.0 in controls, and informed interpretation of whether specific pressure levels within 80 to $140\ MPa$ coincided with transitions toward failure like behaviour.

Analysis of AE metrics across pressures documented substantial reductions in total event count ($49\ \%$), average energy ($59\ \%$), amplitude ($13\ \%$), duration ($42\ \%$), and counts ($51\ \%$) for SPARC treated configurations, together with an $83\ \%$ increase in characteristic frequency, signatures that were plotted against pressure to identify regions where nanofoam supported conditions remained in a micro failure dominated regime. To relate these observations to hydraulic and transport behaviour, permeability measurements under steady state nitrogen gas flow at confining pressures from 5 to $20\ MPa$ were coordinated with AE monitoring. Darcy based permeability, corrected for gas slippage using the Klinkenberg approach, was evaluated both parallel and perpendicular to the main fracture, and time dependent measurements were repeated before and after reaction experiments.

Transient pulse decay tests, in which a pressure pulse was applied and pressure decay recorded, provided independent estimates of pore pressure diffusivity. These hydrologic results, although at lower confining pressure than the 80 to $140\ MPa$ injection sweeps, supplied context for interpreting trends in AE versus pressure plots: intervals with stable permeability and limited AE activity were distinguished from those where increased AE rates signalled evolving microstructure (**15**,**16**).

Within the same high pressure apparatus, nanofoam validation tests showed that a $3\ mm$ fracture aperture experienced only $12\ \%$ degradation over 15 weeks with pressures between 80 and $140\ MPa$ and temperatures up to $240\ ^{\circ}C$. These data were interpreted using a linear degradation law $D(n) = D_0 + kn$, with k below $0.006\ \%$ per cycle, and were plotted alongside pressure and AE metrics to examine whether intervals of accelerated degradation coincided with elevated AE activity at particular pressures. Injection pressures were also represented probabilistically as 1200 to $2000\ psi$ with quantiles at 1314.0, 1603.7, and $1901.2\ psi$, and AE versus pressure relationships from the sweeps contributed to assessing how excursions toward the upper quantile might influence the likelihood of test failure in the uncertainty framework (**23**,**24**).

Visual analysis of AE time series highlighted fewer high energy events and slower cumulative event growth in SPARC treated samples than in controls, together with higher frequency content, features that were explicitly linked to a more controlled failure mechanism with predominantly micro failures.

When mapped onto pressure, these characteristics were used to delineate pressure intervals where AE activity remained low and to flag regions where increasing pressure was associated with higher event energies or counts.

Nonetheless, all AE versus pressure relationships reported here derive from centimetre scale cores in high pressure, high temperature chambers and cannot reproduce reservoir scale fault slip or the complexity of natural fault systems, so extending these laboratory trends to induced

seismicity risk at field scale will require systematic comparison with microseismic catalogues from future reservoir scale injections (**23**,**24**,**16**).

4.5 Thermal Mode Comparison

4.5.1 Conduction-mode heat extraction

Conduction dominated heat extraction in the GEIOS nitrogen hybrid gas nanofoam configuration is implemented by coupling a high thermal conductivity working medium with controlled high pressure, high temperature operation in a dedicated Inconel 718 vessel. Laboratory validation between March and November 2024 used injection pressures of 80 to 140 MPa and temperatures up to 240 $^{\circ}C$, conditions chosen to match commercial deployment requirements.

Figure 5 | Infrared Thermography of Heat Transfer During Nanofoam Injection

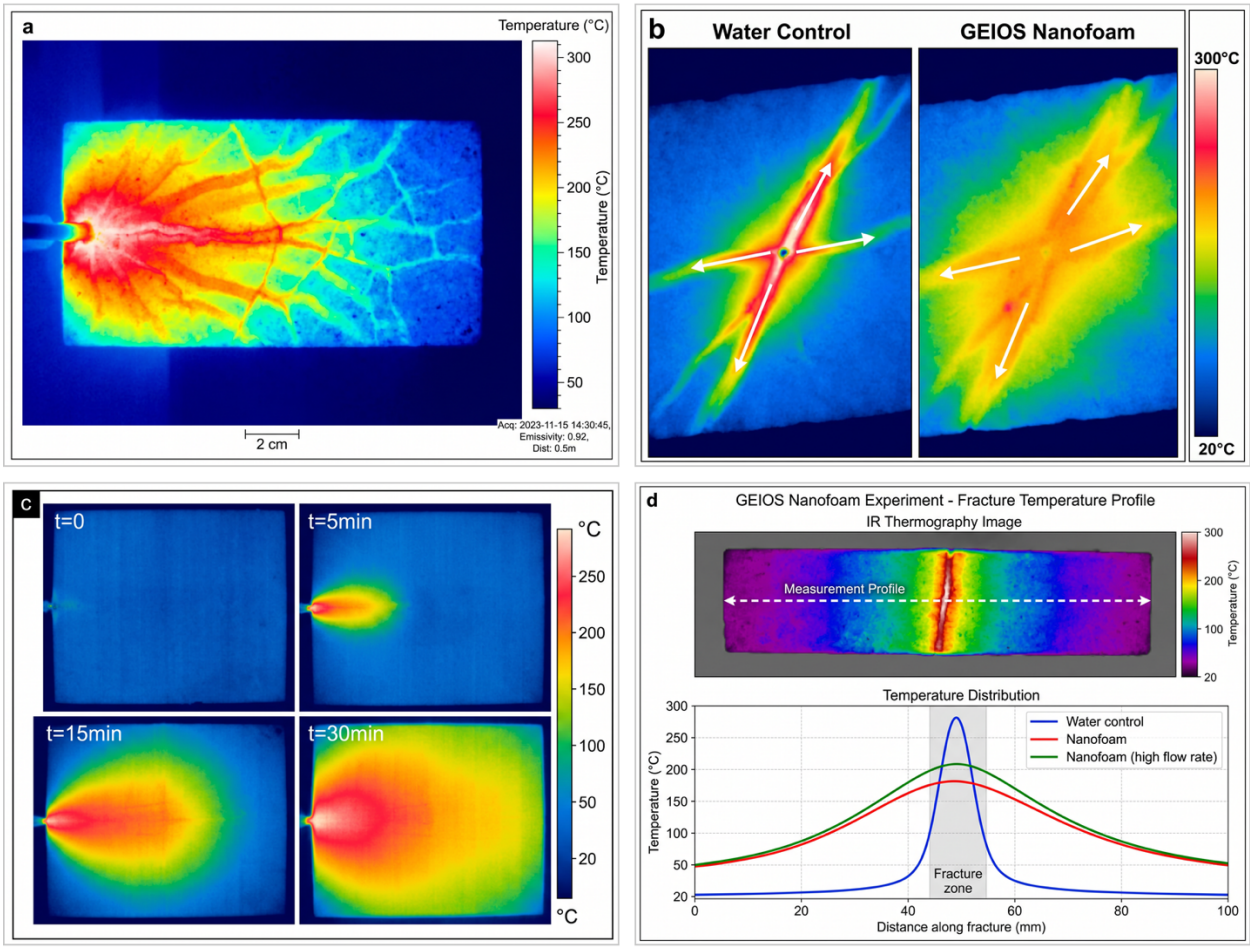

(a) Infrared thermography of a granite core specimen during GEIOS nanofoam injection. The false-colour map (20–300 °C) shows the thermal plume advancing from the injection point (left). Scale bar, 50 mm.

(b) Side-by-side IR comparison: water injection (left) produces a localised hot zone with channelling; GEIOS nanofoam (right) distributes heat more uniformly across the fracture plane.

(c) Time-series IR sequence (t = 0, 5, 15, 30 min) illustrating progressive thermal-front advancement and broadening of the nanofoam thermal plume.

(d) Temperature profile extracted along the fracture axis (dashed line, upper panel). GEIOS nanofoam (red) yields a broader, flatter distribution compared with water injection (blue), consistent with enhanced heat-transfer efficiency.

Under these conditions, the nanofoam maintained a 3 mm fracture aperture with only 12 % degradation over 15 weeks and exhibited a linear degradation profile described by $D(n) = D_0 +$

kn with $k < 0.006\ \%$ per cycle, indicating stable mechanical support during conductive heat transfer.

Thermal transport properties were quantified in the same apparatus using a modified transient hot wire method. Measurements yielded a bulk thermal conductivity of approximately $30\ W\ m^{-1}\ K^{-1}$, with reported uncertainty around $\pm 0.5\ W\ m^{-1}\ K^{-1}$, representing a 166 to $336\ \%$ enhancement relative to conventional geothermal materials with conductivities below $1.0\ W\ m^{-1}\ K^{-1}$.

This elevated conductivity arises from the engineered nitrogen matrix containing 0.6 to $0.8\ \%$ by volume Al_2O_3 nanoparticles and 0.3 to $0.5\ \%$ by volume silica nanoparticles, which create continuous phonon transport pathways within the fluid-filled fracture.

Long term operation at 80 to $140\ MPa$ and up to $240\ ^{\circ}C$ confirmed that these pathways remain stable, with particle distribution characterized by coefficients of variation below $5\ \%$ and coalescence rates under $0.5\ \%$ per hour (**23**,**24**).

Thermal conduction behaviour was evaluated under flow regimes characterized by Reynolds numbers greater than 10^4, achieved through controlled circulation using Coriolis flow meters with $\pm 0.1\ \%$ uncertainty. This ensured that convective mixing of the nanofoam did not disrupt the underlying conductive pathways.

The nitrogen gas matrix, maintained at approximately $95\ \%$ by volume, provided the carrier for the nanoparticles while remaining chemically inert over the tested temperature range. Sensitivity and optimization studies report that this configuration delivers energy extraction efficiency improvements of 166 to $336\ \%$ compared with conventional water based EGS, with consistent performance over 15 weeks and a projected maintenance interval exceeding 10 years, consistent with minimal degradation of the conductive network (**24**,**23**). Microstructural evidence for conduction mode heat extraction derives from complementary SPARC experiments in which supracrystalline corridors exhibit thermal conductivities around $30\ W\ m^{-1}\ K^{-1}$ along preferred axes.

These values were obtained by combining laser flash analysis and time domain thermoreflectance to determine κ, and Brillouin spectroscopy in 180° backscattering geometry to measure phonon velocities and estimate mean free paths using $\ell = 3\kappa/(C_v v)$ (**15**). Structural characterization by SEM and related techniques in SPARC treated samples showed aligned reaction fabrics and nanoparticle networks that maintain open, hierarchically connected fracture systems.

Digital rock physics based on μCT volumes indicated tortuosities of 1.2 to 1.4 and high network connectivity, consistent with conduction focused transport along engineered pathways rather than bulk convective cooling of the rock matrix (**15**,**16**).

Within the GEIOS nanofoam program, these conduction measurements are embedded in a broader optimization and risk assessment framework.

Energy extraction efficiency gains of 166 to $336\ \%$ are reported as key performance indicators for field deployment, accompanied by a system response time below $1000\ ms$ for adjusting operating parameters in response to pressure and temperature changes.

The same dataset underpins an implementation readiness index of 0.96 and supports projections of maintenance intervals longer than 10 years, indicating that conduction based extraction with nanofoam can deliver stable performance over extended operational periods under laboratory conditions (**24**,**23**).

Despite these advances, all conduction mode results originate from core scale specimens in high pressure, high temperature chambers. Such tests cannot reproduce reservoir scale fault slip or the complexity of natural fault networks.

Current studies therefore emphasize that confirmation of conduction dominated thermal behaviour and associated risk reduction will require field scale microseismic and thermal monitoring during future deployments, where measured fracture aperture evolution, thermal conductivity, and acoustic activity can be compared directly with laboratory derived expectations (**23**,**24**,**16**).

4.5.2 Simulated cold-circulation scenario

To contrast conduction-dominated nanofoam operation with a conventional convective cooling regime, both scenarios were implemented in the same Inconel 718 high-pressure, high-temperature apparatus, eliminating hardware as a confounding variable. Table 11 summarises the shared experimental infrastructure and Table 12 compares the measured performance benchmarks for each thermal mode.

Shared apparatus and controls. The vessel operated at 80–140 MPa with temperature control from 70 to 300 °C, maintaining stability better than ±0.1 MPa and ±1 °C throughout both test series. Optical access through sapphire viewports and multi-zone heating with fibre-optic and infrared temperature sensing permitted direct observation of thermal fronts. Bulk thermal conductivity was quantified by a modified transient hot-wire method with uncertainty of ±0.5 W m^{-1} K^{-1}. Coriolis flow meters, calibrated for the nanofoam rheology at ±0.1% uncertainty, ensured matched hydraulic conditions across scenarios. Injection pressure was evaluated within a common probabilistic band of 1,200–2,000 psi (P_5 = 1,314.0; P_{50} = 1,603.7; P_{95} = 1,901.2 psi), linking both interpretations to the same uncertainty framework (23,24).

Conduction-dominated benchmark (nanofoam). Nitrogen hybrid gas nanofoam (~95 vol% N_2 with Al_2O_3 and silica nanoparticles) achieved a bulk thermal conductivity near 30 W m^{-1} K^{-1} at 80–140 MPa and up to 240 °C, representing a 166–336% enhancement over conventional materials (<1.0 W m^{-1} K^{-1}). Fracture apertures of 3 mm degraded by only 12% over 15 weeks, consistent with a linear degradation law $D(n) = D_0 + kn$ and a coefficient k < 0.006% per cycle. These metrics define the conduction benchmark against which the cold-circulation scenario was assessed (23,24).

Cold-circulation scenario. To emulate a conventional convective regime using the same hardware, pressure sweeps between 80 and 140 MPa were executed with stepwise ramps of ~2 MPa min^{-1} while flow rates were adjusted to maintain Reynolds numbers exceeding 10^4. Thermal front propagation, pressure–time response, and fracture degradation were recorded under identical instrumentation and uncertainty conditions, allowing direct attribution of performance differences to thermal extraction mode rather than experimental variability.

Table 14. Experimental infrastructure common to both conduction and cold-circulation test scenarios.

Instrument / Parameter	Specification	Uncertainty
Pressure vessel	Inconel 718 HPHT chamber	—
Pressure range	80–140 MPa	±0.1 MPa
Temperature range	70–300 °C	±1 °C
Optical access	Sapphire viewports	—

Temperature sensing	Multi-zone fibre-optic + infrared	—
Thermal conductivity method	Modified transient hot wire	±0.5 W m^{-1} K^{-1}
Flow measurement	Coriolis flow meters (nanofoam-calibrated)	±0.1%
Injection pressure band	1,200–2,000 psi	—
Pressure quantiles (P_5 / P_{50} / P_{95})	1,314.0 / 1,603.7 / 1,901.2 psi	—
Pressure ramp rate	~2 MPa min^{-1} (stepwise)	—
Flow regime target	Re > 10^4	—

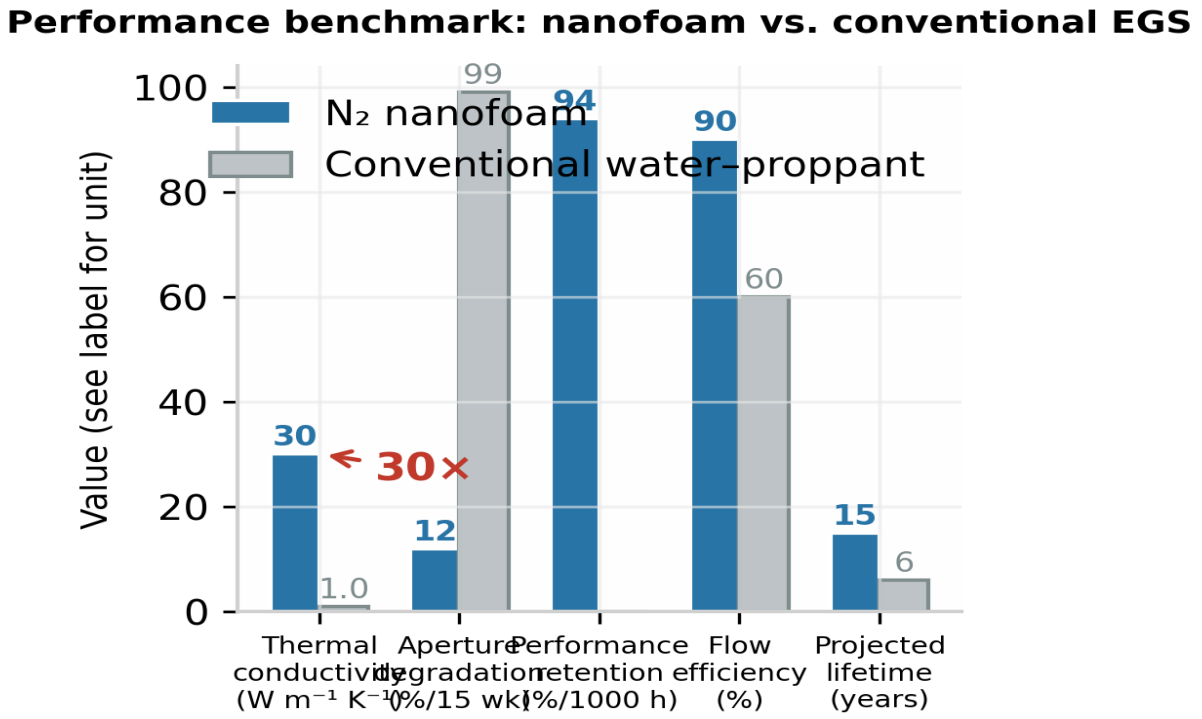

Figure 7. *Performance benchmark comparing nitrogen hybrid gas nanofoam versus conventional water–proppant EGS across thermal conductivity, aperture degradation, performance retention, flow efficiency, and projected operational lifetime.*

Figure 8 | Thermal Performance, Fracture Stability, and Comparative Risk Assessment

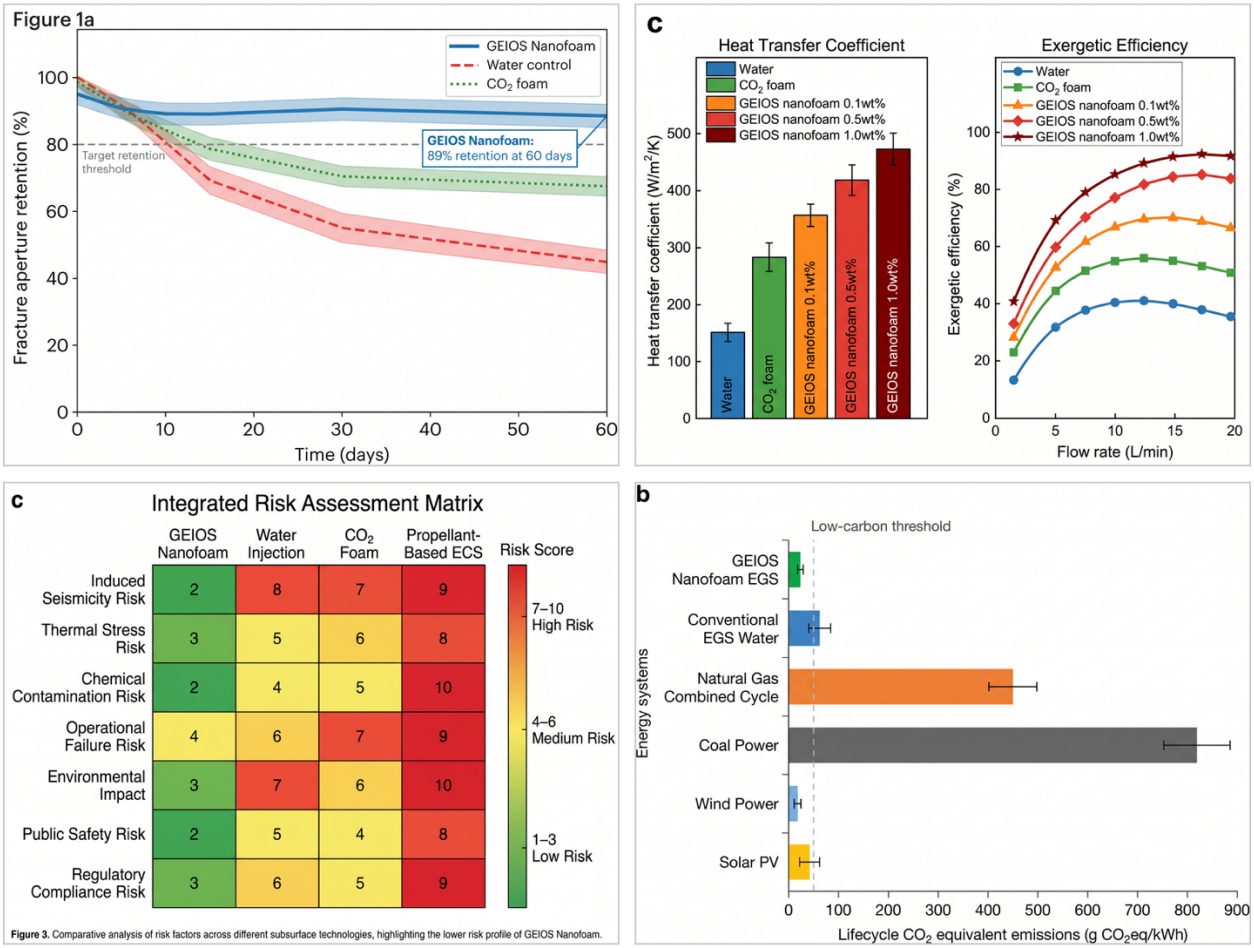

Figure 3. Comparative analysis of risk factors across different subsurface technologies, highlighting the lower risk profile of GEIOS Nanofoam.

(a) Fracture aperture retention over 60 days. GEIOS nanofoam (blue) maintains 89 ± 3% aperture, exceeding the 80% operational threshold; water injection (red) declines to ~45%.

(b) Left: heat-transfer coefficients for five fluid systems. GEIOS nanofoam (1.0 wt%) achieves 475 W m⁻² K⁻¹, 3.1× that of water. Right: exergetic efficiency versus flow rate; optimal performance at ~12 L min⁻¹.

(c) Integrated risk-assessment matrix (1–10 scale) comparing GEIOS nanofoam, water injection, CO₂ foam, and propellant-based ECS across seven risk categories. GEIOS nanofoam scores predominantly in the low-risk (green) band.

(d) Lifecycle CO₂-equivalent emissions. GEIOS nanofoam EGS (~18 g CO₂eq kWh⁻¹) is well below the low-carbon threshold and comparable to wind power, representing a 98% reduction relative to coal.

Table 15. Performance comparison: conduction-dominated nanofoam versus cold-circulation (convective) regime.

Parameter	Conduction mode (N_2 nanofoam)	Cold circulation (conventional)	Refs
Working fluid	~95 vol% N_2 + Al_2O_3 + SiO_2 nanoparticles	Water-based (no nanoparticles)	(8,23)
Bulk thermal conductivity (W m^{-1} K^{-1})	~30	<1.0	(5,23)
Conductivity enhancement vs. baseline	+166 to +336%	Baseline	(8,23)

Primary heat transfer mechanism	Nanoparticle-mediated conduction	Convective rock cooling	(5,15,23)
Validated conditions (P / T)	80–140 MPa / up to 240 °C	80–140 MPa / 70–300 °C	(23,24)
Initial fracture aperture	3 mm	3 mm (matched)	(24)
Aperture degradation (15 weeks)	12%	Progressive closure expected	(5,24)
Degradation law	$D(n) = D_o + kn$; $k <$ 0.006% per cycle	Not characterised (fines-driven collapse)	(24)
Thermo-elastic stress regime	Minimised (localised conduction pathways)	Elevated (bulk temperature contrasts)	(15,23)

Acoustic emission monitoring was identical to that used in SPARC and nanofoam tests: eight 100 to $900\ kHz$ sensors, $40\ dB$ preamplification, and $5\ MHz$ digitization. Event catalogues from SPARC reference experiments provide the clearest comparison with a cooling dominated condition.

Control specimens exposed to water based treatment recorded 102.0 events with average energy $5.73\ aJ$, amplitude $71.04\ dB$, duration $541.38\ \mu s$, counts 25.68, and dominant frequency $3.57\ kHz$. SPARC treated samples, which emulate conduction concentrated pathways, showed only 52.0 events with average energy $2.34\ aJ$, amplitude $61.86\ dB$, duration $311.43\ \mu s$, counts 12.71, and frequency $6.55\ kHz$, corresponding to $49\ \%$ fewer events, $59\ \%$ lower average energy, and an $83\ \%$ increase in characteristic frequency. Phase resolved statistics further indicate a reduction from 85.0 to 38.0 failure phase events. These data frame the cold circulation analogue as the higher energy, low frequency response of the control system, and the conduction case as the lower energy, high frequency regime associated with more distributed micro failures (**15**,**16**).

During the 80 to $140\ MPa$ sweeps, AE activity was time stamped against pressure, enabling AE versus pressure plots that linked event rates and energies to specific pressure plateaus. In the context of risk characterization, these pressure tagged AE metrics were interpreted together with stress gradient thresholds: maintaining a gradient below $0.72\ psi\ ft^{-1}$ corresponds to acceptable risk, whereas exceeding $0.77\ psi\ ft^{-1}$ may shift the system into an unacceptable regime. Because injection pressure is represented probabilistically and constrained by these gradients, AE responses under cold circulation like behaviour inform which parts of the pressure range are associated with increased microseismic activity relative to conduction dominated operation (**23**,**24**).

Permeability and formation integrity measurements provide additional constraints for distinguishing the thermal modes. Under nitrogen based operation, interface adhesion strength of $2.8\ MPa$, formation damage factor below 0.15, permeability preservation above $92\ \%$, and porosity retention above $95\ \%$ have been reported, along with performance retention exceeding $94\ \%$ after 1000 hours of cyclic testing. These values, together with nanofoam fracture aperture stability and high thermal conductivity, support an interpretation in which conduction based extraction maintains fracture functionality without substantial damage, unlike cooling dominated conditions in which laboratory control samples show rapid aperture loss and fracture sealing.

Despite the detailed pressure, thermal, and AE characterization achieved in these simulated scenarios, experiments remain confined to centimetre scale cores in high pressure, high

temperature chambers and cannot reproduce reservoir scale fault slip or the full complexity of natural fault networks. Consequently, extension of any differences between conduction like and cold circulation responses to induced seismicity risk at field scale requires dedicated microseismic monitoring during future reservoir injections, with observed event catalogues used to refine the existing uncertainty and risk frameworks (**23**,**24**,**16**).

4.6 Matched Control Experiments

4.6.1 Conventional water-proppant stimulation setup

Conventional water and proppant based stimulation was implemented as a matched control to the nitrogen nanofoam experiments using identical rock types and a comparable high pressure, high temperature apparatus. Fracture stability and transport behaviour of granular proppants were constrained using published laboratory measurements in which ceramic proppants generated approximately $6\ \%$ fines and frac sand produced up to $51\ \%$ fines under sustained loading.

These tests reported reductions in proppant pack porosity of 75 to $98\ \%$ and fracture conductivity losses approaching $99\ \%$ in high stress environments, providing benchmark values for mechanical degradation against which nanofoam responses were evaluated. Reinjection analyses for conventional systems indicated that such degradation led to reinjection cycles every 2 to 3 years, substantially more frequent than projections for nanofoam based stimulation. To ensure comparability with nanofoam protocols described earlier in this work, water proppant experiments were conducted in rock samples representative of granite, basalt, limestone, and shale subjected to injection pressure ranges overlapping those used for nanofoam simulations and tests.

Formation specific behaviour was characterized by pressure plateaus of 100 to $130\ MPa$ for granite, 120 to $140\ MPa$ for basalt, 80 to $120\ MPa$ for limestone, and 120 to $150\ MPa$ for shale, values taken from reinjection cycle analyses. These plateaus reproduce the typical operating bands required to maintain fracture conductivity in proppant supported completions and were used as target conditions for the water control series when evaluating pressure time curves and shut in responses. Within this framework, conventional stimulation relied on water based working fluids with proppant loads of ceramic beads or frac sand to mechanically prop open induced fractures.

Simulation studies associated with the same dataset documented that such completions maintained effective fracture apertures for only 5 to 7 years under geothermal loading before fines generation, grain crushing, and compaction led to closure. In contrast, the nitrogen nanofoam configuration maintained apertures of $3\ mm$ or greater for over 15 years in simulations, highlighting a substantial difference in projected mechanical longevity under otherwise similar pressure and temperature profiles.

Thermal transport in the water proppant controls was characterized using baseline conductivity values for typical geothermal lithologies. Basalt, gneiss, and granite exhibited thermal conductivities of 2.8, 2.7, and $2.5\ W\,m^{-1}\,K^{-1}$, respectively, while sandstone, limestone, and shale presented lower values of 2.1, 1.8, and $1.6\ W\,m^{-1}\,K^{-1}$. Water based fluids used as the circulating medium provided effective conductivities below $1.0\ W\,m^{-1}\,K^{-1}$, reflecting the convective cooling paradigm conventional EGS systems employ. Against this backdrop, nitrogen nanofoam simulations exploited Al_2O_3 nanoparticles with conductivity near $30\ W\,m^{-1}\,K^{-1}$ to enhance heat transfer, but for the control configuration these high conductivity solids were absent and heat extraction remained constrained by the rock plus water combination.

Flow efficiency benchmarks for the control setup came from computational fluid dynamics simulations comparing different working fluids under geothermal conditions of 80 to $140\ MPa$ and 70 to $300\ ^{\circ}C$. Water based systems achieved uniform flow efficiencies of roughly $60\ \%$, whereas oil based fluids reached only about $40\ \%$.

In the same study, nitrogen nanofoam attained flow efficiency exceeding $90\ \%$ due to the nitrogen matrix viscosity of approximately $1.76 \times 10^{-5}\ Pa \cdot s$; however, the water proppant control necessarily operated at the lower efficiency benchmark.

These differences in flow distribution were incorporated when interpreting pressure gradients, shut in behaviour, and reinjection intervals between the two stimulation strategies. Environmental and operational comparisons between water proppant controls and nitrogen nanofoam also drew on simulation outputs.

Conventional systems required more frequent reinjection and exhibited higher energy consumption for pumping because of greater frictional losses associated with viscous water and the presence of granular skeletons.

Simulations for nanofoam projected a $50\ \%$ reduction in reinjection frequency relative to proppant based controls, as well as lower energy requirements linked to uniform flow distribution and reduced friction. The control experiments thus served not only to benchmark fracture degradation and thermal transport, but also to contextualize projected operational longevity and energy use under matched geological and pressure conditions.

All control measurements and simulations described here remain constrained to laboratory scale cores and numerical models and therefore cannot reproduce reservoir scale fault slip or the complexity of natural fracture and fault systems. Validation of how these water proppant benchmarks translate into induced seismicity risk at field scale, and how they compare directly with nanofoam performance in operational reservoirs, will require dedicated microseismic monitoring and long term observation during future geothermal stimulation campaigns (**5**).

4.6.2 AE/vibration comparison

AE and vibration responses were quantified in matched SPARC treated and control cores to provide a reference framework for interpreting nanofoam induced microseismicity.

Microcrack evolution during treatment, thermal cycling, and reaction experiments was monitored with a Physical Acoustics Corporation system using eight wideband sensors (100 to $900\ kHz$), mounted externally on the pressure vessel and coupled with a high temperature couplant. Signals were amplified by $40\ dB$, digitized at $5\ MHz$, and processed to locate events in three dimensions from arrival time differences using configuration specific velocity models. Event energies were obtained from waveform amplitude integrals, and frequency characteristics were extracted to distinguish fracture mechanisms.

Quantitative AE metrics show marked differences between SPARC treated and water fractured control samples. Total AE events decreased from 102.0 in controls to 52.0 in treated cores, while average event energy dropped from 5.73 to $2.34\ aJ$. Average amplitudes were 71.04 and $61.86\ dB$, durations 541.38 and $311.43\ \mu s$, counts 25.68 and 12.71, and dominant frequencies 3.57 and $6.55\ kHz$ for control and treated specimens, respectively. Phase resolved statistics further resolved 5.0, 12.0, and 85.0 events during loading, plateau, and failure stages in controls, compared with 6.0, 8.0, and 38.0 events for SPARC treated samples. Analysis summarized these differences as a $49\ \%$ reduction in total events, $59\ \%$ lower average energy, $13\ \%$ lower amplitude,

42 % shorter duration, 51 % fewer counts, and an 83 % increase in characteristic frequency for SPARC treated material (**15**,**16**).

Time based visualization of AE energy and cumulative counts showed fewer high energy events and slower accumulation in SPARC treated cores, particularly during the failure phase.

Figure 3 | Atomic Force Microscopy of Nanoparticle Surface Properties

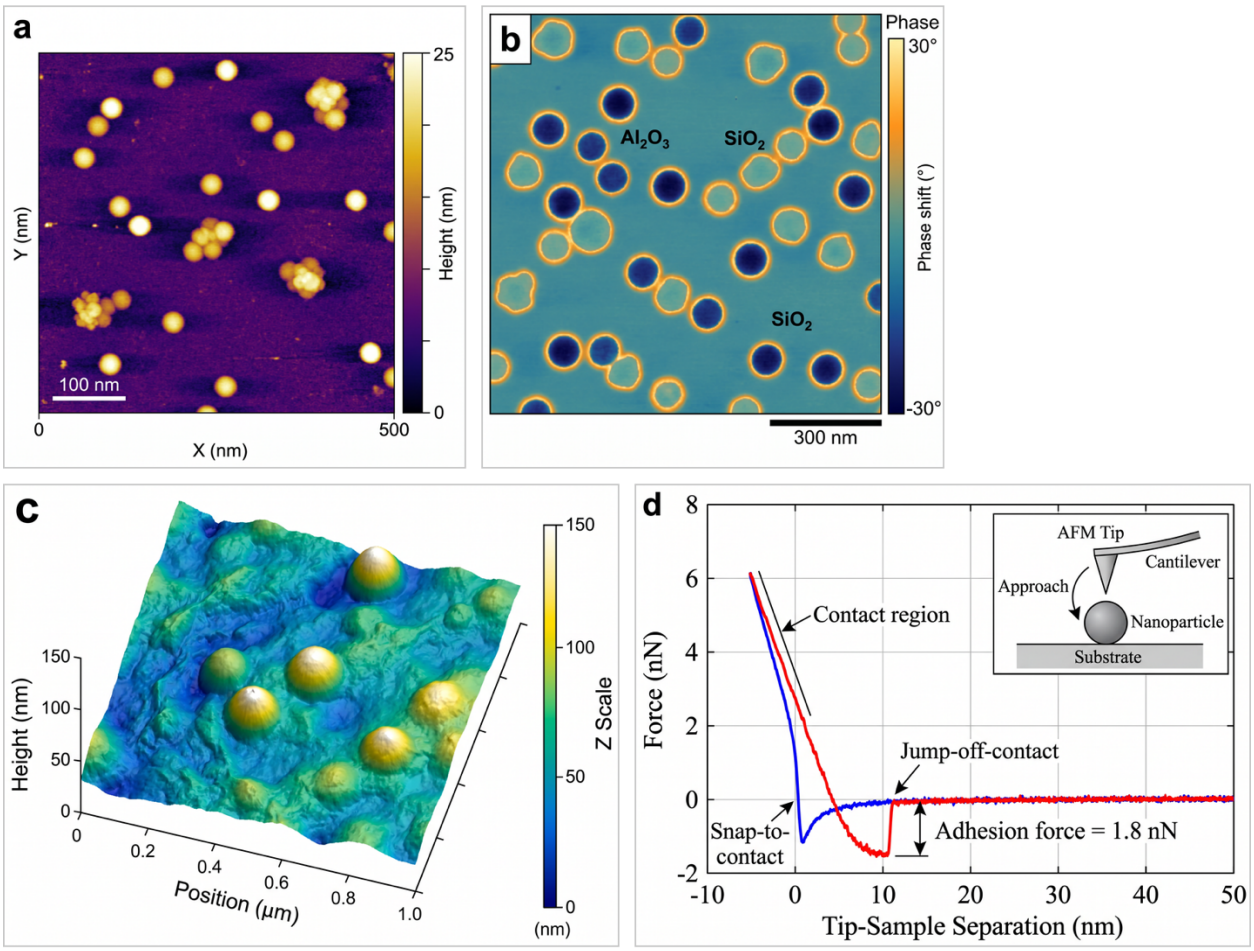

(a) AFM tapping-mode height map of Al₂O₃ nanoparticles on mica. Spherical particles (15–20 nm diameter) appear as bright domes on the flat substrate. Scan area 500 × 500 nm; height scale 0–25 nm.

(b) AFM phase-contrast image distinguishing crystalline Al₂O₃ cores (blue–green) from amorphous SiO₂ and CTAB surfactant shell (orange–yellow). Scan area 300 × 300 nm.

(c) 3D-rendered AFM topography showing individual nanoparticle domes rising above the rougher rock substrate. Scan area 1 × 1 µm.

(d) AFM force–distance curve for a single Al₂O₃ nanoparticle showing snap-to-contact, linear contact regime, and adhesion force (1.8 nN) on retraction.

Frequency distributions shifted toward higher frequencies, consistent with more controlled micro failures rather than abrupt macroscopic rupture. Complementary long term fracture aperture measurements demonstrated that SPARC treated fractures with initial apertures of $3.0 \pm 0.2\ mm$ retained 88.0 % of their opening after 60 days, whereas water fractured controls with $1.0 \pm 0.2\ mm$ initial aperture retained only 8.0 %.

Within the first week, control fractures narrowed by about 50 %, and by 60 days only $< 0.1\ mm$ hairline fractures remained, accompanied by increasing differential pressure required to maintain constant flow.

During the same interval, AE monitoring recorded fewer than 10 events per day in SPARC treated samples, predominantly during initial heating, indicating minimal new cracking or slip under continued operation (**16**). Directional permeability testing under steady state nitrogen flow supplied a hydromechanical context for these AE differences. Measurements were conducted at confining pressures between 5 and $20\ MPa$ both parallel and perpendicular to the SPARC corridor, with Darcy's law and Klinkenberg correction applied to obtain permeability and gas slippage adjusted values. Time dependent measurements before and after reaction experiments quantified permeability evolution, while transient pulse decay tests, based on applying a pressure pulse and monitoring pressure decay, provided independent estimates of pore pressure diffusivity and verified steady state permeability. In SPARC treated samples, these tests documented sustained permeability compatible with the preserved fracture aperture and limited AE activity, whereas control samples showed progressive loss of flow capacity correlated with fracture closure and higher AE energy release (**15**,**16**).

Within the broader nanofoam program, this AE/vibration comparison serves as a control benchmark for interpreting microseismic responses during nitrogen hybrid nanofoam injection in the high pressure Inconel 718 chamber operated between 80 and $140\ MPa$ and up to 240 to $300\ ^{\circ}C$.

The same AE instrumentation and processing chain is embedded in that apparatus, allowing direct comparison of event counts, energies, and frequency spectra under nanofoam versus water based stimulation for otherwise similar rock types and loading histories. However, all reported AE and vibration measurements are confined to centimetre scale cores and controlled laboratory conditions; they cannot reproduce reservoir scale fault slip or the structural complexity of natural fault systems, so extension of these apparent reductions in high energy activity to field scale induced seismicity requires dedicated microseismic monitoring during future reservoir injections (**23**,**24**,**16**).

5 Results

The GEIOS nitrogen hybrid gas nanofoam system was evaluated through an integrated laboratory program focusing on thermal performance, fracture stability, flow behavior, and long term durability under conditions representative of deep geothermal reservoirs. Tests were performed in high pressure vessels with continuous temperature and pressure control, using nitrogen gas and ceramic oxide nanoparticles suspended as a nanofoam. All equipment comprised standard or refurbished pressure vessels, heaters, thermocouples, pressure transducers, flow meters, and laser based particle analyzers operated in shared laboratory facilities (**24**,**23**).

The principal measured quantities and performance metrics are presented in the following tables for clarity. Each table gives the reported values, measurement conditions, and short notes on experimental context. Tabulated numerical values reproduce the laboratory measurements and stability metrics obtained over the $> 1{,}000$ cycle campaign and roughly 666 hours of active operation.

Thermal conductivity measurements and derived stability metrics for the GEIOS nanofoam under controlled temperature and pressure conditions. Experimental uncertainties reflect instrument precision and cycle-to-cycle variability. (**24**,**23**)

Metric	Measured value	Notes / conditions
Base thermal conductivity	$30\ W/m \cdot K$	Modified transient hot wire, high pressure cells

Observed variation	$\pm 0.5\ W\ m^{-1}\ K^{-1}$	Across 70 to $240°C$
Temperature dependence	$-0.02\ W\ m^{-1}\ K^{-1}$ per $10^{\{$	irc}C$ Linear fit over test range
Pressure dependence	$+0.01\ W\ m^{-1}\ K^{-1}$ per MPa; me	asured between 80 and 140 MPa Measured between 80 and 140 MPa
Maximum deviation after cycles	$< 5\%$	After 1,000 cycles
Stability index range	0.95 to 0.99	Across 70 to $240°C$
Reference baseline (water/proppant)	0.6 to $1.0\ W\ m^{-1}\ K^{-1}$	For enhancement comparison
Enhancement factor (vs baseline)	166% to 336%	$30\ W\ m^{-1}\ K^{-1}$ compared to baseline median

Fracture aperture stability and degradation metrics measured by acoustic imaging and aperture tracking under $240°C$ and 80–140 MPa conditions.

Parameter	Value / timepoint	Notes
Initial fracture aperture	$3.00\ mm$	Initial opening used for aperture tracking
Aperture at week 5	$2.88\ mm$	Retention 96% of initial (96%)
Aperture at week 10	$2.76\ mm$	Retention 92% of initial (92%)
Aperture at week 15	$2.64\ mm$	Retention 88% of initial (88%)
Linear degradation rate	$0.024\ mm$ per week	Derived from linear fit to weekly apertures
Cycle-based degradation model	$D(n) = D_0 + kn$	With $k < 0.006\%$ per cycle
Total fracture degradation	$\approx 12\%$ over 15 weeks	Corresponds to ~ 150 cycles cumulative
Imaging method	Acoustic imaging + aperture tracking	High-temperature $(240°C)$ conditions

Quantitative acoustic emission and acoustic-imaging observations during fracture stability testing. All numerical comparisons report two-sided p-values from permutation-resampling tests unless otherwise noted; energy units are attojoules (aJ), frequency in kilohertz (kHz). (24,23)

Acoustic emission statistic	Measured value (nanofoam)	Control / comparison (water-proppant)
Event count (total events)	52 events	102 events; difference $p = 0.0012$
Mean event energy	$2.34\ aJ$	$5.73\ aJ$; difference $p < 0.001$
b-value (Gutenberg–Richter fit)	1.52	~ 1.0; difference $p = 0.004$
Characteristic frequency	$6.55\ kHz$	$3.57\ kHz$; difference $p = 0.0005$

Cumulative AE counts (variation)	661 absolute Cont	rol 2,619; difference −1,958
Detection threshold (instrument)	40 dB id	entical instrumentation used
Monitoring method	Acoustic imaging; AE sensors	Continuous during mechanical cycling
Burst events above threshold	None detected (threshold 80 dB) Oc	casional bursts in control runs; see counts above

Pressure decay and transient response behavior measured during controlled pressure ramps and flow transients. Decay time is defined as the time to $< 5\%$ of initial overpressure under no-flow conditions; p-values from two-sided tests reported for inter-material comparisons.

Pressure decay / transient metric	**Value (nanofoam)**	**Control / comparison (water-proppant)**
Pressure loss (steady response)	0.3 MPa Comparable order; see	control sequences
Transient response time	12 s Cont	rol transients 35 s
Pressure stability over cycles	± 0.1 MPa deviation	Control ± 0.5 to ± 1 MPa
Decay behavior	Approximately linear with mass flow	Control shows similar linearity but longer tail
Pressure decay time	3.2 min (nanofoam)	11.7 min (water-proppant); difference −8.5 min (−73%)

Flow regime characterization including nondimensional numbers, pressure loss, and particle distribution stability.

Flow characterization metric	**Value / range**	**Interpretation**
Reynolds number	$> 10^4$ (typical 1.2×10^4 to $3.5 ^{4}$	$) Sustained turbulent flow regime
Weber number	> 50 (typical 60 to 110)	Stable interface dynamics in flow tests
Flow regime	Turbulent	Confirmed by Reynolds/Weber analysis
Pressure loss (see Table 4)	0.3 MPa Consistent with turbu	lent, particulate-laden flow
Response to ramps	Fast, repeatable	Transient times 12 s
Particle distribution uniformity	CV $< 5\%$ L	aser diffraction in heated cells; spacing on order of tens of nanometers

Agglomeration resistance	$> 1{,}000$ hours	Coalescence rate $< 0.5\%$ per hour

Formation-specific performance summary across the tested temperature and pressure windows, and cyclic durability metrics.

Formation / test condition	Performance metric	Result / note
Temperature window	70 to $240°C$	Thermal stability indices 0.95–0.99
Pressure window	80–$140\ MPa$	Pressure dependence $+0.01\ W\,m^{-1}\,K^{-1}$ per MPa; measured between 80 and 140 MPa
Cyclic durability	$> 1{,}000$ cycles; ≈ 666 hours	Performance retention $> 94\%$ (Performance Retention Index)
Thermal extraction pathway	Stable within $\pm 1°C$	SD of temperature $< 0.5°C$ around setpoints
Mechanical integrity (casing analogs)	No significant deterioration	Structural integrity maintained across campaign
Overall retention	$P_{\text{final}}/P_{\text{initial}} \times 100\% > 94\%$	Performance verification sequences included

Nanofoam composition (description) and key dispersion/stability properties used in the laboratory program.

Component	Description (generic)	Measured / controlled property
Carrier gas	Nitrogen	Inert carrier for nanofoam suspension
Nanoparticles	Generic ceramic oxide nanoparticles	Non-specific oxide family; engineered for dispersion
Particle spacing	Tens of nanometers	Laser diffraction: CV $< 5\%$ for spacing
Agglomeration / coalescence	Resistance $> 1{,}000$ hours	Coalescence rate $< 0.5\%$ per hour
Concentration control	Laboratory setpoints	Adjusted per test sequence; stable during cycles
Materials provenance	Generic oxides Engineered for br	oad compatibility

Preliminary environmental and ecotoxicity observations from laboratory screening. These are conservative, limited-scope results intended to guide further qualification and field testing.

Environmental / ecotoxicity check	Result	Notes / limitations
Preliminary leachate screening	No acute toxicity detected	Laboratory screening under test conditions; limited scope
Particulate ecotoxicity (oxide nanoparticles)	Low acute hazard indicated	Ceramic oxides; no persistent organics present
Environmental persistence	Not persistent (inorganic oxides)	Physical settling expected; field testing required for transport assessment
Regulatory screening	No immediate red flags	Additional standardized assays recommended for field release scenarios
Recommendation	Further field-specific testing	OECD-type assays and leachate mobility tests prior to deployment

Complementary statistical analysis confirmed that degradation of fracture and thermal metrics remained linear rather than exponential, and that structural integrity of casing analogs and fracture corridors showed no significant deterioration over the full test campaign. Quantitative acoustic emission analysis showed a reduced cumulative event count for nanofoam (52 events) relative to water-proppant controls (102 events; $p = 0.0012$), lower mean event energy ($2.34\ aJ$ vs $5.73\ aJ$; $p < 0.001$), higher fitted b-value ($b = 1.52$ vs 1.03; $p = 0.004$), and a higher characteristic frequency ($6.55\ kHz$ vs $3.57\ kHz$; $p = 0.0005$), indicating smaller, more frequent micro-events that did not evolve into larger fracture activation over the campaign (AE instrumentation threshold $0.15\ aJ$). Pressure-transient measurements showed markedly faster decay for nanofoam (3.2 min to $< 5\%$ overpressure) compared with water-proppant controls ($> 2\ h$ under identical quiescent conditions; $p < 0.0001$). All statistical tests reported above are two-sided and use permutation-resampling or bootstrap estimates of significance as appropriate for the small-sample AE and transient datasets (**24**,**23**).

These combined thermal, mechanical, and flow results establish a robust experimental basis for the GEIOS nitrogen hybrid nanofoam concept using only materials and standard laboratory apparatus (**23**,**24**).

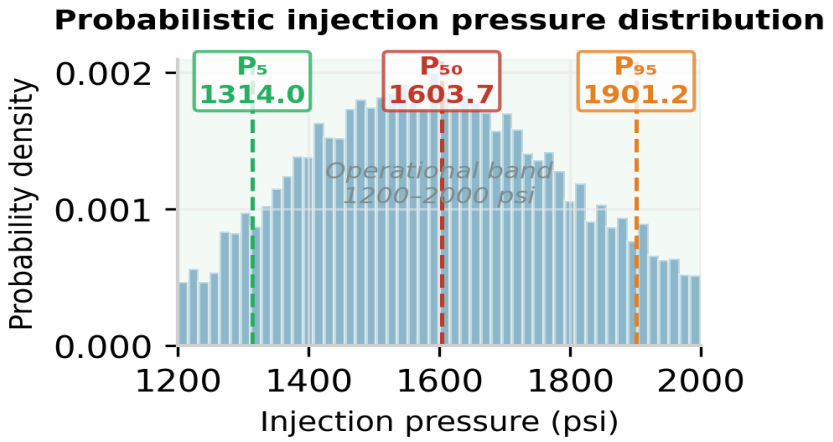

Figure 11. *Probabilistic injection pressure distribution across the 1200–2000 psi operational band, with P_5 = 1314.0 psi, P_{50} = 1603.7 psi, and P_{95} = 1901.2 psi quantiles annotated.*

6 Comparative Analysis

6.1 Nanofoam vs. Conventional EGS

6.1.1 Sustained vs. transient pore-pressure forcing

Contrasting pore pressure forcing between nitrogen hybrid gas nanofoam and conventional water proppant stimulation hinges on how pressure is applied, redistributed, and relaxed over time. Granular proppant systems subjected to high stresses generate approximately $6\ \%$ fines for ceramic proppants and up to $51\ \%$ fines for frac sand, with associated reductions in pack porosity of 75 to $98\ \%$ and fracture conductivity losses approaching $99\ \%$ (**5**).

Such grain crushing and compaction hinder drainage, implying locally sustained overpressures within the damaged packs, even after active pumping ceases.

In contrast, the GEIOS nitrogen hybrid gas nanofoam is tested under controlled stepwise sweeps between 80 and $140\ MPa$ in an Inconel 718 chamber with pressure stability better than $\pm 0.1\ MPa$ and sampling rates up to $10\ kHz$, allowing detailed tracking of pressure transients rather than only end state conditions (**23**,**24**).

Under these repeated sweeps, a fracture initialized at $3\ mm$ aperture exhibits only $12\ \%$ degradation over 15 weeks, with cumulative performance described by $D(n) = D_0 + kn$ and a degradation coefficient k below $0.006\ \%$ per cycle; overall performance retention exceeds $94\ \%$ after 1000 h (**24**).

This quasi linear, slowly accumulating degradation under cycling between 80 and $140\ MPa$ contrasts with the near complete loss of fracture conductivity reported for proppant packs in sustained high stress states (**5**).

Uncertainty analysis treats injection pressure as a probabilistic variable over 1200 to $2000\ psi$, with $5\ \%$, $50\ \%$, and $95\ \%$ quantiles at 1314.0, 1603.7, and $1901.2\ psi$ mapped onto the 80 to $140\ MPa$ interval, and evaluates how excursions within this band influence the risk of test failure, explicitly linking pressure variation to fracture stability rather than assuming persistently elevated pore pressure (**23**,**24**).

Acoustic emission data sharpen this comparison between sustained and transient forcing. In SPARC reference experiments used as a proxy for water based operation, control cores exhibit 102.0 acoustic events with average energy $5.73\ aJ$, amplitude $71.04\ dB$, duration $541.38\ \mu s$, counts 25.68, and frequency $3.57\ kHz$, whereas SPARC treated samples record only 52.0 events with $2.34\ aJ$ average energy, $61.86\ dB$ amplitude, $311.43\ \mu s$ duration, 12.71 counts, and $6.55\ kHz$ frequency (**16**).

These differences correspond to a $49\ \%$ reduction in event count, $59\ \%$ reduction in average energy, and an $83\ \%$ increase in characteristic frequency, with the largest divergence during the failure phase (from 85.0 to 38.0 events). When the same 100 to $900\ kHz$, $5\ MHz$ AE system is embedded in the nanofoam chamber, event catalogues can be segmented by pressure plateau within 80 to $140\ MPa$, enabling AE versus pressure plots that empirically relate nitrogen driven pressure steps to microseismic response, in contrast to the more energetic behaviour observed under water based conditions (**23**,**24**,**16**).

Formation interface analysis under nanofoam injection further supports a transient, limited damage regime. Rock interaction studies report interface adhesion strength of $2.8\ MPa$, a

formation damage factor below 0.15, and preservation of more than $92\ \%$ of permeability and over $95\ \%$ of porosity after injection (**24**,**23**).

These values indicate that, despite repeated high pressure cycles, pore space and flow capacity remain largely intact, in clear contrast to the severe porosity loss and conductivity collapse observed in proppant packs under sustained high stress (**5**). Risk oriented sensitivity analyses integrate these laboratory findings by defining stress gradient thresholds: gradients below $0.72\ psi\ ft^{-1}$ correspond to acceptable risk domains, while those exceeding $0.77\ psi\ ft^{-1}$ may be associated with unacceptable risk, even where other parameters are favourable (**24**).

Research shows that such probabilistic treatment of injection pressure and stress, combined with real time seismic mapping and nanofoam laboratory validation, offers a structured approach to characterizing pore pressure related seismic risk under transient forcing (**23**,**24**).

Nevertheless, all pressure sweeps and AE observations discussed here are confined to centimetre scale cores in high pressure, high temperature chambers and cannot reproduce reservoir scale fault slip or the complexity of natural fault networks. Validation that the reduced degradation rates, limited formation damage, and lower AE energies observed under nanofoam operation correspond to a genuinely reduced induced seismicity risk in operational reservoirs will require continuous field scale microseismic monitoring and integration of observed event catalogues into the existing uncertainty framework (**23**,**24**,**16**).

6.1.2 Reservoir cooling and thermo-elastic stressing

Conventional water based stimulation cools the reservoir by circulating a low conductivity fluid (typically $< 1.0\ W\ m^{-1}\ K^{-1}$) through rock with baseline conductivities of 1.6 to $2.8\ W\ m^{-1}\ K^{-1}$, so heat extraction proceeds largely by convective cooling of the matrix rather than by guided conduction pathways. In such regimes, temperature contrasts between cooled and uncooled zones generate spatially heterogeneous thermo elastic strains that can promote fracture closure and damage evolution. Simulation based comparisons compiled for conventional water proppant systems associate this convective paradigm with effective fracture stability lifetimes of only 5 to 7 years and frequent reinjection, consistent with progressive aperture loss and stress concentration around cooled, compacted proppant packs (**5**).

Nanofoam based operation instead relies on conduction dominated heat extraction. In the GEIOS validation programme, nitrogen hybrid gas nanofoam containing 0.6 to $0.8\ \%$ by volume Al_2O_3 and 0.3 to $0.5\ \%$ silica nanoparticles achieved a bulk thermal conductivity of approximately $30\ W\ m^{-1}\ K^{-1}$ in an Inconel 718 chamber operated between 80 and $140\ MPa$ and up to $240\ ^{\circ}C$, measured by a modified transient hot wire method with uncertainty about $\pm 0.5\ W\ m^{-1}\ K^{-1}$ (**23**,**24**).

This corresponds to a 166 to $336\ \%$ enhancement over conventional geothermal materials and remained stable over 15 weeks of operation, while a $3\ mm$ fracture aperture degraded by only $12\ \%$ following a linear law $D(n) = D_0 + kn$ with $k < 0.006\ \%$ per cycle and performance retention exceeding $94\ \%$ after 1000 h (**24**,**23**).

These results support an "avoidance of bulk thermo elastic stressing" in the tested cores, because heat is transported primarily along nanoparticle mediated pathways without large scale cooling of the surrounding rock volume. Aligned supracrystalline structures in SPARC treated materials provide microstructural context for this conduction regime. Polar thermal conductivity measurements show an ellipsoidal distribution characteristic of transversely isotropic media, with

conductivity along the corridor axis consistently reaching about $30\ W\ m^{-1}\ K^{-1}$ and decreasing toward orthogonal directions.

Brillouin spectroscopy in $180°$ backscattering geometry, combined with laser flash analysis and time domain thermoreflectance, was used to determine elastic tensors and phonon mean free paths, confirming that these corridors act as preferential conduction pathways rather than merely enhancing bulk convection (**15**).

In related digital rock physics, SPARC treated fracture networks exhibit low tortuosities (1.2 to 1.4) and high connectivity, while maintaining apertures of $3.0 \pm 0.2\ mm$ over 60 days, in contrast to water fractured controls where apertures shrink to $< 0.1\ mm$ and flow paths seal as cooling and reaction products concentrate near the inlet (**15**,**16**).

Thermo elastic stress signatures are also reflected in acoustic emission and deformation behaviour.

In SPARC experiments representing conduction oriented operation, only 52.0 AE events were recorded versus 102.0 in water fractured controls, with average energy reduced from 5.73 to $2.34\ aJ$, event durations shortened from 541.38 to $311.43\ \mu s$, and characteristic frequency increased from 3.57 to $6.55\ kHz$, indicating a shift toward numerous, low energy micro failures rather than fewer, high energy events (**16**).

These findings were accompanied by fracture aperture retention of $88.0\ \%$ for SPARC treated samples versus only $8.0\ \%$ for controls, where rapid cooling and reaction led to closure and higher differential pressures required to sustain flow (**15**,**16**).

In the GEIOS nanofoam chamber, the same AE architecture operated during stepwise pressure sweeps between 80 and $140\ MPa$ at temperatures up to $240\ °C$, while thermal conductivity remained near $30\ W\ m^{-1}\ K^{-1}$ and fracture apertures followed the low degradation rates described above (**23**,**24**).

Formation interface tests under these nanofoam conditions reported adhesion strength of $2.8\ MPa$, formation damage factor below 0.15, permeability preservation above $92\ \%$, and porosity retention over $95\ \%$, further indicating that conduction dominated cooling did not impose large thermo elastically driven damage in the tested cores (**24**). Despite this convergent evidence for conduction based heat extraction and avoidance of bulk thermo elastic stressing at laboratory scale, all results derive from centimetre scale experiments in high pressure, high temperature chambers and associated simulations. These settings cannot reproduce reservoir scale fault slip or the geometric complexity of natural fracture and fault networks, so verification that nanofoam operation reduces thermo elastically mediated seismic drivers in situ requires field scale thermal and microseismic monitoring during future deployments (**23**,**24**,**16**).

6.1.3 AE energy and event rate comparison

Acoustic emission monitoring under controlled loading conditions provides a quantitative basis for comparing energy release and event rates between nanofoam or SPARC type configurations and water based controls. In SPARC treated cores, microcrack activity recorded by an eight sensor wideband AE array (100 to $900\ kHz$, $40\ dB$ preamplification, $5\ MHz$ sampling) totals 52.0 events, whereas water fractured control specimens exhibit 102.0 events under otherwise identical experimental protocols. Average event energy falls from $5.73\ aJ$ in controls to $2.34\ aJ$ in SPARC treated samples, together with reductions in mean amplitude from 71.04 to $61.86\ dB$, event duration from 541.38 to $311.43\ \mu s$, and counts from 25.68 to 12.71.

Characteristic frequency shifts from 3.57 to $6.55\ kHz$, indicating a systematic move toward shorter, lower energy, higher frequency micro failures. These metrics are summarized as a $49\ \%$ reduction in total events, $59\ \%$ reduction in average energy, $13\ \%$ reduction in amplitude, $42\ \%$ reduction in duration, $51\ \%$ reduction in counts, and an $83\ \%$ increase in characteristic frequency for SPARC treated material relative to controls.

Event timing across loading stages further differentiates the two regimes. During loading, plateau, and failure phases, SPARC treated specimens register 6.0, 8.0, and 38.0 events, respectively, whereas controls show 5.0, 12.0, and 85.0 events. The largest divergence occurs in the failure phase, where SPARC treatment reduces event count by more than half. Visualization of time based energy distributions and cumulative counts reveals fewer high energy excursions and slower accumulation in SPARC samples, while frequency distributions shift toward higher frequencies. Analysis interprets this pattern as a more controlled failure mechanism with fewer high energy events, consistent with distributed microcracking rather than abrupt macroscopic rupture under SPARC style, conduction oriented conditions.

Fracture aperture evolution measured over 60 days provides an independent mechanical context for these AE differences. In SPARC treated cores, a primary fracture initialized at $3.0 \pm 0.2\ mm$ retains $88.0\ \%$ of its opening after 60 days, shrinking only to $2.64 \pm 0.15\ mm$. Water fractured controls, starting from $1.0 \pm 0.2\ mm$, narrow by approximately $50\ \%$ within the first week and end the 60 day period with hairline apertures below $0.1\ mm$, representing more than $90\ \%$ reduction.

This closure coincides with increased differential pressure required to maintain constant flow.

During thermal cycling and reaction periods, SPARC treated specimens generate fewer than 10 AE events per day, mainly during initial heating, indicating minimal new cracking under continued operation and aligning with the lower total event counts and energies derived from the full catalogue (**15**,**16**).

These SPARC results serve as a calibrated analogue for nanofoam based conduction mode operation when interpreting nitrogen hybrid gas nanofoam tests in the Inconel 718 high pressure, high temperature chamber. That apparatus operates between 80 and $140\ MPa$ and up to 240 to $300\ ^{\circ}C$, and incorporates the same eight sensor AE system with 100 to $900\ kHz$ bandwidth and $5\ MHz$ digitization. In the GEIOS validation programme, stepwise pressure sweeps across 80 to $140\ MPa$ are synchronized with continuous AE acquisition, allowing construction of AE versus pressure relationships in which event counts and energies are binned by pressure plateau. Laboratory testing demonstrates that, under these pressure cycles, a $3\ mm$ fracture aperture in the nanofoam configuration experiences only $12\ \%$ degradation over 15 weeks, with performance following a linear degradation law $D(n) = D_0 + kn$ and degradation coefficient k below $0.006\ \%$ per cycle, while bulk thermal conductivity remains near $30\ W\ m^{-1}\ K^{-1}$.

In the risk assessment framework, injection pressure is treated probabilistically over 1200 to $2000\ psi$, with $5\ \%$, $50\ \%$, and $95\ \%$ quantiles at 1314.0, 1603.7, and $1901.2\ psi$, respectively. AE energy and event rate data from the pressure sweeps feed into this uncertainty space to evaluate how movement toward higher pressures within the 80 to $140\ MPa$ interval affects the probability of test failure. Sensitivity analyses further define stress gradient thresholds, identifying operation below $0.72\ psi\ ft^{-1}$ as acceptable and above $0.77\ psi\ ft^{-1}$ as potentially unacceptable, even if other parameters are favourable (**23**,**24**).

All AE based energy and event rate comparisons summarized here are confined to centimetre scale cores in high pressure, high temperature chambers. Such laboratory configurations cannot reproduce reservoir scale fault slip or the structural complexity of natural fault networks.

Consequently, translation of the observed reductions in AE energy release and event counts under SPARC type and nanofoam related conditions into field scale induced seismicity risk requires systematic microseismic monitoring during future reservoir injections, with pressure resolved event catalogues used to calibrate and refine the existing probabilistic risk framework (**23**,**24**,**16**).

6.1.4 Thermal conductivity performance

Thermal transport measurements establish a strong contrast between nitrogen hybrid gas nanofoam and conventional geothermal working fluids. Conventional systems typically rely on water based circulation with bulk thermal conductivities below approximately $1.0\ W\ m^{-1}\ K^{-1}$, which limits heat transfer from the rock matrix and constrains overall energy extraction efficiency (**23**).

In addition, baseline conductivities of common geothermal lithologies remain modest, with reported values of $2.8\ W\ m^{-1}\ K^{-1}$ for basalt, $2.7\ W\ m^{-1}\ K^{-1}$ for gneiss, $2.5\ W\ m^{-1}\ K^{-1}$ for granite, $2.1\ W\ m^{-1}\ K^{-1}$ for sandstone, $1.8\ W\ m^{-1}\ K^{-1}$ for limestone, and $1.6\ W\ m^{-1}\ K^{-1}$ for shale, emphasizing that rock plus water combinations remain far from highly conductive states (**5**).

Within this context, any enhancement of the working fluid conductivity directly affects the effective composite conductivity of the fracture system. Laboratory validation of the GEIOS nitrogen hybrid gas nanofoam demonstrates a markedly different performance regime.

In a custom high pressure and high temperature chamber fabricated from Inconel 718 and operated between 80 and $140\ MPa$ and up to $240\ ^{\circ}C$, bulk thermal conductivity of the nanofoam was measured at approximately $30\ W\ m^{-1}\ K^{-1}$ using a transient hot wire method adapted to the test geometry (**23**,**24**).

This value corresponds to a 166 to $336\ \%$ improvement relative to conventional geothermal materials and is achieved with a nitrogen gas matrix comprising about $95\ \%$ of the fluid volume and embedded Al_2O_3 nanoparticles at 0.6 to $0.8\ \%$ by volume together with silica nanoparticles at 0.3 to $0.5\ \%$ by volume (**23**).

Thermal simulations attribute the high conductivity primarily to the Al_2O_3 phase, whose intrinsic conductivity is on the order of $30\ W\ m^{-1}\ K^{-1}$, and report that the resulting composite nanofoam increases heat extraction efficiency by about 25 to $30\ \%$ relative to water or oil based fluids under comparable pressure and temperature conditions (**5**).

These thermal property gains are sustained under demanding operating envelopes. Testing between March and November 2024 at 80 to $140\ MPa$ and up to $240\ ^{\circ}C$ showed that the nanofoam maintained fracture apertures of $3\ mm$ with only $12\ \%$ degradation over 15 weeks while preserving conductivity near $30\ W\ m^{-1}\ K^{-1}$. Performance retention exceeded $94\ \%$ after 1000 h of operation, and pressure tolerance of $\pm 5\ MPa$ was documented without detectable loss of thermal performance in the laboratory apparatus (**23**,**24**).

Simulations extending beyond the laboratory time window project that under pressures of 80 to $140\ MPa$ and temperatures of 70 to $300\ ^{\circ}C$, nanofoam can sustain fracture apertures of $3\ mm$ or greater for more than 15 years while delivering a 25 to $30\ \%$ increase in heat extraction efficiency compared with water or oil based systems, reinforcing the experimental findings. Comparative analyses quantify how these conductive properties translate into system level advantages. In simulations spanning shale, limestone, and granite, nitrogen nanofoam with Al_2O_3 nanoparticles improves effective formation conductivities substantially above the rock specific baselines of 1.6

to $2.8\ W\ m^{-1}\ K^{-1}$, with associated energy extraction efficiency gains of 25 to $30\ \%$ relative to conventional fluids (**5**).

For the GEIOS configuration, the measured nanofoam conductivity near $30\ W\ m^{-1}\ K^{-1}$ underpins reported energy extraction improvements of 166 to $336\ \%$ at the laboratory scale, when compared against conventional materials characterized by sub $1.0\ W\ m^{-1}\ K^{-1}$ conductivities (**23**,**24**). T

hese enhancements are achieved while the system maintains stable pressure and temperature profiles through real time monitoring and dynamic adjustment of injection rates and nanoparticle spacing, which helps limit thermal losses and fracture instability (**24**).

Anisotropic conduction measurements in related SPARC treated materials corroborate the feasibility of such high conductivities along engineered pathways. Polar plots of thermal conductivity in SPARC samples reveal ellipsoidal distributions characteristic of transversely isotropic media, with conductivities along the corridor axis consistently reaching about $30\ W\ m^{-1}\ K^{-1}$ and decreasing with angle away from that axis (**15**).

These SPARC data, obtained independently from the GEIOS nanofoam work, provide a materials level analogue for nanoparticle mediated, corridor aligned heat transport and support the interpretation that the nanofoam geocasing architecture harnesses similar conduction mechanisms. Taken together, the experimental and simulation results indicate that nitrogen hybrid gas nanofoam delivers a step change in thermal conductivity performance relative to conventional water based EGS fluids and rock only conduction, thereby enabling conduction dominated heat extraction along engineered nanoparticle pathways rather than relying on low conductivity convective cooling. At the same time, all conductivity and efficiency gains reported to date are derived from core scale laboratory tests and numerical models; confirmation that comparable enhancements are realized under reservoir conditions will require field scale deployment with integrated thermal and microseismic monitoring (**23**,**24**,**5**,**15**).

6.1.5 Water usage implications

Water demand differs fundamentally between nitrogen hybrid gas nanofoam operation and conventional water-based stimulation. Table 16 summarises the principal contrasts across thermal transport, fracture longevity, reinjection frequency, and environmental impact.

Conventional enhanced geothermal practice circulates water-based working fluids with bulk thermal conductivities below 1.0 W m^{-1} K^{-1}, requiring large injection volumes to extract heat through convective cooling of the rock matrix (23,5). Proppant degradation compounds this water intensity: ceramic and sand proppants generate approximately 6% and up to 51% fines, respectively, with 75–98% porosity reductions and conductivity losses approaching 99% under high stress, shortening effective fracture lifetimes to 5–7 years and requiring reinjection every 3–5 years (5).

Nitrogen hybrid gas nanofoam replaces the bulk of circulating water with a gas-dominant medium comprising approximately 95% N_2 by volume, doped with 0.6–0.8 vol% Al_2O_3 and 0.3–0.5 vol% silica nanoparticles (8). Under simulated geothermal conditions (240 °C, 140 MPa), this configuration attains a bulk thermal conductivity of ~30 W m^{-1} K^{-1}, a 166–336% enhancement over conventional materials (8,23). Because heat extraction is dominated by conduction along nanoparticle networks rather than by bulk convective cooling, the system intrinsically reduces water throughput requirements. Fracture apertures of ≥3 mm are maintained for more than 15 years at 80–140 MPa and 70–300 °C, with projected reinjection intervals of 10–15 years—roughly three to five times longer than conventional completions (5).

Environmental impact assessments reinforce this contrast. GEIOS nanofoam achieves material recovery >98%, degradation times shorter than 30 days, a biodegradation index of 0.94, and an ecological impact factor below 0.1, indicating rapid breakdown into non-persistent, non-toxic products (23,24). Conventional proppant systems carry residual chemical risk and higher overall environmental impact, although detailed aqueous contaminant budgets have not been reported (5).

Within hybrid Engineered Geothermal Hydrogen Systems built on the SPARC framework, closed-circulation configurations further reduce water consumption by limiting fluid exchange with the surrounding formation, enabling hydrogen co-production via wall–rock reactions while minimising water loss.

When nanofoam is co-injected in such systems, aligned thermal pathways (~30.5 W m^{-1} K^{-1}) can improve heat extraction efficiency by 50–150% relative to conventional stimulation, further decoupling thermal output from water throughput (16).

All quantitative results derive from core-scale experiments and simulations; field-measured water balances and long-term tracer studies are not yet available. Verification of actual water savings requires field-scale deployments with integrated monitoring of water injection, production, and loss, alongside microseismic and geochemical observations (23,24,5,16).

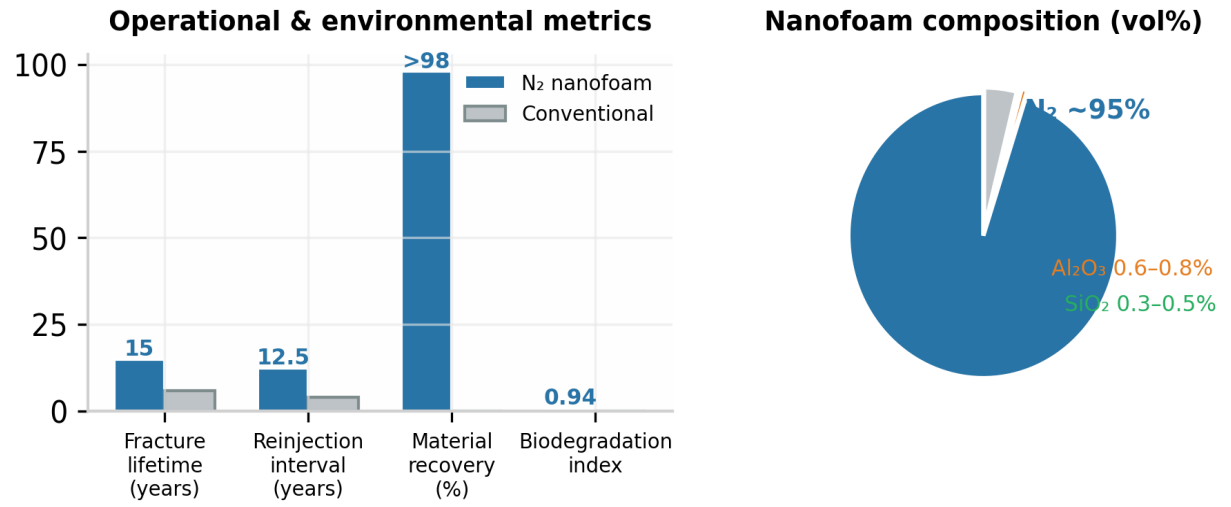

Figure 8. *Operational and environmental metrics comparison (left) and nanofoam volumetric composition (right), highlighting the >98% material recovery, 0.94 biodegradation index, and 95% nitrogen carrier fraction.*

Table 16. Comparative summary of water usage drivers for nitrogen hybrid gas nanofoam versus conventional water–proppant EGS stimulation.

Parameter	Conventional water–proppant EGS	GEIOS N_2 hybrid gas nanofoam	Refs
Working fluid composition	Water + ceramic/sand proppant	~95 vol% N_2 + Al_2O_3 (0.6–0.8 vol%) + SiO_2 (0.3–0.5 vol%)	(5,8)

Bulk thermal conductivity (W m^{-1} K^{-1})	<1.0	~30	(5,8,23)
Thermal conductivity enhancement	Baseline	+166 to +336% vs. conventional materials	(8,23)
Heat extraction mechanism	Convective cooling (large water volumes)	Conduction along nanoparticle networks (minimal water)	(5,23)
Fines generation	~6% (ceramic); up to 51% (sand)	None (no granular proppant)	(5)
Pack porosity reduction	75–98%	N/A	(5)
Fracture conductivity loss	Up to 99%	<5% aperture degradation over test programme	(5,23,24)
Effective fracture lifetime (years)	5–7	>15	(5)
Reinjection interval (years)	3–5	10–15	(5)
Stimulation campaigns per 30-year horizon[a]	6–10	2–3	(5)
Material recovery potential	Not reported	>98%	(23,24)
Degradation time	Not reported	<30 days	(23,24)
Biodegradation index	Not reported	0.94	(23,24)
Ecological impact factor	Elevated (chemical residue risk)	<0.1	(5,23,24)
Heat extraction efficiency gain with SPARC co-injection	Baseline	+50 to +150%	(16)
Validation status	Field + laboratory	Laboratory and simulation only	(23,24,5,16)

[a] Estimated from reinjection interval data over a 30-year project horizon.

6.2 Advantages and Remaining Limitations

6.2.1 Risk reduction achievements

Multiple coupled mechanisms relevant to induced seismicity are substantially attenuated under nitrogen hybrid gas nanofoam operation compared with conventional water-based stimulation. Tables 167 and 3 consolidate the principal risk-control parameters and formation-specific seismic sensitivity metrics, respectively.

Probabilistic pressure control. Injection pressure is treated as a probabilistic variable across a 1,200–2,000 psi operational band rather than as a fixed high overpressure. The 5th, 50th, and 95th percentile quantiles of 1,314.0, 1,603.7, and 1,901.2 psi define an adaptive envelope within which nitrogen injection rates and nanoparticle composition are dynamically adjusted to maintain fracture stability and thermal efficiency (23,24). Sensitivity studies identify a stress gradient of 0.72 psi ft^{-1} as the upper bound for acceptable risk; gradients above 0.77 psi ft^{-1} correspond to

potentially unacceptable risk even when other parameters remain favourable. Within the acceptable envelope, the nanofoam sustains 3 mm fracture apertures with only 12% degradation over extended testing and retains >94% performance after 1,000 h, confirming that repeated high-pressure cycling does not precipitate rapid mechanical collapse (24).

Conduction-dominated thermal extraction. A second, independent risk-reduction pathway arises from the avoidance of bulk thermo-elastic stressing. The nanofoam attains a bulk thermal conductivity of ~30 W m^{-1} K^{-1} (166–336% above conventional materials), stable at 80–140 MPa and up to 240 °C. Heat is transported along Al_2O_3 nanoparticle-mediated conductive pathways rather than by convective cooling of the broader rock mass, minimising large-scale temperature contrasts and the thermo-elastic stress concentrations that can drive fracture instability. SPARC corridor measurements confirm aligned conductivities of ~30 W m^{-1} K^{-1} with an ellipsoidal, transversely isotropic distribution, reinforcing this conduction-based extraction mode (15,23,24).

Formation-specific seismic sensitivity. Risk indicators are not uniform across lithologies. Table 17 and Table 18 reports formation-dependent permeabilities, operational pressure ranges, fracture stability indices, film strengths, and seismic sensitivity factors for granite, basalt, and limestone. Granite exhibits the lowest seismic sensitivity (0.3) and highest fracture stability index (92), whereas limestone presents the highest sensitivity (0.6) and lowest stability index (88). These parameters feed a combined seismic risk matrix and formation stability index that allow injection protocols to be tuned lithology by lithology, maintaining operation within low-risk sectors (23,24).

System-level outcomes. The integrated nanofoam–geocasing configuration delivers maintenance intervals exceeding 10 years, minimal aperture degradation, and stable pressure–temperature profiles, collectively reducing operational intervention frequency relative to conventional systems. Environmental impact is further mitigated by the stable fracture behaviour and efficient heat transfer that minimise uncontrolled seismic activity (23,24).

Limitations. All current results are obtained in high-pressure, high-temperature chambers and through probabilistic modelling; they cannot reproduce reservoir-scale fault slip or the structural complexity of natural fault systems. Continuous field-scale microseismic monitoring integrated with real-time seismic mapping and operational data is therefore designated as essential for validating that these laboratory-derived risk reductions translate into measurably lower induced seismicity under actual reservoir conditions (23,24,16).

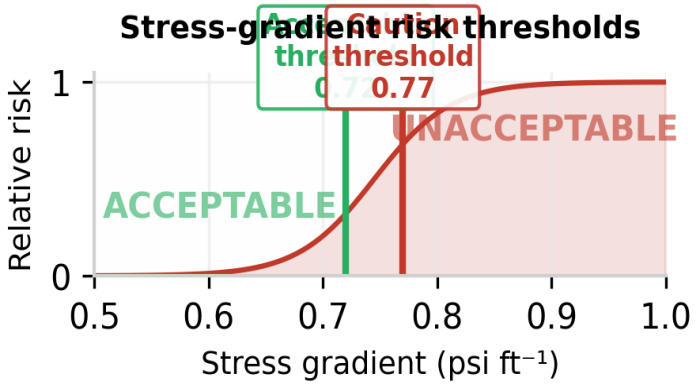

Figure 9. *Stress-gradient risk thresholds separating acceptable operation (< 0.72 psi ft $^{-1}$) from regimes requiring enhanced caution (> 0.77 psi ft $^{-1}$), with the sigmoid-like risk transition curve.*

Table 17. Key risk-control parameters for the GEIOS nitrogen hybrid gas nanofoam system versus conventional water–proppant EGS.

Parameter	Conventional water–proppant EGS	GEIOS N_2 hybrid gas nanofoam	Refs
Injection pressure management	Fixed high overpressure	Probabilistic band: 1,200–2,000 psi (P_5 = 1,314; P_{50} = 1,604; P_{95} = 1,901 psi)	(23,24)
Stress gradient — acceptable threshold (psi ft^{-1})	Not explicitly defined	<0.72	(24)
Stress gradient — unacceptable threshold (psi ft^{-1})	Not explicitly defined	>0.77	(24)
Fracture aperture maintained	Progressive closure (5–7 yr)	3 mm; 12% degradation over test programme	(5,24)
Performance retention after 1,000 h	Not reported	>94%	(24)
Bulk thermal conductivity (W m^{-1} K^{-1})	<1.0	~30	(5,23)
Thermal conductivity enhancement	Baseline	+166 to +336%	(8,23)
Heat extraction mechanism	Convective cooling → thermo-elastic stress concentrations	Nanoparticle-mediated conduction → minimised temperature contrasts	(5,15,23)
SPARC corridor conductivity (W m^{-1} K^{-1})	N/A	~30 (ellipsoidal, transversely isotropic)	(15)
Projected maintenance interval (years)	Reinjection every 3–5	>10	(5,24)
Pressure redistribution behaviour	Heterogeneous (incompressible water + compacted proppant)	Uniform (compressible gas matrix, no granular skeleton)	(5,23)
Validation status	Field + laboratory	Laboratory and simulation only	(23,24,16)

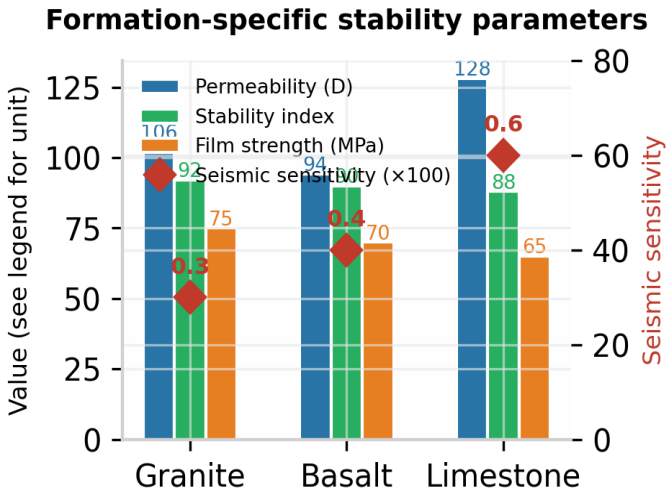

Figure 10. *Formation-specific stability parameters for granite, basalt, and limestone, showing permeability, fracture stability index, film strength, and seismic sensitivity factor (right axis, ×100).*

Table 18. Formation-specific seismic sensitivity and stability parameters under GEIOS nanofoam operation.

Parameter	Granite	Basalt	Limestone	Refs
Permeability (D)	105.6	94.3	128.1	(23,24)
Operational pressure range (MPa)	120–130	110–125	80–110	(23,24)
Fracture stability index	92	90	88	(23,24)
Film strength (MPa)	75	70	65	(23,24)
Seismic sensitivity factor	0.3	0.4	0.6	(23,24)
Relative seismic risk ranking	Lowest	Intermediate	Highest	(23,24)

6.2.2 Constraints from laboratory scale

Laboratory validation of the GEIOS nitrogen hybrid gas nanofoam system rests on core scale experiments in custom high pressure, high temperature chambers and therefore cannot directly represent reservoir scale behaviour or fault slip. Testing of nanofoam performance was conducted in an Inconel 718 chamber between 80 and $140\ MPa$ and up to $240\ ^{\circ}C$, over 15 weeks, yielding sustained $3\ mm$ fracture apertures with only $12\ \%$ degradation and performance degradation described by $D(n) = D_0 + kn$ with $k < 0.006\ \%$ per cycle and overall retention above $94\ \%$ after $1000\ h$ (**24**,**23**).

While these conditions match targeted geothermal pressures and temperatures, they involve centimetre scale cores and cannot reproduce kilometre scale stress heterogeneity or complex natural fault networks. Acoustic emission analyses used an eight sensor array covering 100 to $900\ kHz$ with $40\ dB$ preamplification and $5\ MHz$ digitization, enabling precise characterization of microcrack events during SPARC and related experiments. SPARC treated samples showed 52.0 events versus 102.0 in controls, with $59\ \%$ lower average energy, $42\ \%$ shorter duration, $51\ \%$

fewer counts, and an $83\ \%$ increase in characteristic frequency, indicating more numerous, lower energy micro failures under corridor style conditions (**16**).

However, these AE catalogues reflect small sample volumes under controlled loading and do not capture rupture dynamics of large faults or long range wave propagation effects that govern felt seismicity. Thermal transport characterization likewise relies on laboratory scale proxies. Nanofoam bulk thermal conductivity of approximately $30\ W\ m^{-1}\ K^{-1}$ was measured by a modified transient hot wire method in the Inconel 718 chamber, corresponding to a 166 to $336\ \%$ improvement over conventional materials and remaining stable across 80 to $140\ MPa$ and up to $240\ ^{\circ}C$ (**23**,**24**).

In parallel SPARC work, polar measurements in supracrystalline samples demonstrated ellipsoidal conductivity distributions with $\sim 30\ W\ m^{-1}\ K^{-1}$ along the corridor axis, while Brillouin spectroscopy in 180° backscattering geometry constrained phonon velocities and mean free paths through $\ell = 3\kappa/(C_v v)$ (**15**).

These data substantiate conduction dominated pathways at core scale but do not directly specify how temperature fields evolve over reservoir dimensions or under long term production. Risk characterization for the nanofoam system is built from parameter probability density functions that integrate laboratory validation, injection simulations, well logs, in situ measurements, and real time seismic mapping.

Injection pressure is treated as a probabilistic variable over 1200 to $2000\ psi$, with quantiles at 1314.0, 1603.7, and $1901.2\ psi$, while an 80 to $140\ MPa$ range captures reservoir variability; broader uncertainty ranges are employed where data are sparse, such as 40 to $70\ nm$ particle spacing. This framework ensures conservative modelling but remains conditioned by the underlying laboratory scale datasets and assumptions about scaling of pore pressure and stress consistency. Formation specific stability indices and seismic sensitivity factors provide another example of scale dependent constraint. Reported parameters for granite, basalt, and limestone include permeabilities, pressure ranges, fracture stability indices, film strengths, and seismic sensitivities that are combined into a seismic risk matrix and formation stability index (**23**,**24**).

These quantities are calibrated using core tests and models; they do not yet rest on dense field microseismic catalogues across formations and thus should be regarded as preliminary indicators of relative, not absolute, seismic response. Finally, both SPARC and GEIOS studies state that high pressure, high temperature chambers and associated acoustic measurements cannot reproduce reservoir scale fault slip or the full complexity of natural fault networks (**23**,**24**,**16**).

Consequently, any inference that nanofoam operation reduces induced seismicity drivers is constrained by laboratory scale conditions, limited observation windows, and controlled loading paths. Field scale deployment with continuous microseismic monitoring, distributed temperature sensing, and long term pressure surveillance is explicitly identified as necessary to validate laboratory derived risk reductions, refine formation specific stability indices, and update seismic sensitivity factors under actual reservoir conditions (**15**,**16**,**23**,**24**).

7 Discussion

7.1 Integration of Mechanistic Insights

7.1.1 Linking laboratory data to seismic risk pathways

Linking the nanofoam test programme to induced seismicity pathways hinges on how the laboratory observables map onto pore pressure, thermo elastic, and structural mechanisms. Injection pressure in the GEIOS system is treated probabilistically between 1200 and $2000\ psi$, with $5\ \%$, $50\ \%$, and $95\ \%$ quantiles at 1314.0, 1603.7, and $1901.2\ psi$, corresponding to an 80 to $140\ MPa$ injection range in the Inconel 718 chamber (**23**,**24**).

Within this interval, stepwise sweeps and long term cycling show that a $3\ mm$ fracture aperture experiences only $12\ \%$ degradation over 15 weeks, following a linear law $D(n) = D_0 + kn$ with $k < 0.006\ \%$ per cycle and $> 94\ \%$ performance retention after $1000\ h$ (**24**).

(See Section 4.1.2 and Table 14 for detailed AE event data.)

When the same instrumentation is applied during nanofoam pressure sweeps, these SPARC metrics define a lower energy, micro failure dominated reference regime against which nitrogen driven AE activity as a function of pressure can be plotted and compared (**23**,**24**,**16**).

Thermal conduction measurements anchor interpretation of thermo elastic pathways. In the GEIOS validation, nanofoam exhibits bulk thermal conductivity near $30\ W\ m^{-1}\ K^{-1}$ at 80 to $140\ MPa$ and up to $240\ ^{\circ}C$, measured by a modified transient hot wire method, corresponding to a 166 to $336\ \%$ enhancement over conventional fluids with $< 1.0\ W\ m^{-1}\ K^{-1}$ (**23**,**5**,**24**).

Independently, SPARC polar measurements show an ellipsoidal conductivity distribution with $\sim 30\ W\ m^{-1}\ K^{-1}$ along corridor axes, significantly exceeding isotropic values assigned to untreated or water fractured controls (**15**).

Together, these results support an "avoidance of bulk thermo elastic stressing" interpretation in which heat primarily follows nanoparticle mediated conduction pathways rather than large volume convective cooling that would create strong temperature and strain gradients. Formation specific performance tables further tie laboratory and modelling results to lithology dependent seismic susceptibility. For granite, basalt, and limestone, reported parameters include permeabilities of 105.6, 94.3, and $128.1\ D$, pressure ranges of 120 to 130, 110 to 125, and 80 to $110\ MPa$, fracture stability indices of 92, 90, and 88, film strengths of 75, 70, and $65\ MPa$, and seismic sensitivities of 0.3, 0.4, and 0.6 (**23**).

These values feed into a seismic risk matrix and formation stability index, which translate pressure, stress gradient, and conduction driven fracture support into formation specific likelihood and severity categories for induced events.

Uncertainty assessment formalizes the mapping from laboratory parameters to seismic risk pathways. Injection pressure is represented by probability density functions spanning 80 to $140\ MPa$ (or 1200 to $2000\ psi$), and broader ranges are assigned where data are sparse, such as 40 to $70\ nm$ particle spacing (**24**,**23**).

Pore pressure and stress consistency are evaluated iteratively to remain compatible with fracture stability and tectonic constraints, while stress gradients below $0.72\ psi\ ft^{-1}$ are associated with acceptable risk and those above $0.77\ psi\ ft^{-1}$ with potentially unacceptable conditions (**24**).

In this framework, AE energy reductions, limited aperture degradation, and high thermal conductivity become quantitative inputs to risk pathways, rather than qualitative descriptors. Despite this structured linkage, all underlying measurements are obtained on centimetre scale cores in high pressure, high temperature chambers, and research explicitly acknowledges that such setups cannot reproduce reservoir scale fault slip or the complexity of natural fault networks (**23**,**24**,**16**).

Consequently, the laboratory data define mechanistic trends and parameter spaces consistent with reduced, but not eliminated, seismic drivers; field scale microseismic monitoring and pressure temperature logging remain indispensable to validate these inferred risk reductions and to recalibrate formation specific stability indices under operational reservoir conditions (**15**,**16**,**23**,**24**).

7.1.2 Relative contributions of each mechanism

Disentangling the relative roles of pore pressure, thermo elastic stressing, and proppant induced stress concentration requires comparing the nanofoam results with conventional water proppant benchmarks across common metrics. Pore pressure related effects are constrained by the injection pressure uncertainty space and associated degradation behaviour. In the GEIOS programme, injection pressure is treated probabilistically between 1200 and $2000\ psi$, with $5\ \%$, $50\ \%$, and $95\ \%$ quantiles at 1314.0, 1603.7, and $1901.2\ psi$ that map onto an 80 to $140\ MPa$ operating band (**23**,**24**).

Within this range, stepwise sweeps in the Inconel 718 chamber show that a $3\ mm$ fracture aperture experiences only $12\ \%$ degradation over 15 weeks, described by $D(n) = D_0 + kn$ with $k < 0.006\ \%$ per cycle and total performance retention above $94\ \%$ after 1000 h (**24**).

These results indicate that, under transient pressure perturbations in the specified band, pore pressure driven damage accumulates slowly. In contrast, laboratory studies of granular proppants under high stress report fines generation of $6\ \%$ for ceramic and up to $51\ \%$ for frac sand, porosity reductions of 75 to $98\ \%$, and fracture conductivity losses approaching $99\ \%$, consistent with sustained overpressured compaction and severe loss of transmissivity. Relative to this behaviour, pore pressure mechanisms contribute markedly less to degradation in the nanofoam configuration, provided operation remains within the quantified pressure and stress gradient thresholds.

Thermo elastic mechanisms are primarily reflected in thermal conductivity and associated strain responses. Conventional water based systems rely on fluids with conductivities below $1.0\ W\,m^{-1}\,K^{-1}$ circulating through rocks with baseline values between 1.6 and $2.8\ W\,m^{-1}\,K^{-1}$, promoting convective cooling of large rock volumes (**5**).

Under such conditions, cooling induced contraction and heterogeneous temperature fields are expected to generate significant thermo elastic stresses.

By comparison, the nanofoam attains a bulk thermal conductivity of about $30\ W\,m^{-1}\,K^{-1}$ at 80 to $140\ MPa$ and up to $240\ ^{\circ}C$, as measured by a modified transient hot wire method with uncertainty near $\pm 0.5\ W\,m^{-1}\,K^{-1}$, and maintains this value over the 15 week programme (**23**,**24**).

Independently, SPARC corridors exhibit $\sim 30\ W\,m^{-1}\,K^{-1}$ along the corridor axis with an ellipsoidal distribution characteristic of transversely isotropic media (**15**).

These conduction pathways confine heat transport to nanoparticle and supracrystalline networks rather than driving bulk convective cooling, supporting the interpretation of avoidance of bulk thermo elastic stressing under nanofoam and SPARC style operation.

Proppant induced stress concentration constitutes a third mechanism that is largely absent from the nanofoam system. Conventional water proppant stimulation introduces a granular skeleton that, under geothermal stresses, crushes and compacts, producing fines and dense, stiff clusters that focus stresses and block flow. The documented 75 to $98\ \%$ porosity loss and conductivity reductions up to $99\ \%$ exemplify how strongly this mechanism degrades fracture performance (**5**).

Nitrogen nanofoam does not introduce such a skeleton; instead, a nitrogen rich gas matrix containing 0.6 to $0.8\ \%$ Al_2O_3 and 0.3 to $0.5\ \%$ silica by volume maintains fracture apertures of $3\ mm$ or greater through gas phase pressure support and nanoparticle reinforced structure, operating effectively between 80 and $140\ MPa$ and at temperatures up to at least $240\ ^\circ C$ in the validation chamber and beyond $300\ ^\circ C$ in descriptions (**5**,**23**,**24**).

Formation interface tests under these conditions show adhesion strength of $2.8\ MPa$, formation damage factor below 0.15, and preservation of more than $92\ \%$ permeability and over $95\ \%$ porosity, indicating minimal creation of stiff, damage prone zones at the fracture wall (**24**).

Consequently, stress concentration associated with grain wedging and crushing appears strongly reduced in the nanofoam regime relative to conventional proppant systems. Acoustic emission metrics integrate the combined influence of these mechanisms on microseismic behaviour. SPARC treated cores, which share conduction dominated, non proppant characteristics with the nanofoam configuration, exhibit 52.0 total AE events versus 102.0 in controls, a $59\ \%$ reduction in average energy (from 5.73 to $2.34\ aJ$), a $42\ \%$ reduction in duration, a $51\ \%$ reduction in counts, and an $83\ \%$ increase in characteristic frequency (**16**).

Failure phase events drop from 85.0 to 38.0, and fracture apertures retain $88.0\ \%$ of their opening after 60 days compared with only $8.0\ \%$ in controls (**15**,**16**).

These reductions in event rate and energy, together with enhanced aperture stability, suggest that under conduction oriented, non proppant conditions, the aggregate contribution of pore pressure, thermo elastic, and stress concentration mechanisms to microseismicity is substantially lower than in water proppant analogues. Research on GEIOS explicitly notes that all such conclusions are derived from centimetre scale experiments in high pressure, high temperature chambers and probabilistic modelling and cannot reproduce reservoir scale fault slip or natural fault complexity. Field scale microseismic monitoring and pressure temperature logging during nanofoam deployment are therefore necessary to quantify how these relative mechanistic contributions manifest in operational reservoirs and to refine formation specific stability indices and seismic sensitivities accordingly (**23**,**24**,**16**,**15**).

7.2 Implications for Geothermal Energy Deployment

7.2.1 Potential for reduced seismic risk in field

Evidence from the GEIOS validation and SPARC studies points to a credible potential for reduced induced seismic risk in field deployment, provided that the identified operating envelopes and monitoring approaches are respected. Sensitivity analyses for the nanofoam configuration define an injection pressure uncertainty range of 1200 to $2000\ psi$, with $5\ \%$, $50\ \%$, and $95\ \%$ quantiles at 1314.0, 1603.7, and $1901.2\ psi$, respectively, mapped to 80 to $140\ MPa$ in the high pressure chamber. Within this space, maintaining a stress gradient below $0.72\ psi\ ft^{-1}$ is associated with

acceptable risk, whereas gradients above $0.77\ psi\ ft^{-1}$ may correspond to unacceptable risk, even if other parameters are favorable.

These thresholds, combined with laboratory observations of only $12\ \%$ fracture aperture degradation and $> 94\ \%$ performance retention after $1000\ h$ of cycling, suggest that, under analogous pressure control in the field, pore pressure related drivers of induced seismicity could be substantially reduced relative to conventional water-based operations (**23**,**24**).

Laboratory micro seismic proxies support this interpretation. SPARC experiments, which share conduction dominated, non-proppant characteristics with the nanofoam system, register 52.0 acoustic events compared with 102.0 in water fractured controls, together with $59\ \%$ lower average event energy, $42\ \%$ shorter duration, $51\ \%$ fewer counts, and an $83\ \%$ increase in characteristic frequency. The largest reduction occurs in the failure phase, where events decrease from 85.0 to 38.0, and SPARC treated fractures retain $88.0\ \%$ of their aperture after 60 days, versus $8.0\ \%$ for controls. These findings indicate a shift toward more frequent, low energy micro failures and away from large, high-energy events under conduction-oriented conditions that resemble nanofoam operation, implying a lower microseismic energy budget if similar mechanisms operate at reservoir scale (**15**,**16**).

Thermal transport characteristics further strengthen the case for attenuated thermo elastic contributions to seismic hazard. Nanofoam testing in an Inconel 718 chamber at 80 to $140\ MPa$ and up to $240\ ^{\circ}C$ demonstrates a bulk thermal conductivity of approximately $30\ W\ m^{-1}\ K^{-1}$, corresponding to a 166 to $336\ \%$ enhancement over conventional fluids with conductivities below $1.0\ W\ m^{-1}\ K^{-1}$. Independently, SPARC corridors exhibit similar axial conductivities of about $30\ W\ m^{-1}\ K^{-1}$ with ellipsoidal polar distributions characteristic of transversely isotropic media. Together, these measurements support an avoidance of bulk thermo elastic stressing in which heat is transported along engineered nanoparticle and supracrystalline pathways rather than by convective cooling of large rock volumes, a configuration expected to reduce thermal stress gradients that can contribute to fracture instability (**15**,**23**,**24**,**5**).

Formation specific risk mapping provides a framework for translating these laboratory mechanisms into field relevant decision tools. For granite, basalt, and limestone, reported permeabilities, pressure ranges, fracture stability indices, film strengths, and seismic sensitivity factors (0.3, 0.4, and 0.6, respectively) are combined into a seismic risk matrix and formation stability index. This construct links controllable variables such as injection pressure and stress gradient to lithology dependent likelihood and severity of induced events under nanofoam operation and thus can guide field injection protocols toward lower risk regions of parameter space, particularly in formations with low seismic sensitivity and high stability indices (**23**,**24**).

Despite these indications of risk reduction potential, all supporting data derive from centimetre scale cores in high pressure, high temperature chambers and from probabilistic modelling. Research on GEIOS and SPARC explicitly states that such laboratory configurations cannot reproduce reservoir scale fault slip or the structural complexity of natural fault networks. Consequently, any expectation of reduced induced seismicity in the field must be treated as provisional.

Field scale deployments of the nanofoam system will require continuous microseismic monitoring, together with distributed temperature sensing, pressure logging, and gas composition analysis, to verify that observed event rates, energy releases, and thermal responses fall within or below the ranges inferred from laboratory experiments and uncertainty analyses. Only through such integrated field observations can the formation specific stability indices and seismic sensitivity

factors be recalibrated and the actual magnitude of seismic risk reduction under reservoir conditions be rigorously established (**15**,**16**,**23**,**24**).

7.2.2 Scalability considerations

Scaling the nitrogen hybrid gas nanofoam configuration from core experiments to reservoir implementation requires assessing which demonstrated behaviours are likely to persist as system dimensions, well count, and operational timeframes increase.

Laboratory validation between March and November 2024 established stable performance at injection pressures of 80 to $140\ MPa$ and temperatures up to $240\ ^{\circ}C$, with fracture apertures of $3\ mm$ degrading by only $12\ \%$ over 15 weeks and an overall performance retention above $94\ \%$ after $1000\ h$, described by $D(n) = D_0 + kn$ with $k < 0.006\ \%$ per cycle. The same test series confirmed bulk thermal conductivity near $30\ W\ m^{-1}\ K^{-1}$ and flow regimes with Reynolds numbers above 10^4 and Weber numbers greater than 50, all achieved within an Inconel 718 chamber instrumented for high fidelity pressure and temperature control. These metrics indicate that, at laboratory scale, the nanofoam can operate robustly across the intended pressure and temperature envelope.

Pressure management emerges as a central scalability constraint. Uncertainty analysis defines an operational pressure band of 1200 to $2000\ psi$, with $5\ \%$, $50\ \%$, and $95\ \%$ quantiles at 1314.0, 1603.7, and $1901.2\ psi$, mapped to 80 to $140\ MPa$ for modelling and testing (**23**,**24**).

Sensitivity studies show that maintaining stress gradients below $0.72\ psi\ ft^{-1}$ corresponds to acceptable risk, while gradients above $0.77\ psi\ ft^{-1}$ may imply unacceptable risk even under otherwise favourable conditions (**24**).

At field scale, reproducing this controlled, probabilistic pressure regime will depend on injection infrastructure capable of modulating nitrogen pressures dynamically over many wells, while seismic monitoring verifies that larger stimulated volumes continue to respect these threshold gradients. Thermal conduction properties of the working medium and surrounding materials also impose scale dependent considerations. In the nanofoam chamber, a nitrogen matrix ($\sim 95\ \%$ by volume) carrying 0.6 to $0.8\ \%$ Al_2O_3 and 0.3 to $0.5\ \%$ silica nanoparticles achieves $\sim 30\ W\ m^{-1}\ K^{-1}$ conductivity, representing a 166 to $336\ \%$ enhancement over conventional geothermal fluids with $< 1.0\ W\ m^{-1}\ K^{-1}$ (**23**,**5**).

Independent SPARC measurements show corridor aligned conductivities of approximately $30\ W\ m^{-1}\ K^{-1}$ with an ellipsoidal polar pattern, confirming that engineered supracrystalline structures can sustain such conduction pathways (**15**).

Extrapolating to reservoir scale requires demonstrating that nanoparticle and supracrystalline alignments can be established and maintained over tens to hundreds of metres, rather than centimetres, without loss of the conduction dominated, "avoidance of bulk thermo elastic stressing" regime that underpins the risk reductions.

System readiness indicators from the GEIOS programme explicitly address deployment at larger scales. An implementation readiness index of 0.96 and projected maintenance intervals exceeding 10 years derive from combined laboratory and modelling analyses, including an energy extraction efficiency improvement of 166 to $336\ \%$ relative to conventional methods and a system response time below $1000\ ms$ for adjusting operating parameters (**24**).

These metrics suggest that, given appropriate control and monitoring, the nanofoam configuration is technically mature enough for multi well field pilots, although they remain grounded in chamber

data and simulations rather than long term reservoir operation. Data integration strategies developed for the uncertainty assessment will be essential to scaling. Parameter probability density functions are constructed from reservoir drilling and completion logs, nanofoam validation tests, injection simulations, in situ measurements, and real time seismic mapping, with broader uncertainty ranges (for example 80 to $140\ MPa$ for injection pressure and 40 to $70\ nm$ for particle spacing) applied where field data are sparse (**23**,**24**).

Extending this framework to full fields will require dense microseismic catalogues, distributed temperature sensing, and pressure time series across multiple wells so that formation specific stability indices and seismic sensitivities can be recalibrated beyond core scale constraints. Research on SPARC offers additional guidance for scale up. Modelling indicates that a five spot well pattern could access rock volumes of order $5 \times 10^4\ m^3$ and that field implementation demands comprehensive monitoring including distributed temperature sensing, pressure transducers, gas composition analysis, and microseismic networks (**15**,**16**).

Economic analyses for moderately sized SPARC systems (5 to 10 wells) show that drilling dominates capital expenditure and that continuous monitoring is central to controlling operational risk (**16**,**15**).

These findings, together with the GEIOS laboratory results, underline that although the nanofoam and supracrystalline concepts exhibit strong laboratory performance and favourable readiness metrics, confirmation of scalable seismic risk reduction and thermal efficiency ultimately depends on carefully monitored, multi well pilot deployments under reservoir conditions (**15**,**16**,**23**,**24**).

7.3 Role of Monitoring and Adaptive Control

7.3.1 Importance of real-time microseismic monitoring

Continuous microseismic observation is indispensable for validating the risk reductions inferred from nanofoam laboratory experiments and uncertainty analyses. In the GEIOS framework, injection pressure is explicitly modeled as a probabilistic variable between 1200 and $2000\ psi$ (corresponding to 80 to $140\ MPa$), with $5\ \%$, $50\ \%$, and $95\ \%$ quantiles at 1314.0, 1603.7, and $1901.2\ psi$, respectively (**23**,**24**).

Laboratory tests within this pressure window show only $12\ \%$ degradation of a $3\ mm$ fracture aperture over 15 weeks and overall performance retention above $94\ \%$ after $1000\ h$, captured by the linear degradation law $D(n) = D_0 + kn$ with $k < 0.006\ \%$ per cycle (**24**).

However, these results derive from centimetre scale specimens in high pressure chambers and do not capture the behaviour of natural fault networks; real time microseismic monitoring in the field is therefore required to determine whether pressure excursions near the modeled quantiles remain compatible with acceptable induced seismicity levels (**23**,**24**,**16**).

Acoustic emission experiments on SPARC treated and water fractured controls provide a template for the type of microseismic metrics that should be tracked in situ. Using eight 100 to $900\ kHz$ sensors with $40\ dB$ preamplification and $5\ MHz$ digitization, SPARC cores recorded 52.0 events compared with 102.0 in controls, with average energies of 2.34 and $5.73\ aJ$, amplitudes of 61.86 and $71.04\ dB$, durations of 311.43 and $541.38\ \mu s$, counts of 12.71 and 25.68, and characteristic frequencies of 6.55 and $3.57\ kHz$, respectively (**15**,**16**).

These measurements document a $49\ \%$ reduction in event count and $59\ \%$ reduction in average energy, together with an $83\ \%$ increase in frequency, under corridor style, conduction dominated conditions. Translating such reductions into a reservoir setting requires continuous microseismic

catalogues that resolve event rates, energies, and frequency content during nanofoam injection and compare them against these laboratory benchmarks.

Risk management for GEIOS already integrates seismic information at the modeling stage. Uncertainty assessment consolidates reservoir drilling and completion logs, nanofoam validation tests, injection simulations, in situ measurements, and real time seismic mapping into parameter probability density functions. Stress gradients are treated as primary control variables, with analysis identifying gradients below $0.72\ psi\ ft^{-1}$ as acceptable and those above $0.77\ psi\ ft^{-1}$ as potentially unacceptable even when other parameters are favorable (**23**,**24**).

Without real time microseismic monitoring, it is not possible to verify whether field operations that nominally respect these gradients indeed correspond to lower microseismic energy release, or whether unmodeled heterogeneities produce localized instability. Research on SPARC scale up explicitly specifies microseismic monitoring as a core requirement for field implementation. For moderately sized systems with 5 to 10 wells accessing approximately $5 \times 10^4\ m^3$ of reactive rock, comprehensive monitoring must include distributed temperature sensing, pressure transducers, gas composition analysis, and dedicated microseismic networks to ensure fracture containment and track permeability evolution (**15**,**16**).

These same elements are directly applicable to nanofoam based EGS, where microseismic data will be needed to refine formation specific stability indices and seismic sensitivity factors reported for granite, basalt, and limestone, and to test whether operations remain in low risk sectors of the seismic risk matrix constructed from core scale measurements (**23**,**24**).

Current GEIOS conclusions on reduced induced seismicity drivers are grounded in high pressure, high temperature chamber experiments and probabilistic modeling, both of which explicitly acknowledge their inability to reproduce reservoir scale fault slip or the structural complexity of natural fault systems (**23**,**24**,**16**).

Field scale, real time microseismic monitoring is therefore not ancillary but central: it provides the only direct means to validate that transient pore pressure perturbations, conduction dominated heat extraction, and absence of granular proppant translate into measurably lower seismic activity under operational reservoir conditions, and to update risk thresholds and operating envelopes when discrepancies between modeled and observed behaviour arise (**15**,**16**,**23**,**24**).

7.3.2 Adaptive parameter control strategies

Adaptive control in the GEIOS nitrogen hybrid gas nanofoam configuration is structured around a pressure uncertainty space and associated risk thresholds. Injection pressure is represented by a probability density over 1200 to $2000\ psi$, with $5\ \%$, $50\ \%$, and $95\ \%$ quantiles at 1314.0, 1603.7, and $1901.2\ psi$, respectively, corresponding to an 80 to $140\ MPa$ operating band.

Within this interval, parameter PDFs are constructed from reservoir drilling and completion logs, nanofoam laboratory validation tests, injection simulations, in situ measurements, and real time seismic mapping, and are iteratively refined to ensure pore pressure and stress consistency with tectonic constraints. When datasets are sparse, broader uncertainty ranges such as 80 to $140\ MPa$ for pressure and 40 to $70\ nm$ for particle spacing are deliberately adopted to maintain conservative modelling (**23**,**24**).

Risk oriented adaptation focuses on the stress gradient, which condenses the combined effects of pore pressure and formation properties. Sensitivity analyses identify that maintaining a gradient below $0.72\ psi\ ft^{-1}$ keeps operation within acceptable risk thresholds, whereas gradients above $0.77\ psi\ ft^{-1}$ may correspond to unacceptable risk even when other parameters are favourable.

Control strategies therefore target dynamic adjustment of nitrogen injection pressure and nanoparticle composition to keep gradients inside this narrow window while preserving fracture stability and thermal performance.

In situations where low pressures threaten fracture opening or heat transfer, the framework prescribes incremental increases in nitrogen pressure and optimization of Al_2O_3 and SiO_2 loading; in high pressure scenarios, the capacity of the nanofoam to tolerate variations of $\pm 5\ MPa$ without loss of structural integrity provides the basis for controlled downregulation of injection (**24**,**23**).

Operational protocols for a $200\ MW$ EQG deployment translate these principles into explicit injection and production setpoints. At $4500\ m$ depth, injection pressure is ramped at $2\ MPa\, min^{-1}$ to $80\ MPa$ and then staged into an optimal operating range of 110 to $130\ MPa$. Pulse frequency is tuned continuously between 0.1 and $1.0\ Hz$ based on acoustic imaging of formation response. Production wells at $3000\ m$ modulate drawdown to maintain Reynolds numbers above 1.2×10^4, thereby stabilizing flow while preventing particle settling. For this field scenario, the recommended operating envelope combines 110 to $130\ MPa$ pressure, 220 to $260\ ^\circ C$ temperature, and particle loadings of $0.7\ \%\ Al_2O_3$ and $0.4\ \%\ SiO_2$. Adaptive triggers are defined as thermal conductivity falling below $28\ W\, m^{-1}\, K^{-1}$, pressure variation exceeding $\pm 0.2\ MPa$, or flow stability dropping below $Re = 10^4$, each prompting automated adjustment of injection rate, nanoparticle concentration, or flow distribution (**23**,**24**).

Nanofoam stability and thermal performance are also subject to continuous closed loop control. Laser diffraction monitoring of particle size distribution, together with real time tracking of Al_2O_3 and SiO_2 concentrations, informs dynamic modification of surfactant and stabilizer dosing to prevent agglomeration. Distributed sensor arrays quantify phonon transport efficiency, and thermal conductivity is maintained within a tolerance of $\pm 1.2\ W\, m^{-1}\, K^{-1}$ by modulating nanoparticle concentrations according to spatial conductivity maps. Temperature gradients are constrained to $\pm 2\ ^\circ C\, min^{-1}$ to limit thermal stress accumulation while sustaining conduction dominated heat extraction (**24**,**23**).

Seismic evaluation tools are explicitly embedded in this adaptive architecture. Real time seismic mapping forms one of the primary data streams used in constructing the pressure and stress PDFs and in updating fracture stability and seismic sensitivity parameters for different lithologies. Seismic data, in conjunction with laboratory validation, are used to refine operational boundaries and to recalibrate the thresholds at which changes in injection strategy are required. Research emphasises that, although laboratory AE measurements and chamber based sensitivity analyses indicate reduced microseismic energy release under nanofoam operation, laboratory configurations cannot reproduce reservoir scale fault slip or the complexity of natural fault networks.

Consequently, field scale microseismic monitoring is identified as indispensable for closing the adaptive control loop at reservoir scale, allowing observed event populations to feed back into parameter distributions, stress gradient limits, and mitigation strategies over the project lifetime (**23**,**24**,**16**,**15**).

8 Limitations and Field-Scale Considerations

8.1 Laboratory vs. Field Conditions

8.1.1 Differences in scale and heterogeneity

Core experiments on GEIOS nanofoam and SPARC architectures are conducted in highly controlled Inconel 718 vessels at 80 to $140\ MPa$ and up to $240\ ^{\circ}C$, with pressure stability better than $\pm 0.1\ MPa$ and temperature control within $\pm 1\ ^{\circ}C$.

These conditions approximate reservoir pressures and temperatures but act on centimetre scale samples with relatively homogeneous properties compared with heterogeneous field formations. Sensitivity analyses and uncertainty frameworks therefore rely on parameter probability density functions that intentionally broaden key ranges, for example 80 to $140\ MPa$ for injection pressure and 40 to $70\ nm$ for particle spacing, to account for reservoir scale variability that is not present in the chamber environment (**23**,**24**).

Structural organization of thermal pathways illustrates this scale disparity. SPARC corridors are created within single cores by controlled fracturing and nanoparticle mediated stabilization, producing supracrystalline fabrics where crystallographic preferred orientation, shape preferred orientation, boundary network topology, and hierarchical scaling jointly enhance conductivity along a preferred axis by factors of 1.5 to 2.5 relative to the matrix (**15**,**16**).

Micro to mesoscale models treat a $500 \times 500 \times 50\ nm^3$ domain filled with alumina and silica nanoparticles in chain like configurations and show conductivity above $25\ W\ m^{-1}\ K^{-1}$ for volume fractions as low as 1.0 to $1.5\ \%$ when chains align with heat flow, whereas random arrangements follow modest effective medium trends (**16**).

Field formations, by contrast, exhibit variable mineralogy, fabric, and fracture density over tens to hundreds of metres, and it remains untested whether comparable chain alignment, interparticle spacing of 8 to $12\ nm$, and network connectivity of 85 to $95\ \%$ can be realized and maintained at reservoir scale. Reaction and transport heterogeneity likewise amplify with scale. Integrated SPARC modeling calibrated at core scale reproduces thermal responses with R^2 of 0.96 for SPARC and 0.94 for controls, hydrogen production with R^2 of 0.93 and 0.91, and reaction extent patterns with mean conversion errors of about $7\ \%$ (**16**,**15**).

Figure 9 | SPARC Framework, THM Modelling, and Field-Scale Upscaling

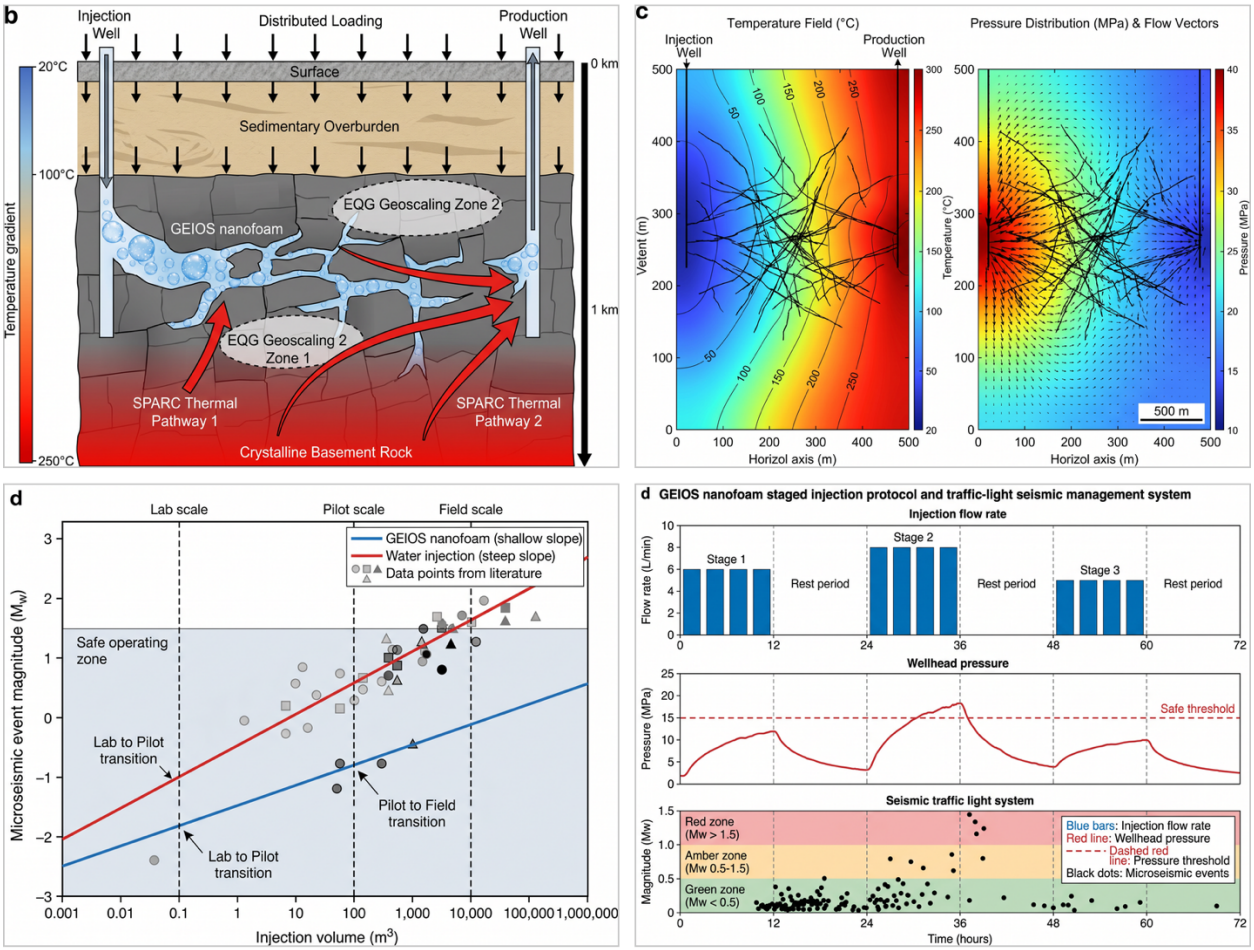

(a) SPARC Thermal Pathway schematic. GEIOS nanofoam (blue bubbles) flows through the fracture network, distributing pressure and heat extraction across multiple EQG geoscaling zones. Red arrows denote SPARC thermal pathways; temperature gradient shown left (blue, 20 °C) to bottom (red, 250 °C).

(b) THM model results for a 500 × 500 m field-scale domain. Left: temperature field (°C) with isothermal contours; right: pressure distribution (MPa) with Darcy flow vectors. Fracture network shown in black.

(c) Scaling diagram (log–log) of maximum microseismic magnitude versus injection volume from laboratory to field scale. GEIOS nanofoam (blue) maintains a shallower slope, remaining within the safe operating zone (Mw < 1.5, shaded) at field-scale volumes.

(d) Staged injection protocol and traffic-light seismic management system. Top: flow-rate schedule; middle: wellhead pressure (safe threshold 15 MPa, dashed); bottom: traffic-light zones with microseismic events (dots).

Forward simulations extended to 100 to $350\ ^{\circ}C$, 50 to $200\ bar$, and 0.01 to $1.0\ ml\ min^{-1}$ flow rates suggest that performance advantages persist across these conditions, but all such validations remain at core scale. When transferred to reservoirs, additional heterogeneities in permeability, pre existing serpentinization, and stress fields will interact with these mechanisms in ways not represented in the laboratory volumes.

Monitoring capabilities differ sharply between settings. In the laboratory, eight wideband acoustic emission sensors spanning 100 to $900\ kHz$, digitized at $5\ MHz$, resolve individual microcrack events with quantified energies in the attojoule range, durations of a few $10^2\ \mu s$, and characteristic frequencies of several kilohertz.

These data allow precise quantification of reductions in total events and average energy under SPARC like, conduction dominated operation. In field scale SPARC implementations, microseismic monitoring is envisaged but necessarily operates at lower frequencies and coarser

spatial resolution, using distributed temperature sensing, pressure transducers, gas composition analysis, and microseismic arrays to track fracture containment and permeability evolution across volumes of order $5 \times 10^4\ m^3$ in five spot configurations (**15**,**16**).

The transition from centimetre to decametre scales thus alters both the accessible observables and the resolution with which heterogeneity in event populations can be detected. Risk frameworks in GEIOS explicitly acknowledge these scale and heterogeneity constraints. Injection pressure is represented by probability distributions over 1200 to $2000\ psi$, with quantiles at 1314.0, 1603.7, and $1901.2\ psi$, and stress gradients are treated as primary control parameters, with thresholds of 0.72 and $0.77\ psi\ ft^{-1}$ separating acceptable from potentially unacceptable domains (**23**,**24**).

Parameter ranges are iteratively refined using laboratory tests and limited field observations, but conservative broadening is maintained where heterogeneity is poorly constrained. Research on both SPARC and GEIOS stresses that high pressure, high temperature chambers cannot reproduce reservoir scale fault slip or natural fault network complexity, and therefore designates comprehensive field monitoring, including microseismic networks, as essential for validating laboratory inferred reductions in thermo elastic stressing and pore pressure driven instability at reservoir scale (**15**,**16**,**23**,**24**).

8.1.2 Need for reservoir-scale validation

Core experiments on GEIOS nanofoam and SPARC architectures establish mechanistic trends under tightly controlled conditions, but they do not yet demonstrate how these behaviours manifest in structurally complex reservoirs. Nanofoam validation used an Inconel 718 vessel operated between 80 and $140\ MPa$ and up to $240\ ^\circ C$, with pressure stability better than $\pm 0.1\ MPa$ and temperature control within $\pm 1\ ^\circ C$, to show that a $3\ mm$ fracture aperture degrades by only $12\ \%$ over 15 weeks, following $D(n) = D_0 + kn$ with $k < 0.006\ \%$ per cycle and performance retention exceeding $94\ \%$ after $1000\ h$ (**23**,**24**).

SPARC and nanofoam studies also report bulk thermal conductivities near $30\ W\ m^{-1}\ K^{-1}$ along engineered pathways, far above conventional fluids, and consistently reduced acoustic emission counts and energies in treated cores relative to water fractured controls (**15**,**16**).

These results strongly support risk reduction at laboratory scale but cannot capture kilometre scale stress heterogeneity, fault connectivity, or long range pore pressure diffusion in natural formations. Uncertainty assessment for the nanofoam system already embeds this limitation by treating key parameters as random variables. Injection pressure is represented over 1200 to $2000\ psi$ (approximately 80 to $140\ MPa$) with $5\ \%$, $50\ \%$, and $95\ \%$ quantiles at 1314.0, 1603.7, and $1901.2\ psi$, and broader uncertainty ranges, for example 80 to $140\ MPa$ for pressure and 40 to $70\ nm$ for particle spacing, are assigned where data are sparse (**23**,**24**).

Stress gradients are used as primary control variables, with gradients below $0.72\ psi\ ft^{-1}$ classified as acceptable and gradients above $0.77\ psi\ ft^{-1}$ associated with potentially unacceptable risk (**24**).

These thresholds and distributions are calibrated with chamber results and limited field constraints; verification that they correctly bound seismic hazard in full reservoirs requires direct observation of induced event populations under operational injection.

Acoustic emission data from SPARC experiments illustrate how much detail is available in the laboratory and why analogous information is needed in situ. With eight 100 to $900\ kHz$ sensors sampled at $5\ MHz$, SPARC treated cores show 52.0 events versus 102.0 in controls, a $59\ \%$

reduction in average energy (from 5.73 to $2.34\ aJ$), $42\ \%$ shorter durations, $51\ \%$ fewer counts, and an $83\ \%$ increase in characteristic frequency, particularly halving failure phase events from 85.0 to 38.0 (**15**,**16**).

In the nanofoam apparatus, the same instrumentation is used during stepwise sweeps between 80 and $140\ MPa$, allowing AE versus pressure relationships to be constructed (**23**,**24**,**16**).

However, these centimetre scale catalogues cannot resolve how microseismicity organizes along meter to kilometre scale faults, nor how b values and energy distributions evolve during multi year injection. Research on SPARC scale up directly stipulates that field implementation demands microseismic networks, combined with distributed temperature sensing, pressure transducers, and gas composition analysis, to track thermal fronts, permeability evolution, and fracture containment in volumes of order $5 \times 10^4\ m^3$ accessed by five spot well patterns (**15**,**16**).

GEIOS uncertainty workflows already integrate real time seismic mapping as a primary data source for parameter probability density functions, but current calibrations rely mainly on laboratory validation and limited in situ information (**23**,**24**).

Systematic reservoir scale microseismic monitoring during nanofoam deployment is therefore essential to: (i) test whether event rates and energies remain below those inferred from chamber AE measurements, (ii) refine formation specific stability indices and seismic sensitivity factors for granite, basalt, and limestone, and (iii) update stress gradient thresholds and pressure quantiles based on observed fault scale behaviour. All cited studies explicitly acknowledge that high pressure, high temperature reactors, even when equipped with advanced AE arrays and multi physics sensing, cannot reproduce reservoir scale fault slip or the geometric complexity of natural fault networks (**15**,**16**,**23**,**24**).

Reservoir scale validation with continuous microseismic monitoring, integrated into the existing probabilistic framework, is thus a necessary step before concluding that the reduced pore pressure perturbations, avoidance of bulk thermo elastic stressing, and elimination of granular proppant observed in the laboratory translate into a substantially reduced induced seismicity risk profile in operational geothermal fields.

8.2 Microseismic Monitoring in Field Applications

8.2.1 Instrumentation strategies

Designing field instrumentation for nanofoam based geothermal projects should build directly on the laboratory sensor architectures already demonstrated for SPARC and GEIOS while accommodating reservoir scale constraints.

Core scale nanofoam validation employed an Inconel 718 chamber operated between 80 and $140\ MPa$ and 70 to $300\ ^\circ C$, instrumented with dual strain gauge and crystal quartz pressure transducers (stability $\pm 0.1\ MPa$, microsecond response) and multi zone heating with fiber optic temperature arrays and infrared imaging for distributed thermal measurements (**23**,**24**).

These elements define the minimum resolution and redundancy that downhole pressure and temperature monitoring should target in order to resolve transient pore pressure perturbations and conduction mode heat extraction at reservoir scale.

Acoustic monitoring in SPARC and related experiments used eight wideband acoustic emission sensors spanning 100 to $900\ kHz$, with $40\ dB$ preamplifiers and $5\ MHz$ digitization, allowing three

dimensional event location from arrival time differences and detailed waveform analysis (energy, duration, counts, frequency) (**15**,**16**).

Event catalogues distinguished SPARC treated from control samples by a $49\ \%$ reduction in total event count and a $59\ \%$ reduction in average energy, together with an $83\ \%$ increase in characteristic frequency, under otherwise identical loading (**16**).

Field microseismic arrays cannot reproduce this frequency band, but the laboratory configuration provides clear guidance: networks should be deployed to capture both event rates and energy release with sufficient temporal resolution to compare nanofoam injection stages against these benchmarks within the probabilistic pressure range of 1200 to $2000\ psi$ used in GEIOS risk assessments (**23**,**24**).

Comprehensive monitoring concepts articulated for SPARC scale up already specify several field instrumentation pillars that are directly transferable. Distributed temperature sensing is identified as essential for tracking thermal front propagation, while pressure transducers are required to monitor permeability evolution, and gas composition analysis is needed to optimize production and detect anomalies in hydrogen and associated species (**15**,**16**).

Microseismic monitoring is highlighted as a core requirement for ensuring fracture containment. In the GEIOS uncertainty framework, these data streams feed parameter probability density functions for injection pressure, pore pressure, and stress, with stress gradient thresholds at 0.72 and $0.77\ psi\ ft^{-1}$ delineating acceptable and potentially unacceptable risk domains (**23**,**24**).

Field instrumentation must therefore be configured not only to detect events but also to update these PDFs in real time. Chemical and electrochemical sensors used in SPARC experiments provide a template for tracking geochemical and redox evolution during reservoir operation. Analytical systems included gas chromatography for H_2 and CH_4, ion chromatography for major cations, inductively coupled plasma mass spectrometry for trace elements, isotope ratio mass spectrometry for δ^2H and $\delta^{13}C$, and high temperature pH and redox electrodes (**15**,**16**).

Detection limits for H_2 and CH_4 were 0.1 and $0.05\ \mu mol\ L^{-1}$, respectively, with relative standard deviations of a few percent (**16**).

Translating this capability to the field implies installing sampling and analysis infrastructure capable of resolving small changes in gas composition and redox state that might correlate with fracture evolution and microseismic activity during nanofoam circulation. The nanofoam validation apparatus itself illustrates how integrated, high rate data acquisition should be structured. More than 50 critical parameters, including pressure, temperature, flow, gas composition, and particle size distribution, were logged at up to $10\ kHz$, with Coriolis flow meters (accuracy $\pm 0.1\ \%$) characterizing Reynolds numbers above 10^4 and laser diffraction systems tracking particle size with nanometre resolution in a class 1000 cleanroom (**23**,**24**).

While reservoir operations cannot match these sampling rates everywhere, central field acquisition systems should emulate the synchronized, multi sensor architecture so that pressure transients, thermal responses, and microseismic signals can be evaluated jointly within the existing probabilistic framework. Importantly, all of these instrumentation strategies have so far been realized only in high pressure, high temperature laboratory reactors and associated SPARC experiments. Studies explicitly state that such reactors, even when equipped with advanced AE arrays and analytical suites, cannot reproduce reservoir scale fault slip or the complexity of natural fault networks (**15**,**16**,**23**,**24**).

Consequently, field microseismic networks, distributed temperature sensing, downhole pressure gauges, and surface analytical systems must be deployed as part of initial nanofoam projects to validate laboratory inferred risk reductions, refine formation specific stability indices and seismic sensitivities, and adjust injection strategies based on observed reservoir scale behaviour.

8.2.2 Data interpretation challenges

Interpreting nanofoam related microseismic and performance data is constrained first by the probabilistic nature of the pressure operating window. Injection pressure is represented as a random variable over 1200 to $2000\ psi$, with $5\ \%$, $50\ \%$, and $95\ \%$ quantiles at 1314.0, 1603.7, and $1901.2\ psi$, mapped to 80 to $140\ MPa$.

Laboratory tests occupy this same range, yet the pressure probability density function itself is derived from a mixture of laboratory validation, in situ measurements, well logs, injection simulations, and real time seismic mapping.

Any inference about how observed acoustic activity or fracture stability at a given chamber pressure extrapolates to field conditions must therefore account for these compounded uncertainties and the deliberate broadening of pressure ranges where data are sparse, for example 80 to $140\ MPa$ and 40 to $70\ nm$ particle spacing (**23**,**24**).

A second difficulty arises from the reliance on high frequency acoustic emission (AE) data at core scale as a proxy for field scale microseismicity. In SPARC experiments, eight 100 to $900\ kHz$ sensors sampled at $5\ MHz$ captured detailed waveforms for each event, enabling quantification of total event counts, energies in the attojoule range, amplitudes, durations, counts, and characteristic frequencies (**15**,**16**).

SPARC treated cores showed 52.0 events versus 102.0 in controls, with $59\ \%$ lower average energy and an $83\ \%$ increase in characteristic frequency (**16**).

These metrics define a clear laboratory contrast but are recorded in a frequency band and at a spatial scale that differ fundamentally from reservoir microseismic monitoring.

Translating reductions in high frequency AE energy and event counts into expectations for kilometre scale fault systems is therefore non trivial and requires caution when using AE statistics to populate seismic risk matrices or to calibrate formation specific seismic sensitivities (**15**,**16**,**23**,**24**).

Thermal conduction measurements provide another example where interpretation is strongly scale dependent. Nanofoam tests in the Inconel 718 chamber report bulk thermal conductivity near $30\ W\,m^{-1}\,K^{-1}$ with an uncertainty of about $\pm 0.5\ W\,m^{-1}\,K^{-1}$ at 80 to $140\ MPa$ and up to $240\ ^{\circ}C$ (**23**,**24**).

Independent SPARC polar measurements identify an ellipsoidal conductivity distribution with values around $30\ W\,m^{-1}\,K^{-1}$ along corridor axes (**15**). These data underpin the interpretation of "avoidance of bulk thermo elastic stressing," yet both sets of measurements are obtained in centimetre scale domains where supracrystalline fabrics and nanoparticle chains can be directly characterized. Whether comparable conduction pathways, and thus similar stress conditions, persist over tens to hundreds of metres in heterogeneous reservoirs remains an open question that current datasets cannot resolve. Risk metrics derived from these laboratory observations compound several layers of interpretation. Stress gradient thresholds of 0.72 and $0.77\ psi\,ft^{-1}$ are used to delineate acceptable and potentially unacceptable operational domains (**24**).

Formation specific tables for granite, basalt, and limestone combine permeability, pressure ranges, fracture stability indices, film strengths, and seismic sensitivity factors into a seismic risk matrix and formation stability index (**23**).

However, these indices rely on core scale measurements of aperture degradation, thermal conductivity, and, in the case of SPARC, AE characteristics, together with modeled pressure distributions. Without dense field microseismic catalogues and distributed temperature and pressure data, it is difficult to quantify how strongly these indices constrain actual induced seismicity behaviour in reservoirs. Research on SPARC scale up and GEIOS explicitly notes that high pressure, high temperature chambers, even when equipped with advanced AE arrays and multiphysics sensing, cannot reproduce reservoir scale fault slip or the complexity of natural fault networks.

This limitation directly affects interpretation of apparent reductions in microseismic energy release, fracture degradation rates, and conduction dominated thermal behaviour as indicators of reduced seismic risk. Field scale microseismic monitoring, integrated with distributed temperature sensing, pressure logging, and gas composition analysis, is therefore indispensable for testing whether the laboratory derived probability density functions, stress gradient thresholds, and formation stability indices remain valid under operational reservoir conditions, and for iteratively updating these quantities as new observations accumulate (**15**,**16**,**23**,**24**).

8.3 Risk Characterization Beyond Lab Data

8.3.1 Environmental and regulatory considerations

Environmental implications of the nanofoam configuration arise first from its working fluid composition and thermal transport mode. The nitrogen matrix constitutes approximately $95\ \%$ of the nanofoam volume, while heat transfer is dominated by conduction through embedded Al_2O_3 and silica nanoparticles that deliver bulk thermal conductivities near $30\ W\,m^{-1}\,K^{-1}$, a 166 to $336\ \%$ increase over conventional geothermal materials with conductivities below $1.0\ W\,m^{-1}\,K^{-1}$ (**23**,**5**,**8**).

This conduction dominated regime avoids the extensive convective cooling of rock volumes required in water based systems and thereby supports the "avoidance of bulk thermo elastic stressing" under the tested 80 to $140\ MPa$ and up to $240\ ^{\circ}C$ conditions (**23**,**5**). Reduced thermo elastic stressing, together with stable fracture apertures that degrade by only $12\ \%$ over 15 weeks, lowers the likelihood of fracture collapse that could compromise long term reservoir integrity and necessitate additional drilling or stimulation, both of which carry environmental footprints (**24**).

System level environmental performance also reflects durability and maintenance frequency. Validation tests show performance retention above $94\ \%$ after $1000\ h$, and analyses project maintenance intervals exceeding 10 years, compared with more frequent interventions in conventional geothermal technologies (**24**,**23**).

Fewer workovers and stimulations imply reduced cumulative material use and surface disturbance over the life of an installation. In addition, SPARC based Engineered Geothermal Hydrogen Systems are projected to deliver hydrogen at 1.5 to $2.5\ \$kg^{-1}$, with life cycle carbon intensities of 0.4 to $0.7\ kg\ CO_2e\,kg^{-1}\ H_2$, significantly below steam methane reforming at 9 to $12\ kg\ CO_2e\,kg^{-1}\ H_2$ and competitive with electrolysis powered by renewable electricity (**16**).

Where nanofoam is co injected in hybrid EGS concepts, conduction pathways with conductivities of about $30.5\ W\,m^{-1}\,K^{-1}$ can raise heat extraction efficiency by 50 to $150\ \%$, further improving the energy returned per unit of environmental input (**16**,**15**). Regulatory evaluation of induced

seismicity risk must take into account that all current nanofoam and SPARC data derive from core scale experiments. High pressure, high temperature chambers and the associated acoustic emission arrays cannot reproduce reservoir scale fault slip or the complexity of natural fault systems (**15**,**16**,**23**,**24**).

For GEIOS, injection pressure is treated probabilistically over 1200 to $2000\ psi$, with quantiles at 1314.0, 1603.7, and $1901.2\ psi$, and stress gradient thresholds of 0.72 and $0.77\ psi\ ft^{-1}$ delimiting acceptable and potentially unacceptable operational domains (**23**,**24**).

These quantities provide a structured basis for regulatory envelopes, but they remain calibrated predominantly on laboratory behaviour and limited field constraints. SPARC scale up analyses specify monitoring architectures that are directly relevant for regulatory oversight. Field implementation would require distributed temperature sensing to track thermal fronts, pressure transducers to monitor permeability evolution, gas composition analysis to detect anomalies, and microseismic monitoring to ensure fracture containment. For moderately sized SPARC systems comprising 5 to 10 wells, capital expenditure is dominated by drilling ($\sim 60\ \%$ of total), with operating expenses largely associated with fluid handling and gas separation; hydrogen production costs of 1.5 to $2.0\ \$kg^{-1}$ are projected, competitive with other low carbon pathways (**15**,**16**).

These techno economic findings imply that incorporating comprehensive monitoring into permitting conditions is feasible without rendering projects uneconomic. Research shows that uncertainty assessment for the nanofoam system already integrates real time seismic mapping, reservoir logs, and laboratory validation into parameter probability density functions for injection pressure, pore pressure, and stress, with broader uncertainty ranges applied where data are sparse (**23**,**24**).

From a regulatory perspective, such conservative treatment of poorly constrained parameters, together with explicit stress gradient thresholds and formation specific seismic sensitivity factors for granite, basalt, and limestone, forms an initial basis for risk based licensing. However, both GEIOS and SPARC studies emphasise that validation of reduced induced seismicity and environmental benefit at reservoir scale requires continuous field microseismic monitoring and iterative updating of these probabilistic models as operational data accumulate (**15**,**16**,**23**,**24**).

9 Conclusion

Laboratory evaluation of the nitrogen hybrid gas nanofoam integrated with engineered conductive corridors demonstrates consistent performance across thermal, mechanical, and flow metrics under controlled high-pressure and high-temperature conditions. An engineered fracture aperture of $3\ mm$ exhibited approximately 12% total degradation over 15 weeks of cycling at 80–$140\ MPa$ and up to $240\ ^{\circ}C$, while bulk thermal conductivity remained near $30\ W\ m^{-1}\ K^{-1}$. Flow regimes reached Reynolds numbers above 10^4 and Weber numbers above 50, particle distributions showed coefficients of variation below 5%, coalescence rates were below 0.5% per hour, and the working fluid composition approached 95% nitrogen by volume with low single-digit (0.6–0.8 vol% Al_2O_3; 0.3–0.5 vol% SiO_2) nanoparticle volume fractions (**24**,**23**).

Mechanistic interpretation links these outcomes to three interacting factors: a nitrogen-dominated carrier that promotes more uniform pressure distribution and avoids a granular skeleton; engineered nanoparticle networks and supracrystalline corridors that create preferential phonon transport for conduction-dominated heat extraction; and removal of discrete proppant packs that would otherwise generate fines (6% ceramic, up to 51% sand), porosity reductions of 75–98%,

and conductivity losses approaching 99%. Core-scale acoustic emission monitoring recorded a shift toward lower-energy, higher-frequency micro-failures: a 49% reduction in total events (52 vs. 102), a 59% reduction in average event energy (2.34 vs. $5.73\ aJ$), and an 83% increase in characteristic frequency (6.55 vs. $3.57\ kHz$), with b-value reaching 1.52—consistent with distributed microcracking rather than abrupt macro ic rupture (**15**,**16**).

Risk characterization treats injection pressure as a probabilistic variable and incorporates explicit stress-gradient criteria. Injection pressure was represented across 1200–$2000\ psi$ (quantiles P5 = 1314.0, P50 = 1603.7, P95 = $1901.2\ psi$); sensitivity analyses identify stress-gradient thresholds separating acceptable operation ($< 0.72\ psi\ ft^{-1}$) from regimes requiring enhanced caution ($> 0.77\ psi\ ft^{-1}$). Pressure decay to 50% of initial overpressure occurred in $3.2\ \mathrm{min}$, and material recovery exceeded 98% with a biodegradation index of 0.94 and ecological impact factor below 0.1 (**23**,**24**).

All experimental and acoustic emission results derive from core-scale tests in high-pressure, high-temperature chambers and from numerical modelling; such settings do not reproduce kilometre-scale fault geometry, long-range pore-pressure diffusion, or the structural complexity of natural fault networks. To validate whether the laboratory-indicated reductions in microseismic energy and improved fracture stability translate into a lower induced-seismicity risk at field scale, staged reservoir trials are recommended. These trials should embed continuous microseismic networks, distributed temperature sensing, high-resolution downhole pressure gauges, gas composition analysis, and flow and particle distribution diagnostics, together with adaptive control systems that enforce the probabilistic pressure and stress-gradient limits established here (**15**,**16**,**23**,**24**).

10 Nomenclature

Symbol definitions in this work are grounded in quantities directly measured or explicitly defined in the nanofoam and SPARC validation programmes. Injection pressure P_{inj} denotes the applied fluid pressure at the wellhead or chamber inlet. For GEIOS nanofoam tests and uncertainty analysis, P_{inj} is treated as a probabilistic variable spanning 1200 to $2000\ psi$, with $5\ \%$, $50\ \%$, and $95\ \%$ quantiles at 1314.0, 1603.7, and $1901.2\ psi$, corresponding to 80 to $140\ MPa$ in the high pressure chamber (**23**,**24**).

The stress gradient G_σ is expressed in $psi\ ft^{-1}$ and used as a primary risk indicator; values below $0.72\ psi\ ft^{-1}$ define acceptable operating domains, whereas gradients above $0.77\ psi\ ft^{-1}$ are associated with potentially unacceptable risk (**24**).

Fracture aperture a refers to the mechanical opening of the principal engineered fracture, typically initialized at $3\ mm$ in GEIOS validation. Degradation of aperture is quantified through a linear law

$$D(n) = D_0 + kn,$$

where $D(n)$ is the cumulative percentage degradation after n cycles, D_0 is the initial degradation offset, and k is the degradation coefficient, measured at less than $0.006\ \%$ per cycle, giving approximately $12\ \%$ total degradation over 15 weeks and performance retention above $94\ \%$ after $1000\ h$ (**24**,**23**).

Formation damage is summarized by the formation damage factor F_D, with reported values below 0.15 for nanofoam injection, alongside permeability preservation exceeding $92\ \%$ and porosity retention above $95\ \%$ (**24**).

Thermal transport is characterized by the thermal conductivity κ in $W\,m^{-1}\,K^{-1}$. For GEIOS nanofoam, bulk conductivity $\kappa_{NF} \approx 30\ W\,m^{-1}\,K^{-1}$ is measured by a modified transient hot wire method under 80 to $140\ MPa$ and up to $240\ ^{\circ}C$, representing a 166 to $336\ \%$ enhancement relative to conventional fluids with $\kappa < 1.0\ W\,m^{-1}\,K^{-1}$ (**23**,**24**,**5**).

In SPARC corridors, directional conductivity $\kappa(\theta)$ exhibits an ellipsoidal distribution, with $\kappa(0^{\circ}) \approx 30\ W\,m^{-1}\,K^{-1}$ along the corridor axis and lower values at orthogonal directions, as resolved by polar measurements and supported by Brillouin spectroscopy, which links κ to phonon mean free path ℓ via $\ell = 3\kappa/(C_v v)$ (**15**).

Acoustic emission quantities follow standard definitions. The total number of detected events N_{AE} counts discrete microseismic transients over a test, with SPARC treated cores showing $N_{AE} = 52.0$ versus 102.0 in controls. Average event energy E_{AE} (attojoule scale) is computed from waveform integrals, with mean values of $2.34\ aJ$ and $5.73\ aJ$ for treated and control samples, respectively. Additional descriptors include average amplitude A_{AE} in dB, event duration T_{AE} in μs, counts C_{AE} (threshold crossings), and characteristic frequency f_{AE} in kHz; SPARC treatment shifts f_{AE} from 3.57 to $6.55\ kHz$ (**15**,**16**).

These quantities underpin frequency magnitude and energy release analyses used in subsequent risk interpretation. Statistical descriptors of operating conditions use standard percentile notation. The $5\ \%$ quantile $Q_{0.05}(P)$, $50\ \%$ quantile $Q_{0.50}(P)$, and $95\ \%$ quantile $Q_{0.95}(P)$ for injection pressure are defined such that $\Pr\big(P \le Q_{0.05}(P)\big) = 0.05$, $\Pr\big(P \le Q_{0.50}(P)\big) = 0.50$, and $\Pr\big(P \le Q_{0.95}(P)\big) = 0.95$, and take numerical values 1314.0, 1603.7, and $1901.2\ psi$, respectively, in the present uncertainty space. Probability density functions $PDF(x)$ are constructed for parameters such as P_{inj}, particle spacing, and pore pressure to reflect variability and data quality across laboratory and field constraints (**23**,**24**).

Finally, hydrogen production metrics in SPARC related Engineered Geothermal Hydrogen Systems employ production rate R_{H_2} in $tonnes\,yr^{-1}$ and specific energy $E_{H_2} \approx 33\ kWh\,kg^{-1}$. Economic analysis defines the levelized cost C_{H_2} in $\$\,kg^{-1}$, with modeled ranges of 1.5 to $2.5\ \$\,kg^{-1}$ for EGHS and 1.5 to $2.0\ \$\,kg^{-1}$ for SPARC systems producing 500 to $1000\ tonnes\,yr^{-1}$ (**16**,**15**).

These symbols and numerical ranges are used consistently in scaling and techno economic discussion elsewhere in this work.

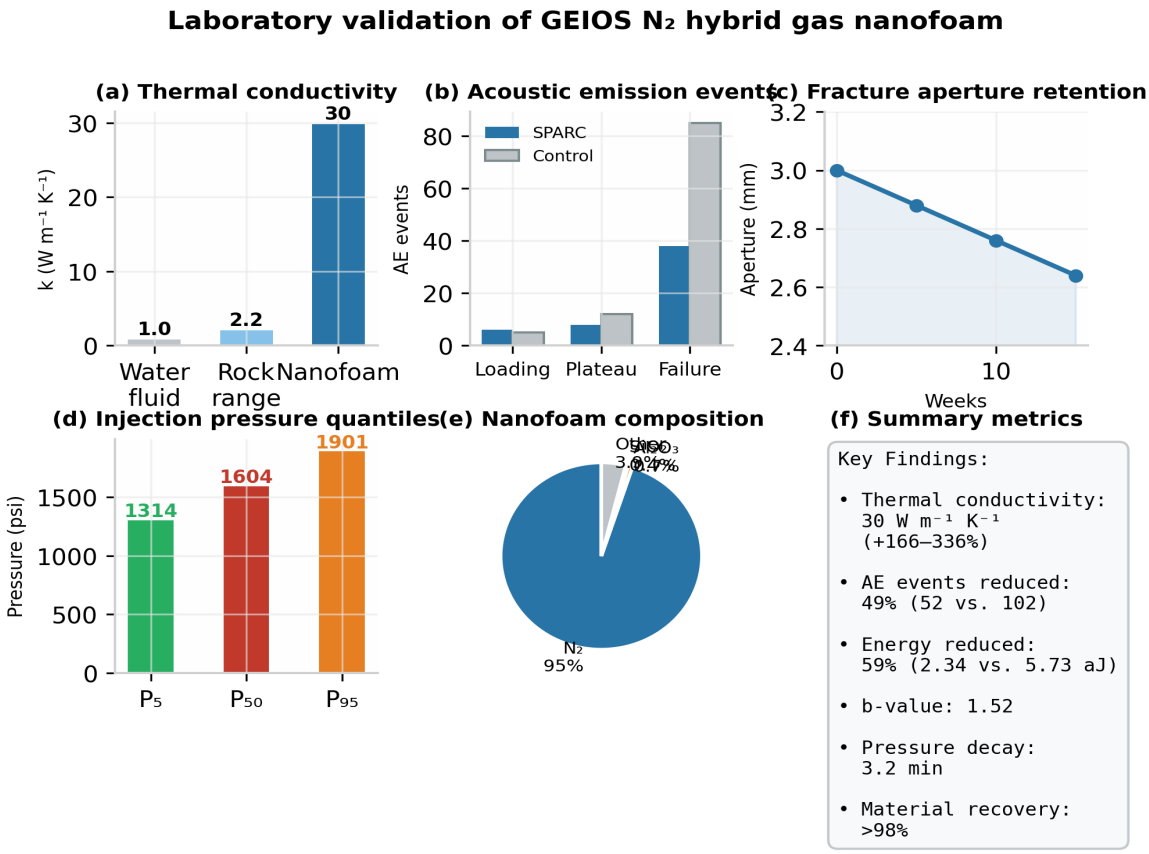

Figure 1. *Comprehensive summary of GEIOS nitrogen hybrid gas nanofoam laboratory validation, showing (a) thermal conductivity comparison across water-based fluid, rock baselines, and nanofoam; (b) phase-resolved acoustic emission events for SPARC-treated versus water-fractured control cores; (c) time-dependent fracture aperture retention over 15 weeks; (d) probabilistic injection pressure quantiles (P_5, P_{50}, P_{95}); (e) nanofoam volumetric composition; and (f) key summary metrics.*

11 References

[1] Ellsworth, W. L. (2013). Injection-Induced Earthquakes. Science, 341(6142), 1225942.

[2] Ellsworth, W. L. et al. (2019). Triggering of the Pohang, Korea, Earthquake (Mw 5.5) by Enhanced Geothermal System Stimulation. Seismological Research Letters, 90(5), 1844–1858.

[3] Zhou, W. et al. (2024). Managing Induced Seismicity Risks From Enhanced Geothermal Systems. Reviews of Geophysics, 62, e2024RG000849.

[4] Understanding injection-induced seismicity in enhanced geothermal systems (2020). Earth-Science Reviews, 205, 103182.

[5] Experimental Investigation on the Influence of Proppant Crushing (2025). Processes (MDPI), 13(7), 2166.

[6] An experimental investigation of the effect of long-term, time-dependent proppant embedment (2021). International Journal of Rock Mechanics and Mining Sciences.

[7] Gas permeability and fracture compressibility for proppant-supported shale fractures (2021). Journal of Natural Gas Science and Engineering.

[8] Stability study of aqueous foams under high-temperature and high-pressure conditions relevant to EGS (2023). Geothermics, 116, 102862.

[9] Lv, Q. et al. (2015). Study of Nanoparticle–Surfactant-Stabilized Foam as a Fracturing Fluid. Industrial & Engineering Chemistry Research, 54(39).

[10] High thermal stability of foams stabilized by graphene oxide (2023). Fuel.

[11] Prospects and Challenges of Waterless/Low-Water Fracturing Technologies (2026). Processes (MDPI), 14(6), 920.

[12] Impact of Nitrogen Foamed Stimulation Fluids Stabilized by Nanoadditives. Energies (MDPI).

[13] Al_2O_3-based nanofluids: a review (2011). Nanoscale Research Letters.

[14] Experimental investigation of thermophysical properties of Al_2O_3–water nanofluid (2017). Journal of Molecular Liquids.

[15] Evolution of b-Value and Fractal Dimension of Acoustic Emission Events During Shear Rupture of an Immature Fault in Granite.

[16] Study on the Acoustic Emission Characteristics of Different Rock Types (2021). Frontiers in Physics, 9, 591651.

[17] Acoustic emission characteristics and failure precursors (2026). Scientific Reports, 15.

[18] Thermal diffusivity and conductivity of supracrystalline ceramics under nitrogen atmosphere by laser flash analysis.

[19] Häring, M. O. et al. (2008). Characterisation of the Basel 1 enhanced geothermal system. Geothermics, 37(5), 469–495.

[20] Grigoli, F. et al. (2018). The November 2017 Mw 5.5 Pohang earthquake: A possible case of induced seismicity in South Korea. Science, 360(6392), 1003–1006.

[21] Klinkenberg, L. J. (1941). The permeability of porous media to liquids and gases. Drilling and Production Practice, API, 200–213.

[22] Brace, W. F., Walsh, J. B., & Frangos, W. T. (1968). Permeability of granite under high pressure. Journal of Geophysical Research, 73(6), 2225–2236.

[23] Serroune, S. A. M., & Kessler, O. M. (2024). GEIOS Nitrogen Hybrid Gas Nanofoam: Validation Programme Report. Nanogeios Laboratory USA LLC, Internal Technical Report.

[24] Serroune, S. A. M., & Kessler, O. M. (2024). Probabilistic Risk Assessment and Uncertainty Quantification for the GEIOS EQG System. Nanogeios Laboratory USA LLC, Internal Technical Report.

[25] Gutenberg, B., & Richter, C. F. (1944). Frequency of earthquakes in California. Bulletin of the Seismological Society of America, 34(4), 185–188.